

Estuary Turbulence and Air-Water CO₂ Exchange

Philip Mark Orton

Submitted in partial fulfillment of the
requirements for the degree
of Doctor of Philosophy
in the Graduate School of Arts and Sciences

COLUMBIA UNIVERSITY

2010

© 2010
Philip Mark Orton
All Rights Reserved

ABSTRACT

Estuary Turbulence and Air-Water CO₂ Exchange

Philip Mark Orton

The mixing of constituents between estuarine bottom and surface waters or between estuarine surface waters and the atmosphere are two topics of growing interest, in part due to the potentially important role of estuaries in global carbon budgets. These two types of mixing are typically driven by turbulence, and a research project was developed to improve the scientific understanding of atmospheric and tidal controls on estuary turbulence and air-water exchange processes. Highlights of method development and field research on the Hudson River estuary include several deployments of bottom mounted current profilers to quantify the turbulent kinetic energy (TKE) budget, and construction and deployment of an instrumented catamaran that makes autonomous measurements of air-water CO₂ exchange (F_{CO_2}), water TKE dissipation at 50 cm depth (ϵ_{50}), and other physical properties just above and below the air-water interface.

On the Hudson, wind correlates strongly with ϵ_{50} , but surface water speed and air-water heat flux also have moderate correlations with ϵ_{50} . In partially mixed estuaries such as the Hudson, as well as salt wedge estuaries, baroclinic pressure forcing typically causes spring ebb tides to have much stronger upper water column shear than flood tides. The Hudson data are used to show that this shear leads to local shear instability and stronger near-surface turbulence on spring ebbs. Also, buoyancy budget terms are compared to demonstrate how water-to-air heat fluxes can influence stratification and indirectly

influence ε_{50} . Looking more closely at the role of wind forcing, it is demonstrated that inland propagation of the sea breeze on warm sunny days leads to arrival in phase with peak solar forcing at seaward stations, but several hours later at up-estuary stations. Passage of the sea breeze front raises the air-water CO₂ flux by 1-2 orders of magnitude, and drives ε_{50} comparable to spring tide levels in the upper meter of the water column. Modeling and observational studies often use remotely-measured winds to compute air-water fluxes (e.g. momentum, CO₂), and this is shown to cause large flux errors during these periods, in terms of magnitude and diurnal phase.

TABLE OF CONTENTS

List of figures and tables	v
Acknowledgments	vii
Dedication	ix
Preface	x
Chapter 1:	
Introduction.....	1
1. Introduction	2
2. The importance of estuary carbon	3
3. The measurement challenge.....	4
4. Dissertation plan.....	5
References.....	6
Chapter 2:	
Variability of internally generated turbulence in an estuary, from 100 days of continuous observations.....	13
Abstract.....	14
1. Introduction	14
2. Field program and data processing	17
2.1 ADCP turbulence sampling and processing.....	18
2.2 ADCP turbulence quality control	20
2.3 Acoustic backscatter observations of turbulent structures and sea-surface height	21
3. Analyses.....	21
3.1 Layer definitions	22
3.2 Cross-correlation analyses	24
4. Results	25
5. Discussion.....	28
5.1 Forcing of Site C IML turbulence	29
5.2 Forcing of Site B IML turbulence	32
5.3 IML and BBL turbulence variability on sub-tidal to seasonal timescales	33

5.4 Implications for estuarine circulation, modeling and transports	37
6. Summary and conclusions	40
References	41
Figure captions.....	46

Chapter 3:

An autonomous self-orienting catamaran (SOCa) for measuring air-water exchanges and forcing	62
Abstract.....	63
1. Introduction	63
2. Materials and procedures	65
2.1 SOCa construction and data logging.....	66
2.2 Sensors and locations.....	67
2.3 The inertial dissipation method (IDM)	69
2.4 ADV data processing.....	70
2.5 Autonomous application of the Gradient Flux Technique (GFT)	72
2.6 CO ₂ data processing.....	75
2.7 The flux footprint.....	76
3. Assessment	77
3.1 Field evaluation.....	77
3.2 Platform orientation	78
3.3 Velocity and turbulence validation.....	79
3.4 CO ₂ validation and uncertainty tests	80
3.5 GFT applicability, profile height and footprint.....	84
4. Discussion.....	86
References.....	90
Figure captions	95

Chapter 4:

Tidal and atmospheric influences on near-surface turbulence in an estuary	112
Abstract.....	113
1. Introduction	114
2. Background	117
2.1 The turbulent kinetic energy budget.....	118
3. Methods	119

3.1	Field experiments.....	119
3.2	Acoustic data proecssing	122
3.3	Dissipation estimates from ADV data.....	123
3.4	TKE budget from ADCP data: P, B, T_D , $\partial TKE/\partial t$	125
3.5	ADCP turbulence data quality control	128
3.6	Surface heat flux estimates	129
3.7	Additional derived quantities.....	131
4.	Results	132
4.1	Near-surface dissipation observations and regressions	134
4.2	Near-surface TKE budgets	136
5.	Discussion.....	138
5.1	Wind stress generation of turbulence	138
5.2	Ebb dominance of near-surface dissipation	140
5.3	The role of bed stress versus local shear instability.....	141
5.4	Buoyancy flux impacts on water column stratification	143
5.5	Heat flux impacts on near-surface turbulence generation	144
6.	Summary and conclusions	147
	References.....	149
	Figure captions	154

Chapter 5:

Sea breeze forcing of estuary turbulence and air-water CO ₂ exchange.....	170
Abstract.....	171
1. Introduction	171
2. Field observations	172
3. Results and discussion.....	174
3.1 Sea breeze driven turbulence and air-water CO ₂ exchange.....	176
3.2 Errors from under-sampling or using remote winds.....	177
3.3 Broader context	178
References	180
Figure captions.....	182

Chapter 6:

Conclusions and future research	188
1. Summary.....	189

2. Primary conclusions	189
3. Implications for modeling estuarine gas transfer for any estuary	191
References	192

Appendix A:

Integrated ocean-atmosphere sampling aboard a robotic boat.....	193
Abstract.....	194
1. Introduction	194
2. Measurements.....	196
2.1 The ocean-atmosphere sensor integration system (OASIS).....	196
2.2 Instrumentation and methods	197
2.3 Coastal ocean deployments	199
3. Results and discussion.....	200
3.1 Autonomous, integrated atmosphere-ocean sampling in Massachusetts Bay	200
3.2 Future possibilities with robotic boats.....	201
References	203
Figure captions	205

LIST OF FIGURES AND TABLES

Chapter 1

Figure 1: Conceptual turbulence and air-water exchange diagram	10
Figure 2: Photo showing a water surface boil and white foam	11
Figure 3: Five minute time series showing a large instability	12

Chapter 2

Figure 1: Conceptual mixing layer diagram	50
Figure 2: Hudson River estuary coastline (left) with bathymetry	51
Figure 3: Time series view of ambient conditions and turbulence during ADCP deployments	52
Figure 4: Relationship between bed frictional forcing and turbulence	53
Figure 5: Three along-channel density transects during spring freshet season	54
Figure 6: Summary of stratification observations, versus along-channel location	55
Figure 7: Zoom-ins of a neap-spring transition with high riverflow	56
Figure 8: Zoom-ins to 0.5 Hz raw data for 20-minute periods	58
Figure 9: 20-minute averages of data from the periods shown in the prior figure	59
Figure 10: Comparison of stratification with the percentage of turbulence in the IML ...	60
Figure 11: Post-neap tides have higher IML turbulence than post-spring transitional tides, a hysteresis pattern	61

Chapter 3

Table 1: Sensors, locations, and sample rates on SOCa	99
Figure 1: Plan view of SOCa with the autonomous CO ₂ profiling system	100
Figure 2: Photo of SOCa during the CASsIE study	101
Figure 3: Example inertial dissipation method fits for estimating TKE dissipation	102
Figure 4: CASsIE field experiment observations and flux estimates made from SOCa	103
Figure 5: SOCa rotational performance under differing wind and water velocities	104
Figure 6: SOCa orientation relative to the water current, as a function of wind speed ...	105
Figure 7: SOCa pitch angle standard deviations plotted as a function of wind speed	106
Figure 8: Comparison of catamaran-mounted ADV and bottom-mounted ADCP measurements of water speed	107
Figure 9: Bin-averaged dissipation for different wind and water speeds	108
Figure 10: Three typical cases showing the equilibration rate of the equilibrators	109

Figure 11: Observed wind speed versus gas transfer velocity	110
Figure 12: Guidance for planning the CO ₂ profile height with GFT	111
Chapter 4	
Table 1: Results of the correlation analyses for near-surface dissipation.....	158
Figure 1: Conceptual diagram showing processes that may influence upper water column turbulence in an estuary	159
Figure 2: Hudson River estuary coastline with study site and bathymetry	160
Figure 3: Time series of ambient conditions during the 2007 CASsIE study	161
Figure 4: Water and wind conditions during one 12-hour timeseries	162
Figure 5: Tidal phase bin-averaged water velocity and dissipation	163
Figure 6: The relationship between wind speed and dissipation	164
Figure 7: The relationship between net air-water heat flux and dissipation.....	165
Figure 8: Velocity profiles for periods used in the strong spring tide TKE budgets	166
Figure 9: Vertical turbulence lengthscales for the periods used in the budgets.....	167
Figure 10: Mean TKE budget terms for strong spring tides	168
Figure 11: Comparison of the estimated buoyancy fluxes that govern water column stratification	169
Chapter 5	
Figure 1: Study area map, with wind and air temperature data on a sea breeze day.....	184
Figure 2: Observations during the day shown in Figure 1 plus three more days.....	185
Figure 3: Comparing turbulence levels resulting from sea breezes and spring tides.....	186
Figure 4: Variance-preserving wind velocity spectra	187
Chapter 6	
Appendix A	
Figure 1: The Ocean-Atmosphere Sensor Integration System, a robotic boat	206
Figure 2: The shoreward transect off the coast of Virginia, with salinity shaded	207
Figure 3: Transect T1 from the Massachusetts Bay study, with air-sea CO ₂ flux	208
Figure 4: Atmosphere and ocean profile time series data from the Massachusetts Bay study	209

ACKNOWLEDGMENTS

First and foremost, thank you to my inspirational parents, Barbara and Colin, for setting an amazing example and giving me all the support one could ever ask for; and to Jennifer for inspiring me, having endless patience for my long hours, and for giving me something to smile about each and every day.

I want to express my gratitude to my dissertation advisers, Wade McGillis and Christopher Zappa, for leading me in exciting, original, and rewarding directions academically; Doug Martinson for being a good friend, brilliant scientist, and spectacular storyteller; Martin Visbeck for opening the door to Columbia and being a great mentor; Adam Sobel and Alan Blumberg for taking time out to join as committee members; Arnold Gordon, Bob Houghton, and Andreas Thurnherr for providing assistance and inspiration; David Jay and Antonio Baptista for encouraging me to get my hunting license; John Moisan, John Higinbotham, and Carl Schirtzinger for being a pleasure with which to work; John Lipscomb, eyes-on-the-water and captain for the Hudson Riverkeeper, for always being willing to share his deep Hudson knowledge, memorable storytelling and conducting the along-channel CTD surveys and ADCP deployments; Bruce Huber for being an extremely knowledgeable and experienced friendly face around the corner; Tim Newberger for being a great guy and an all-knowing god of ocean carbon dioxide measurement technology; Frank Nitsche for field and mapping assistance; Bernie Gallagher for assistance with platform development; Rocky Geyer and Parker MacCready for giving me the opportunity and inspiring me at the Friday Harbor summer school; Friendly conversationalists and helpful field assistants Kandaga Pujiana, Brice Loose, Jonathan

Bent, Nadine Els, Jay De Lanoy, Matt Linkswiler; Malcolm Scully for useful suggestions for the dissipation computations; Mia Leo, Missy Pinckert, Carol Mountain for support and happiness whenever in the Geoscience Building, from my first visit for interviews onward; and Mauricio Gonzalez of Frederick Douglas Academy in Harlem for collaborations, field assistance, and most of all, for the Maou Funk soundtrack that smoothed my dissertation-writing ups and downs.

This research was funded by the National Science Foundation, Environmental Protection Agency, Department of Earth and Environmental Sciences, Hudson River Foundation, and National Aeronautics and Space Administration.

DEDICATION

In memory of Patricia Cornell
whose wisdom and kindness
splash gently on the Jersey Shore

PREFACE

Most people are surprised an oceanographer would bother living in New York City.

Before I moved here, I was aware that the Hudson River typically runs brackish for at least its lower 20 miles, but I too failed to comprehend how amazing of a place this would turn out to be for an ocean scientist. Estuaries and tidal straits of every stripe run through or near New York City, from the Hudson to East River, Harlem River, Jamaica Bay, Long Island Sound, and dozens more out on Long Island. You can find mild currents or extreme currents, and heavily polluted waters or clean swimmable waters brimming with fish.

There are so many blue crabs here, that at least one supplier from the Chesapeake regularly looks to our region's fishermen as a source. There is no shortage of ocean fish migrating through for ordinary city dwellers to snare along the banks of these waterways. Unfortunately, these people are taking chances due to pollution, particularly after rainfall "flushes" pollution into the system, so to speak.

Today I surveyed the view from the top of my apartment building on the east side of Manhattan. Down below are the turbulent currents of Hell Gate, where strong currents from East River, Harlem River and western Long Island Sound all swirl together and hundreds of ships sank through history. I can track the latter two waterways off toward the horizon, and looking across the island I can even see the cabled towers of George Washington Bridge, reminding me that the Hudson is just a few miles away.

A balance has finally been struck here between the needs of millions of people and these natural brackish waterways. In the past, the water suffered extreme degradation, but

these days there is a revival due to reductions in pollution inputs. Moreover, the capacity of these waterways to absorb pollution is amazing. It all comes down to the strong dispersive currents that surround the city, which oceanographers measure with instrumentation we deploy on the seabed. If you've ever seen East River churning like water at a rolling boil, you'll know what I'm talking about.

As an oceanographer, I seek to optimize this balance, studying the currents and water quality and improving our predictive capacity.

As an educator, I get excited about the aquatic educational possibilities for the dozens of schools that are built right alongside the water. Most the schools have the water at their backs, with no windows and no waterfront access because when they were built, the water was an eyesore.

Once upon a time, hundreds of years ago, this was an amazing natural fishery with abundant fish, oyster beds, birds, and who knows what more. The most exciting prospect is that our improved environmental regulations and gradual movement away from heavy industry makes at least a partial return to this natural state possible.

Remarkably, a famous developer recently published an editorial in the Sunday edition of the Times recommending that the Harlem River tidal strait be filled with dirt, to provide additional real estate and park land for the city. He argued that neighborhoods need to expand, and schools need football fields, and a very small percent of the people see value in the waterway.

As sure as these tides will always push and pull, I know there will always be room for an oceanographer in this vibrant ocean island city.

Chapter 1

INTRODUCTION AND MOTIVATION

1. Introduction

Air-water exchanges and internal ocean mixing of heat, salt, carbon dioxide and momentum are being studied and modeled at an increasing level of detail because of their important influence on ocean circulation and climate. The operation of these processes in rivers, estuaries and the continental shelf is also of growing interest due to the potentially important role of these regions in the global carbon budgets [*Birdsey et al.*, 2009; *Borges*, 2005], and growing concerns over hypoxia [e.g., *Dai et al.*, 2006]. A fundamental problem with computer modeling, however, is the incomplete representation of the nonlinear physics of these small-scale mixing processes. Numerical models represent them with parameterizations because of computer processing constraints. Yet, unless these parameterizations are developed with a strong physical basis and validated with observational datasets with a wide range of forcing, they typically do not work for multiple ocean regions [e.g., *McGillis et al.*, 2004].

Recent work has demonstrated synergy in studying both air-water exchanges and near-surface water turbulence together, demonstrating fundamental links and feedbacks between these processes. Air-water gas exchange is fundamentally an interfacial turbulent process in all but the most quiescent conditions, whether forced by tidal currents, wind, rain [*Zappa et al.*, 2007] or diurnally-forced convection and shear instability in the surface ocean [*McGillis et al.*, 2004].

Estuaries are useful locations to study these turbulent mixing processes due to their convenient access, and diverse characteristics (e.g. wind fetch, water depth, stratification). A broad variety of turbulent features may be present, including tide-driven and wind-driven shear instability, forced convection at density fronts [*Orton and Jay*, 2005], surface boils,

internal wave breaking, and wind wave breaking (**Figures 1-3**). Furthermore, estuarine upper water column turbulence is a topic of interest in its own right, because it is not well-understood and has not been studied as widely as its well-known neighbor bottom boundary layer turbulence. One of the primary remaining shortcomings of three-dimensional numerical estuary models is that the upper water column salinity structure is poorly predicted [e.g., *Li et al.*, 2005; *Warner et al.*, 2005]. Moreover, due to the role of salt determining density, an inaccurate modeled vertical salinity structure leads to reduced skill in predicting the estuarine circulation and longitudinal salinity gradient [*Warner et al.*, 2005].

2. The importance of estuary carbon

Estuaries are metabolically active regions – they are among the world’s most productive ecosystems, yet typically have even stronger respiration of organic matter [*Borges et al.*, 2005]. Estuaries receive organic matter from throughout the river watershed, and as a result, respiration is often higher than local production and estuaries become supersaturated in CO₂. Much of this is outgassed to the atmosphere through air-water exchange, but a significant proportion is also delivered to the open ocean [*Cole et al.*, 2007]. These relatively large air-water CO₂ fluxes are relatively easy to measure relative to those in the open ocean, making them particularly useful regions to study the physical forcing of these exchanges. Globally, estuaries and salt marshes are estimated to be a source of 0.34 PgC y⁻¹ [*Borges et al.*, 2005]. This is large compared with the total ocean carbon sink, but this carbon is typically part of a cyclic process, with terrestrial or aquatic photosynthesis initially drawing the CO₂ from the atmosphere. The greater questions are

(a) what the role of estuaries is in transforming terrestrial carbon and controlling the proportion that reaches the deep sea, and (b) whether anthropogenic disturbance to estuaries is causing any change in this flux [Abril *et al.*, 2002].

3. The measurement challenge

Accurately measuring small-scale turbulent mixing processes within a water body or across an interface between different fluids presents a serious observational challenge. Our ability to observe and understand near-surface turbulence in natural water bodies has been limited by several factors, including: (1) the fact that it is often highly heterogeneous in space and time, (2) it can be too subtle to be measured by conventional instruments, (3) it is in a moving reference frame with tides and waves displacing the sea surface, and (4) the turbulent velocity fluctuations of interest are much smaller than surface wave orbitals. Observations of turbulent mixing far from the bottom boundary have until recently required costly and labor-intensive instrumentation [e.g., Peters and Bokhorst, 2000]. Turbulence near the sea surface is also complicated by processes occurring at the air-water interface that are difficult to measure, such as wave breaking and heat fluxes.

Direct measurement of exchanges across the air-water interface suffers from some of the same difficulties. Most prior gas exchange studies have utilized tracers, floating chambers, or direct eddy covariance measurements, but all these approaches have important drawbacks. Floating chambers have been criticized for disturbing sampling area too much to achieve accurate measurements, and laboratory studies have sometimes cast doubt on their accuracy [Belanger and Korzun, 1991]. Tracer methods are useful for studying large spatial scales and temporal scales of days or longer [Clark *et al.*, 1995], but

shorter timescales and more localized studies would be useful in strongly tidal and spatially variable regions. Eddy covariance flux measurements have the benefits of being a direct measurement of the flux with no sea surface disturbance, and having a relatively small measurement footprint [McGillis *et al.*, 2001]. However, when collected from a moving vessel, challenging motion corrections are required.

Though also challenging, it is advantageous to have autonomous measurements, because it broadens the temporal range of conditions studied (e.g. strong winds or internal waves) and allows for studies of longer timescales (neap-spring, seasonal), relative to manual sampling. Moreover, ambitious efforts are underway to reduce the reliance of oceanographers on inefficient ship-based measurements, and toward observation with autonomous systems. These efforts are gaining momentum, in part, because one of three central oceanographic research priorities for the United States in the next decade is to develop an ocean observation system [NSTC, 2007]. Developing autonomous instrumentation for sampling air-water exchanges or upper ocean turbulence is an important research endeavor in its own right, potentially paving the road to global ocean sampling on autonomous floats, gliders and buoys [Johnson *et al.*, 2009].

4. Dissertation plan

A dissertation research project is described herein, with the following primary goals:

- Develop autonomous methods and platforms to measure near-surface turbulence and air-water exchanges
- Conduct an estuarine sampling program over a wide range of tidal and atmospheric forcing

- Relate these observations broadly to the general circulation and dynamics of estuaries, as well as atmospheric processes
- Evaluate the utility of simple dynamical and regression models for simulating these processes

The dissertation continues in Chapter 2 with a study contrasting two types of turbulence observed in the Hudson River estuary: bottom boundary layer and internal mixing layer turbulence. Chapter 3 is a methodological study where a self-orienting catamaran with similar measurements but also an automatic system for measuring air-water fluxes of carbon dioxide is described and evaluated with a deployment in the Hudson. The measurement approach used on the catamaran has been extended to robotic boats capable of performing autonomous mobile sampling, summarized in Appendix A. Chapter 4 is a detailed study of tidal and atmospheric controls on near-surface turbulence in the Hudson, including complete budgeting of turbulent kinetic energy in the upper water column. In Chapter 5, measurements at an anchored catamaran and four meteorological stations along the Hudson are used to illustrate some basic characteristics and impacts of the sea breeze on turbulence and air-water exchange processes. The final concluding Chapter 6 summarizes what has been learned but also what lies ahead in this ongoing research.

References

Abril, G., M. Nogueira, H. Etcheber, G. Cabecadas, E. Lemaire, and M. Brogueira (2002), Behaviour of organic carbon in nine contrasting European estuaries, *Estuarine, Coastal and Shelf Science*, 54(2), 241-262.

Belanger, T. V., and E. A. Korzun (1991), Critique of floating dome technique for estimating reaeration rates, *J. Environ. Eng.*, *117*, 144-150.

Borges, A. V., B. Delille, and M. Frankignoulle (2005), Budgeting sinks and sources of CO₂ in the coastal ocean: Diversity of ecosystems counts, *Geophys. Res. Lett.*, *32*.

Clark, J. F., P. Schlosser, H. J. Simpson, M. Stute, R. Wanninkhof, and D. T. Ho (1995), Relationship between gas transfer velocities and wind speeds in the tidal Hudson River determined by the dual tracer technique, in *Air-Water Gas Transfer*, edited by B. Jähne and E. C. Monahan, pp. 785-800, AEON Verlag & Studio, Hanau.

Cole, J., et al. (2007), Plumbing the global carbon cycle: integrating inland waters into the terrestrial carbon budget, *Ecosystems*, *10*(1), 172-185.

Dai, M., X. Guo, W. Zhai, L. Yuan, B. Wang, L. Wang, P. Cai, T. Tang, and W.-J. Cai (2006), Oxygen depletion in the upper reach of the Pearl River estuary during a winter drought, *Mar. Chem.*, *102*(1-2), 159-169.

Johnson, K., et al. (2009), Observing biogeochemical cycles at global scales with profiling floats and gliders: Prospects for a global array, *Oceanography*, *22*(3), 216-225.

Li, M., L. Zhong, and W. C. Boicourt (2005), Simulations of Chesapeake Bay estuary: Sensitivity to turbulence mixing parameterizations and comparison with observations, *J. Geophys. Res.*, *110*.

McGillis, W., J. B. Edson, J. E. Hare, and C. W. Fairall (2001), Direct covariance air-sea CO₂ fluxes, *J. Geophys. Res.*, *106*, 16,729-716,745.

McGillis, W. R., et al. (2004), Air-sea CO₂ exchange in the equatorial Pacific, *J. Geophys. Res.*, *109*, C08S02.

Nimmo-Smith, W. A. M., S. A. Thorpe, and A. Graham (1999), Surface effects of bottom-generated turbulence in a shallow tidal sea, *Nature*, *400*, 251-254.

NSTC (2007), Charting the Course for Ocean Science in the United States for the Next Decade: An Ocean Research Priorities Plan and Implementation Strategy, National Science and Technology Council.

- Orton, P. M., and D. A. Jay (2005), Observations at the tidal plume front of a high-volume river outflow, *Geophys. Res. Lett.*, 32, L11605.
- Peters, H., and R. Bokhorst (2000), Microstructure observations of turbulent mixing in a partially mixed estuary. Part I: Dissipation rate, *J. Phys. Oceanogr.*, 30, 1232-1244.
- Warner, J. C., W. R. Geyer, and J. A. Lerczak (2005), Numerical modeling of an estuary: A comprehensive skill assessment, *J. Geophys. Res.*, 110.
- Zappa, C., W. McGillis, P. Raymond, J. Edson, E. Hintsa, H. Zemmeling, J. Dacey, and D. Ho (2007), Environmental turbulent mixing controls on air-water gas exchange in marine and aquatic systems, *Geophys. Res. Lett.*, 34(10), 10601.
- Zappa, C. J., P. A. Raymond, E. Terray, and W. R. McGillis (2003), Variation in surface turbulence and the gas transfer velocity over a tidal cycle in a macro-tidal estuary, *Estuaries*, 26(6), 1401-1415.

Figure Captions

Figure 1: Conceptual diagram showing some of the processes that may influence upper water column turbulence and air-water exchanges in an estuary. Vectors at the center show characteristic ebb tide (toward the left) and flood tide (toward the right) velocity profiles. Vertical turbulent transport of eddies (turbulent kinetic energy, TKE) can lead to surface boils (next figure).

Figure 2: Photograph showing a water surface boil and white foam, caused by very strong turbulence. Boils are surface manifestations of TKE turbulent transport, and can enhance air-water exchanges by replenishing surface waters from below, and by causing turbulence and wave breaking on the sea surface [Nimmo-Smith *et al.*, 1999]. The picture was taken from the Tri-Borough Bridge, New York City, looking down at Hell Gate, the tidal strait connecting East River and Long Island Sound.

Figure 3: Five-minute timeseries showing a large instability at a 15 m deep site in the Hudson River estuary, measured with an acoustic Doppler current profiler. There is typically a two-layer flow at this location, with saline (dense) deep water and relatively fresh surface water. Turbulence driven by tidal currents in an unstratified estuary can produce near-surface turbulence and drive air-water exchanges of CO₂ [Zappa *et al.*, 2003], but little is known about these processes in stratified estuaries.

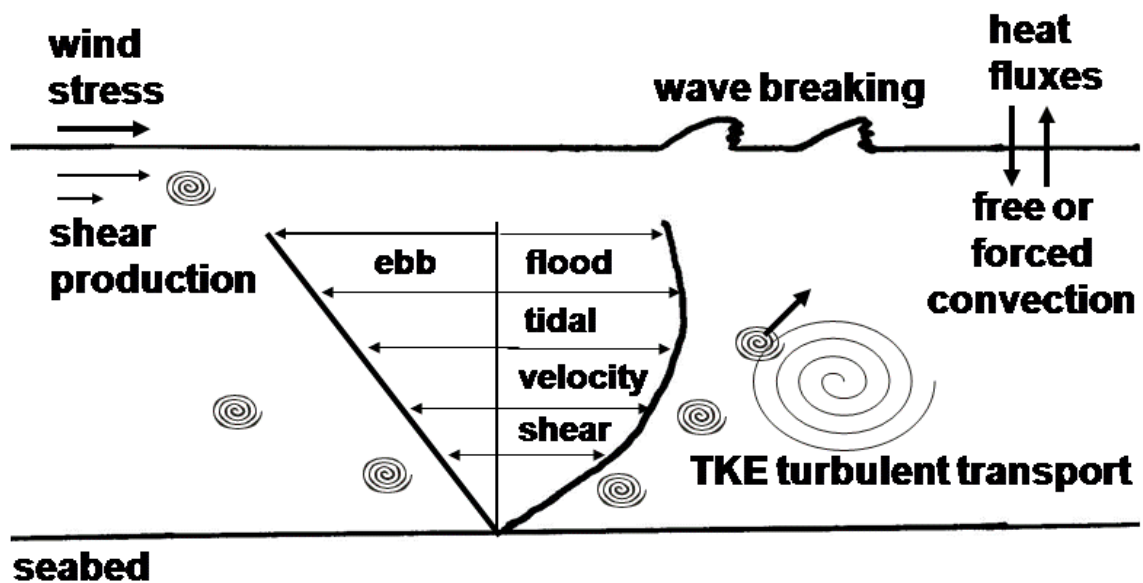


Figure 1: Conceptual diagram showing some of the processes that may influence upper water column turbulence and air-water exchanges in an estuary. Vectors at the center show characteristic ebb tide (toward the left) and flood tide (toward the right) velocity profiles. Vertical turbulent transport of eddies (turbulent kinetic energy, TKE) can lead to surface boils (next figure).



Figure 2: Photograph showing a water surface boil and white foam, caused by very strong turbulence. Boils are surface manifestations of TKE turbulent transport, and can enhance air-water exchanges by replenishing surface waters from below, and by causing turbulence and wave breaking on the sea surface [Nimmo-Smith *et al.*, 1999]. The picture was taken from the Tri-Borough Bridge, New York City, looking down at Hell Gate, the tidal strait connecting East River and Long Island Sound.

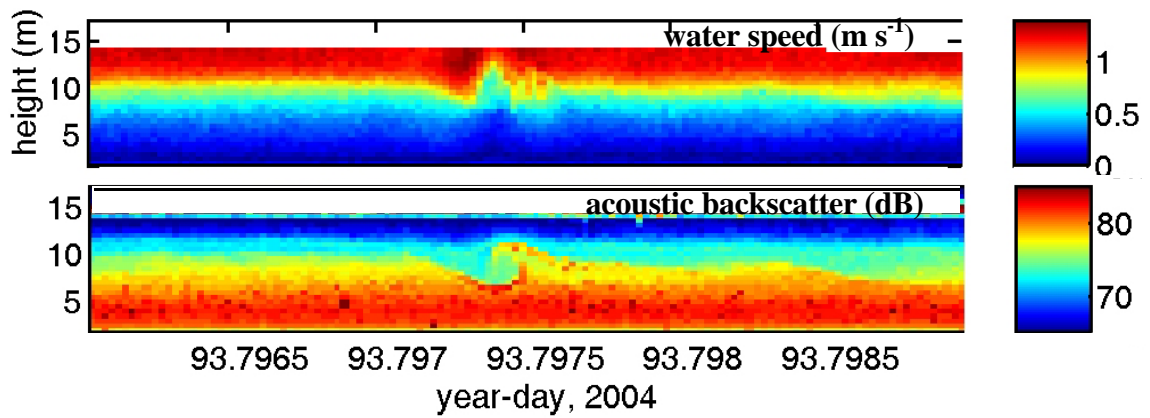


Figure 3: Five-minute timeseries showing a large instability at a 15 m deep site in the Hudson River estuary, measured with an acoustic Doppler current profiler. There is typically a two-layer flow at this location, with saline (dense) deep water and relatively fresh surface water. Turbulence driven by tidal currents in an unstratified estuary can produce near-surface turbulence and drive air-water exchanges of CO₂ [Zappa *et al.*, 2003], but little is known about these processes in stratified estuaries.

Chapter 2

VARIABILITY OF INTERNALLY GENERATED
TURBULENCE IN AN ESTUARY,
FROM 100 DAYS OF CONTINUOUS OBSERVATIONS¹

¹ previously published as: Orton, P.M. and Visbeck, M., 2009. Variability of internally generated turbulence in an estuary, from 100 days of continuous observations. *Continental Shelf Research*, doi:10.1016/j.csr.2007.07.008.

Abstract

We present detailed observations of internally generated turbulence in a sheared, stratified natural flow, as well as an analysis of the external factors leading to its generation and temporal variability. Multi-month time series of vertical profiles of velocity and acoustic backscatter (0.5 Hz) and turbulence parameters were collected with two moored acoustic Doppler current profilers in the Hudson River estuary, and estuary-long transects of water density were collected thirty times. ADCP backscatter is used for visualization of coherent turbulent structures and evaluation of surface wave biases to the turbulence measurements. Benefits of the continuous long-term turbulence record include our capturing: (1) the seasonality of turbulence due to changing riverflow, (2) hysteresis in stratification and turbulence over the fortnightly cycle of tidal range, and (3) intermittent events such as breaking internal waves. Internal mixing layers (IMLs) are defined as turbulent regions above the logarithmic velocity layer, and the bottom boundary layer (BBL) is defined as the continuously turbulent range of heights above the bed. A cross-correlation analysis reveals how IML and BBL turbulence vary with stratification and external forcing from tidal range, river flow, and winds. Turbulence in both layers is maximal at spring tide and minimal when most stratified, with one exception – IML turbulence at a site with changing channel depth and width is maximal at times of maximum stratification and freshwater input.

1. Introduction

Vertical turbulent mixing is a primary determinant of transport in all but the most stratified estuaries, with vigorous turbulence promoting retention, and stratification

promoting along-channel shear dispersion. A fundamental problem with numerical hydrodynamic modeling, however, is the incomplete representation of the nonlinear physics of turbulence. Numerical models require turbulence parameterizations because of computer processing constraints, but studies have shown that the many available schemes do not reflect turbulence variability over a wide range of stratification [e.g., *Sharples*, 2005; *Stacey et al.*, 1999b].

An important goal, if we are to understand estuarine transport dynamics and improve numerical models, is to obtain a more complete database of field observations of turbulence parameters. Whereas turbulence parameterizations can be indirectly tested by the ability of a model to reproduce the mean flow or salinity field, a more critical test is the ability to describe the depth dependence and time evolution of turbulence [*Simpson et al.*, 1996]. Studies have clarified the important role of bottom boundary layer (BBL) turbulence in estuaries [e.g., *Chant et al.*, 2007; *Geyer et al.*, 2000], a process that is well-predicted by model parameterizations.

It has long been known that along-estuary bathymetric variations or the presence of strong stratification and shear can cause "interfacial" turbulence (e.g. internal wave breaking) at a sharp estuarine pycnocline [*Chant and Wilson*, 2000; *Geyer and Smith*, 1987; *Peters*, 1999; *Stenström*, 2004]. Furthermore, turbulence above the logarithmic velocity layer is generated by local shear instabilities and modified by stratification (if present), not directly generated by bottom friction [*Peters and Bokhorst*, 2000]. These forms of turbulence, hereafter referred to as internal mixing layer (IML) turbulence (**Figure 1**), have higher mixing efficiency than BBL turbulence due to the stronger vertical gradients in water properties [*Lewis*, 1996; *Rippeth et al.*, 2005]. It has been acknowledged that IML

turbulence is a more difficult modeling task [*Sharples, 2005; Simpson et al., 1996*]. However, few full water column studies of turbulence have been carried out because methods for observing a full vertical profile of turbulence parameters have until recently required costly ship-based measurements.

Recent advances in acoustic Doppler current profiler (ADCP) techniques for observing turbulence are now enabling researchers to measure turbulence parameters autonomously for multiple days and through most of the water column [*Gargett et al., 2004; Lu and Lueck, 1999; Stacey et al., 1999a*]. The result is an increasing number of studies of ephemeral turbulence events at the ocean's margins, including tidal bores [*Simpson et al., 2004*], storm-driven Langmuir supercells [*Gargett et al., 2004*], and dense deepwater gravity currents [*Peters and Johns, 2006*].

Here, we contrast the variability of IML and BBL turbulence in the Hudson River estuary using two continuous 100+ day ADCP velocity, turbulent stress, and acoustic backscatter datasets and 30 along-estuary CTD transects. Although our observations span time scales from seconds to seasons, in this paper we primarily focus on the sub-tidal signals. A cross-correlation analysis reveals how IML and BBL turbulence vary with stratification and external forcing from tidal range, river flow, and winds. Significant correlations are discussed and in most cases matched with physical explanations. We synthesize these results by discussing the broader implications of IML turbulence variability in terms of estuarine modeling, circulation, fine sediment and pollutant transports, and air-water gas exchange.

2. Field Program and Data Processing

Ongoing monthly along channel CTD transects have now been run 30 times from The Battery (km 0) to Green Island, NY (km 243) since 2001, with the aid of the Hudson Riverkeeper. A Seabird SBE-19+ CTD is used for profiling along the estuary's thalweg (deepest cross-sectional location) to best track the salt intrusion, and data are bin-averaged to 0.5 m vertical resolution. Acoustic Doppler current profiler (ADCP) tripods were deployed on the bed of the Hudson (**Figure 2**) near Piermont (Site B; 3/24/04 - 7/12/04) and at the Hudson Highlands entrance sill in northern Haverstraw Bay (Site C; 3/24/04 - 7/3/04). Each held a Teledyne-RDI (TRDI) ADCP (Workhorse Monitor, 1200kHz) facing upward to monitor water velocity and acoustic backscatter through the water column. Continuous density estimates are available for the Site B tripod (at $z = 0.5$ m), surface water 6 km southward [USGS, unpublished data at Hastings-on-Hudson, 2004], and at surface and bottom water C-T sensors about 6 km south and 12 km north of Site C [R. Geyer, unpublished data, 2004].

Ambient conditions during the ADCP deployments covered nearly the complete range of riverflow, tidal and wind forcing that act upon the Hudson (**Figure 3**). Freshwater input (Q) at the head of the tidal river peaked at $1800 \text{ m}^3 \text{ s}^{-1}$ (twice), and bottomed out at $130 \text{ m}^3 \text{ s}^{-1}$. The 1980-2004 Q data show a mean of $400 \text{ m}^3 \text{ s}^{-1}$, and in a typical year, Q varies by a factor of 25, with means for annual minimum and maximum of $90 \text{ m}^3 \text{ s}^{-1}$ and $2340 \text{ m}^3 \text{ s}^{-1}$ [USGS, 2006]. Water depth from Site B shows significant fortnightly variability in tidal range, including a minimal apogean neap tide. A continuous wavelet transform (CWT) was used to quantify tidal forcing, decomposing these data into semi-diurnal (D2) and diurnal (D1) species, as well as several overtide and sub-tidal species. The

fundamental benefit of the CWT over traditional harmonic analysis is that it resolves the time-variation of frequency content, with no assumption of stationarity [Flinchem and Jay, 2000]. Wind stress was computed from wind observations off the mouth of the Hudson in New York Bight [NOAA, 2006] using a quadratic drag law $\tau_w = \rho_{\text{air}} C_d U_w^2$. Here, the air density ρ_{air} is 1.2 kg m^{-3} and the sea surface drag coefficient C_d is 0.001 [Large and Pond, 1981]. The 8-hour average wind speed was as high as 20 m s^{-1} in one isolated stormy period ($\tau_w = 0.45 \text{ Pa}$), but more typical wind maxima were $10\text{-}13 \text{ m s}^{-1}$ ($\tau_w = 0.1\text{-}0.2 \text{ Pa}$).

2.1 ADCP turbulence sampling and processing

ADCP sampling characteristics and processing were optimized for two months of turbulence sampling per deployment, given battery (3-57V D-cell stacks) and memory (2 GB) limitations. TRDI's rapid sampling mode-12 was used to record one ensemble average every 2 s, an average of 15 sub-pings that were collected over about $\sim 0.6 \text{ s}$ (40 ms intervals). The vertical cell size was 0.5 m, and the resulting manufacturer estimate of velocity standard error is 1.5 cm s^{-1} . Velocity and turbulent stress data were rotated from the earth reference frame into the direction of maximum near-bed velocity variance, to an along-stream (x) and across-stream (y) orthogonal reference frame. Data from the upper 6% of the water column were omitted, a standard procedure required because of acoustic side-lobe reflections off the sea surface, so data is available from 1.75 m above the bed to $\sim 1 \text{ m}$ below the sea surface.

ADCP data were used to compute 20-minute averages of the along- and across-stream vertical turbulent stress (τ_{xz} , τ_{yz}), turbulent kinetic energy production (P), and eddy viscosity (A_z) with 5-minute increments through time (75% overlap). Researchers have

developed a methodology called the “variance method” for an ADCP, to measure these turbulence parameters with minimal spatial averaging. Assuming that instrument tilts are negligible (they were below 2° at all times), and that second-order moments of the flow (e.g. $\overline{u'^2}$, $\overline{u'w'}$) are horizontally homogeneous between beams, we compute turbulent stress [Lu and Lueck, 1999; Stacey et al., 1999a]:

$$\tau_{xz} = -\rho \overline{u'w'} = \frac{\rho(\overline{b_4'^2} - \overline{b_3'^2})}{4 \sin \theta \cos \theta} \quad \tau_{yz} = -\rho \overline{v'w'} = \frac{\rho(\overline{b_2'^2} - \overline{b_1'^2})}{4 \sin \theta \cos \theta} \quad (1, 2)$$

Here, b_i are along-beam velocities ($i = 1,2,3,4$), ρ is the water density, and θ is the angle each beam makes with the vertical axis. Prior studies comparing ADCP turbulence measurements to those from shear microstructure or bottom-mounted acoustic Doppler velocimeters have shown good correspondence [Lu et al., 2000; Rippeth et al., 2003; Simpson et al., 2005]. Our stress noise floor for periods with weak turbulence, based on methods described in Williams and Simpson [2004], is $\sigma_\tau = 0.015$ Pa.

Where there are non-zero stresses, kinetic energy of the mean flow is converted into small-scale turbulence, an energy flux measured by our ADCP as shear production of turbulent kinetic energy (P). This is computed directly from these stresses and the mean shear [Rippeth et al., 2002]:

$$P = \tau_{xz} \frac{\partial \bar{u}}{\partial z} + \tau_{yz} \frac{\partial \bar{v}}{\partial z} \quad (3)$$

Here, we assume that shear production is dominant, and convective motions are negligible. Simpson et al. [2005] demonstrated that buoyancy production due to overstraining is typically below 10% of turbulent energy production, and a much smaller contributor to tidally-integrated production.

The eddy viscosity (A_z) is also directly available from the ADCP measurements [Lu and Lueck, 1999]:

$$A_z = \frac{1}{\rho} \frac{P}{\left(\frac{\partial \bar{u}}{\partial z}\right)^2 + \left(\frac{\partial \bar{v}}{\partial z}\right)^2} \quad (4)$$

2.2 ADCP turbulence quality control

Quality control for eight million vertical profiles of velocity, and resulting measurements of turbulence parameters, requires objective, automated methods for correcting or masking biased data. We blank out turbulence data in regions with frequent occurrence of negative TKE production [Rippeth *et al.*, 2003], likely indicating low turbulence levels or very small turbulent length scales. Surface waves can lead to a bias in τ due to the presence of strong non-turbulent water motions [Rippeth *et al.*, 2003], and researchers often manually detect wave bias by looking for cases where stress increases up to the sea surface. We have developed a conservative technique where the coherence between a given beam's sea surface height (h_i ; measurement discussed below) and its raw along-beam velocity (b_i) is used to identify depths and periods with potential for wave bias. This is particularly useful because it is an objective technique and depends only on ADCP measurements. If the coherence between h_i and b_i at any frequency is 0.1 or above, we blank out that data cell and all above it. Using this technique, we omitted data at depths greater than 4 m 21% of the time, and greater than 10 m 2.5% of the time.

A comparison of low and high-resolution datasets is typically used to estimate the low-bias in stress due to averaging in time and space, resolution bias [Lu *et al.*, 2000; Rippeth *et al.*, 2002]. We estimate resolution bias by averaging neighboring beam velocity

data in pairs (temporally or vertically) to create a new dataset with half the sample density (the "low resolution" dataset), and compare the resulting Reynolds stress estimates in linear regressions against those obtained with the full data set (the "high resolution" dataset).

Using this approach, we estimate that stress is underestimated on average by 23% due to resolution bias, and scale our stress observations up by this percentage.

2.3 Acoustic backscatter observations of turbulent structures and sea-surface height

An important component of our ADCP dataset is the acoustic backscatter (ABS), which has successfully been used in estuaries to observe coherent turbulent structures [e.g., *Geyer and Smith, 1987; Seim and Gregg, 1994*]. Acoustic backscatter data were corrected for range-dependent spreading and attenuation [*Deines, 1999*]. We also use raw ABS data from each beam separately to obtain a time series of sea surface height, h_i [*Visbeck and Fischer, 1995*]. This method has much higher resolution than the vertical cell height, because a parabolic fit of ABS is used to more precisely estimate h_i . ABS was linearly detrended prior to surface height detection to account for possible strong ABS from suspended sediment. This approach is useful for surface wave detection, though our mode-12 subsample averaging smooths h_i over ~ 0.6 second periods, causing underestimation of the height of high-frequency waves. One must have at least two samples per wave period for detection, so the maximum frequency wave we can detect is 0.25 Hz.

3. Analyses

Computations using the data described above include turbulence parameters, boundary layer heights, and cross-correlation analyses that relate an integral measure of

turbulence to external variables. Bed stress, τ_b , was computed using linear regressions toward the bed of the bottom five stress measurements in the water column (at heights of 1.75 - 3.25 m). ADCP measurements of the mean squared shear [*Geyer and Smith, 1987*] were computed using 30-second velocity averages:

$$S^2 = \overline{(\partial u / \partial z)^2 + (\partial v / \partial z)^2} \quad (5)$$

Estimates of the local buoyancy frequency were computed using the CTD transect data:

$$N = [(g/\rho)(\partial\rho/\partial z)]^{0.5} \quad (6)$$

The full water column "bulk" buoyancy frequency was computed similarly, using only the surface and bottom density estimates near the ADCP sites. Mean squared shear was averaged over the full water column and combined with bulk buoyancy to compute the bulk gradient Richardson number:

$$Ri_{\text{bulk}} = N^2/S^2 \quad (7)$$

The Richardson number is useful for diagnosing the dynamic stability of the water column, with values below 0.25 typically indicating potential for instability [*Geyer and Smith, 1987*].

3.1 Layer definitions

Basic features of the turbulence observations motivate a quantitative separation into bottom boundary layer (BBL) and internal mixing layer (IML) turbulence. Shear velocity ($U_* = (\tau_b/\rho)^{0.5}$) cubed should correlate well against depth-integrated shear production when turbulence is strong, if bed friction is the dominant mechanism for turbulence generation [*Lewis, 1996; Peters and Bokhorst, 2000*]. At Site B, a moderate correlation is

observed, with 52% of the variance in vertically integrated P being explained by U_*^3 (**Figure 4**). This correlation would likely be higher if we had more reliable estimates of τ_b ; our method relies on extrapolation toward the bed. Nevertheless, at Site C, there are clearly two regimes -- one where turbulence is strong yet U_* is small, and another where the two variables correlate more strongly.

The general concept of separating IML and BBL turbulence was presented by Dyer [1997, p.53], wherein the IML and BBL can overlap (**Figure 1**). We loosely follow that model and define IML turbulence as that which is detected above the top of the logarithmic velocity layer. This definition quantifies turbulence that is not a direct result of frictional forcing from the bed. The height of the logarithmic velocity layer (δ_{\log}) was computed following methods given in Lueck and Lu [1997], and is the highest level to which there is a regression with no more than 1% discrepancy between observed and best-fit velocity. The minimum possible successful fit gives $\delta_{\log} = 2.75$ m, using the first three ADCP velocity bins for a 3-point linear regression. This is likely to be an outer log layer, not related to skin friction, and we typically do not observe a constant turbulent stress in the layer. The tidal maximum δ_{\log} was typically about half the total water column depth during spring tides. Waves typically accompanied strong wind stress events, so no direct wind generated turbulence was detected without being masked to avoid wave bias in τ_z (**Sec. 2.2**).

We define the bottom boundary layer (BBL) as the continuously turbulent range of heights above the bed, capped by either (a) a zero intercept (stress) in a regression of near-bed stress versus height, or (b) the height where turbulent stress is not detected (where there are two successive omitted turbulent stress measurements in the quality-control procedures summarized in **Sec. 2.2**). In case (a), the top of the bottom boundary layer (δ_{BBL}) is

identified using linear extrapolation of the lower water column ($z \leq 3.8\text{m}$; 5 data points) stress profile upward to find a z -intercept. The 20-minute average turbulent stress profiles typically are linear through most of the BBL. However, only regressions with $r^2 > 0.7$ are used for estimating δ_{BBL} , and otherwise, the most recent height estimate is maintained. Resulting values for δ_{log} and δ_{BBL} were de-spiked with a 5-point median filter (25 minutes) and are presented and discussed in **Sec. 4**.

3.2 Cross-correlation analyses

A cross-correlation analysis enables us to examine how IML and BBL turbulence at each site responds to external forcing such as tidal range, wind, and freshwater input at Green Island (**Table 1**). Production (P) is a useful integral measure of turbulence, and when tidally averaged, is directly proportional to energy dissipation and buoyancy flux [*Rippeth et al.*, 2003]. The integrated production (P_{int}) in the bottom boundary layer and internal mixing layer were computed by integrating P over these layers and over successive 24.84-hour periods (one tidal day), though this was limited to the depths where we have measurements (**Figure 3g,h**).

"Driver variables" in the correlation analysis include external forcing parameters riverflow (squared, Q^2), east-west and north-south wind velocity (cubed, $U_{\text{wind},1}^3$ and $U_{\text{wind},2}^3$), and semidiurnal tidal range (cubed, $D2^3$). Additionally, the bulk buoyancy frequency squared (N^2) was utilized as a driver variable, to examine the role of local stratification effects. The powers for the driver variables were chosen to represent expected physical behavior, considering for instance that P_{int} (or dissipation) should be proportional to velocity cubed and velocity should be proportional to wave height. These powers also

generally showed the most significant correlations, when contrasted against correlation analysis results using other powers.

We estimate significance for the correlations using a bootstrap technique that accounts for temporal autocovariance in driver variables [*Martinson and Iannuzzi, 2003*]. Synthetic time series are created with identical mean, variance and power spectra as the driver variable. The driver variable's power spectrum is inverted with random phase, to create a synthetic "colored noise" time series, which is then cross-correlated against P_{int} . The result of 1000 repetitions is an empirical PDF of maximum (across all lags) absolute value correlation coefficients, from which we can see the number of times our regression coefficient was exceeded by random chance. Taking the maximum over all lags conservatively assigns significance, but is appropriate because we are presenting maximum coefficients over all lags for our results table. The maximum lag in the cross-correlation analysis was chosen to be 8 tidal days, long enough to capture neap-spring tidal period relationships. Results are presented in **Sec. 4**, and discussed in **Sec. 5.3**.

4. Results

Along-channel CTD transects show that stratification generally increases with decreasing semi-diurnal tidal range (**Figure 5**). High riverflow increases stratification in saline regions of the estuary, and dramatically enhances the neap-spring variability in stratification (**Figure 6**). The 2004 transects and bottom water density time series (e.g. **Figure 3d**) show patterns that are consistent with this stratification climatology. Both sites exhibited large neap-spring variations in stratification, and salinity was lower at Site C due to its location near the head of the salt intrusion.

We present ADCP data in three forms: (1) close ups of neap-to-spring transitions for the two sites during a period of high riverflow (**Figure 7**), (2) 20-minute zoom-ins from within that figure to episodes of vigorous IML/BBL turbulence (**Figure 8a**) and IML turbulence (**Figure 8b**), and (3) profile averages for these zoom-in periods (**Figure 9**). Site B shows abrupt changes in the turbulence and velocity fields at day 95 due to the onset of a wind event (west-northwesterly winds at $10\text{-}15\text{ m s}^{-1}$), although the change in stratification appears to be gradual (**Figure 7a**). Turbulence is stronger on flood tide while there is stratification, then on ebb tide after the stratification is eliminated. At Site C, there appear to be two different patterns of velocity and turbulence (**Figure 7b**). Prior to the breakdown of stratification, velocity does not ebb at all near the bed, and shear is strong throughout the water column (**Figure 9b**). Turbulent stress magnitude maxima occur at mid-depth during ebb tides, and there are few signs of a turbulent bottom boundary layer. Approaching spring tide, which occurred on day 97, velocity becomes more uniform through depth. The largest turbulent stress is near the bed but turbulence occurs throughout the water column.

Strong episodes of IML turbulence are well-characterized by acoustic backscatter, with patterns resembling piled up billows [*Seim and Gregg, 1994*], breaking internal waves, waves distorted by shear, and widespread Kelvin-Helmholtz instabilities [*Strang and Fernando, 2001*]. At Site C, IML turbulence was strongest during stratified ebb tides, at the time when ebb currents were maximal and shear strong throughout the water column (**Figure 8**). Characteristic turbulent (Ellison) length scales are typically larger than the 0.5 m ADCP resolution (**Figure 9**), and ABS clearly identifies coherent turbulent structures. At Site B, IML turbulence is strongest at peak flood, but is also moderate in association with a

1-3 m thick shear layer ($0.15\text{-}0.25\text{ s}^{-1}$) that persists into slack tide. Length scales at Site B are similar to or larger than the ADCP resolution, and coherent events (likely sediment resuspension) are visible in ABS in the lower water column.

Cross-correlation results are shown in **Table 1**, and discussed in detail in **Sec. 5.3**. Here, we focus on correlations significant at the $>90\%$ level only, shaded in the table. Tidal range correlations are often highly significant, riverflow correlations are only significant for Site C, wind correlations are only significant in one case, and bulk buoyancy frequency correlations are very strong. Specifically, the correlation between Site B BBL P_{int} and D2 range is positive and significant at 1 tidal day lag ($\alpha = 0.001$), and for Site C BBL P_{int} and D2 range it is also highly significant at a 2 day lag ($\alpha = 0.001$). The correlation between Site B IML P_{int} and D2 range is significant at a 0 day lag ($\alpha=0.02$). The negative correlation between Site C IML P_{int} and D2 range is significant, with the largest correlation ($\alpha = 0.06$) when P_{int} minima trails D2 range maxima by 2 or 3 tidal days (i.e. trails spring tide). The positive correlation between Site C BBL P_{int} and Q is significant ($\alpha = 0.08$) with P_{int} trailing Q by 8 days, while the correlation between Site C IML P_{int} and Q is significant at a 0-1 day lag ($\alpha = 0.06$). Correlation results for P_{int} with wind were only significant for Site C IML P_{int} ($\alpha=0.04$), which would indicate that turbulence is strong three days before a period with a strong east wind. Significant negative correlations exist for Site B and C BBL P_{int} with bulk N^2 ($\alpha=0.03$ and $\alpha=0.02$), and a highly significant positive correlation exists for Site C IML P_{int} with bulk N^2 ($\alpha<0.001$). The relationship between N and IML turbulence is further demonstrated in **Figure 10**.

5. Discussion

To our knowledge, ours is the first study to contrast the intensity and variability of observed estuarine IML and BBL turbulence over a broad range of forcing. Furthermore, the sites provide a sharp contrast; Site B is more representative of channelized "rectangular" estuary dynamics, while Site C is a region with changing channel depth and width near the head of the salt intrusion. At Site C, the proportion of turbulence occurring in the IML is often near 100%, with no log layer. At Site B, the proportion typically varies from 30-60% (**Figure 10**). A prior study evaluating the relative magnitude of observed log layer and IML turbulence between George Washington Bridge and The Battery also found that IML turbulence was strong, but also found that the depth-averaged dissipation was generally well-predicted as bed-driven (logarithmic layer) shear production [*Peters and Bokhorst, 2000*].

Some limitations to the scope of our study are worth mentioning. Our ability to quantify turbulence close to the sea surface, seafloor and in weakly turbulent stratified regions (e.g. the pycnocline in certain cases) is limited due to the half-meter vertical averaging length and the fact that the ADCP cannot collect data at the upper and lower edges of the water column. The majority of shear production and dissipation is expected to occur below 1.75 m when turbulence is bottom-driven [*Peters and Bokhorst, 2000*], so our observations of BBL P_{int} may be underestimates, if one is interested in flow energetics. Finer-scale measurements will be useful to shed further light on turbulence in these regions, and we recommend microstructure surveys alongside long-term ADCP measurements.

This is also the first published account where the ADCP variance method was used to study IML turbulence, and the first study of (at times) strongly stratified conditions (local

$N > 0.1 \text{ s}^{-1}$), so we cannot take for granted that the turbulence observations are not biased by internal waves during these periods. Below, we address this concern and briefly examine the mechanisms driving shear and turbulence at both sites. We then contrast variability in IML and BBL turbulence on timescales of days to seasons, the main focus of this paper. We conclude **Sec. 5** by discussing the implications for estuarine transports, residence times and air-water gas transfer.

5.1. Forcing of Site C IML turbulence

Site C exhibits unusual IML turbulence patterns never before observed at this level of detail in the Hudson, yet they are robust and physically sensible considering local bathymetry and observed currents. The patterns fit more closely to the isolated turbulence layers concept of **Figure 1b**, though in many cases the BBL is non-existent or confined very close to the bed. Bottom friction is clearly not driving turbulence during and after neap tide, as P is highest during ebb tide when near-bed currents are near zero (**Figure 7b**). Strong ebb currents flow over the slowly flooding near-bed layer, exhibiting strong shear. This occurs because there is a $\sim 1\%$ downward slope toward the north and a sharp slope to isopycnals at neap and post-neap transitional tides (**Figure 5**) that leads to an up-estuary baroclinic pressure force near the bed. Stenstrom [2004] used a numerical model in non-hydrostatic mode (on a coarse grid; not a large eddy simulation) to examine the role of bed slope and channel width in the Hudson. He concluded that turbulent mixing was highly dependent upon local bed slope.

ADCP stress observations from a period such as that shown in **Figure 8b** should be reliable because the assumptions of the variance method (**Sec. 2.1**) are likely to be valid.

One assumption is for horizontal homogeneity – the first statistical moments (e.g. \bar{u}) of the flow must be uniform across the ADCP beam spread in order to accurately observe the mean velocity, and the second statistical moments of the flow (e.g. $\overline{u'^2}$, $\overline{u'w'}$) must be uniform across the beam spread to observe the turbulent stress with the variance method. Lu and Lueck [Lu and Lueck, 1999] suggested a simple test of the former assumption: The averaging time should greatly exceed L/U , the distance between beams divided by the mean velocity. At mid-depth, the beam spread is about 5 m, the mean along-stream velocity is 0.5 m s^{-1} , and the ratio L/U equals 10 s, over two orders of magnitude lower than the averaging time of 20 minutes; thus, the assumption is reasonable for first moments. The second moments, when computed over 20-minute periods, should generally not vary over dramatically smaller distances than the first moments, so the second assumption is also likely valid.

The vertical excursions of acoustic backscatter (ABS) and strong aperiodic vertical velocities in **Figure 8b** support our contention that the high stress and P measurements reflect true vertical momentum and mass fluxes. ABS shows angled features that start high in the water column and migrate down in the water column over periods of about one minute. In an estuary, a common interpretation for peaks in ABS (away from the bed) is that they identify regions of turbulent salinity microstructure [Seim, 1999]. We interpret these ABS maxima as regions with small-scale turbulence at the edges of large-scale turbulent billows that are piling upon one another and being deformed due to the strong shear. The downward phase propagation of the features is due to the upper part a given billow (at 10 m) being moved much more rapidly downstream than the lower part (at 5 m).

The bulk Richardson number is somewhat useful for understanding the forcing of turbulence at this site, when combined with clues from the CTD database. The period shown in **Figure 8b** exhibits a Ri_{bulk} of 0.23. Shear is spread through the water column, whereas CTD profiles at this site from periods with similar conditions show that the vertical density gradient occurs over a much smaller range of depths, in a pycnocline. The *local* Richardson number in the pycnocline should be higher than the *bulk* Richardson number for such a period. Therefore, it is likely that the local gradient Richardson number at the pycnocline for **Figure 8b** was above 0.25, and mixing was a one-way upward entrainment process, not a two-way diffusion process – a particular challenge for numerical models [Sharpley, 2005]. Moreover, during the hour leading up to this highlighted period, Ri_{bulk} was from 0.25 to 0.75, and the local Richardson number in the pycnocline was likely higher. There were isolated yet periodic turbulent events evident in ABS, w , and turbulent stress during this period.

There is a minimum in channel width just north of Site C, where Stony Point cuts into the channel [**Figure 2**; Nitsche *et al.*, 2007], which could trigger internal hydraulic effects impacting Site C during stratified ebb tides. A lateral constriction can spawn trains of turbulent billows or internal waves [e.g., Geyer and Smith, 1987; Seim and Gregg, 1994], possibly explaining some of our observations described above. The importance of lateral constrictions for turbulence in the Hudson has been examined around the channel constriction at George Washington Bridge [Chant and Wilson, 2000; Peters, 2003; Stenström, 2004]. Our long-term observations at Site C broaden our understanding of the impact of riverflow and tidal range on IML turbulence in a region with rapidly changing bathymetry (**Sec. 5.3**).

5.2. Forcing of Site B IML turbulence

Site B turbulence patterns fit more closely to the overlapping turbulence layers concept of **Figure 1a**. The periods of strongest IML turbulence are during flood tides, when there is a local stress maximum between the bed and the mid-depth region of maximum shear (**Figure 8a**). The bulk Richardson number is not useful during stratified Site B flood tides, as it is above 0.25 even when BBL or IML turbulence is strong, and thus is not a good local measure of stability. Near the bed, vigorously turbulent velocities and pulses of high acoustic backscatter suggest that the local Richardson number is below 0.25 and shear instability is the turbulence generation mechanism.

Brief periods of strong turbulence are also often observed as vigorously turbulent front-like features pass the ADCP with very high near-surface acoustic backscatter, a common observation when ADCP measurements are made around sea-surface fronts [Marmorino and Trump, 1996]. A front at year-day 94.07 provided ~15% of the flood tide's IML TKE production, though turbulence was only elevated for about 10 minutes. Similarly, turbulence within 100 m behind a propagating river plume front was estimated to provide 20% of the total plume mixing [Orton and Jay, 2005].

A surprising result is the moderate shear production at Site B high in the water column during the slack after flood (e.g. day 94.13). One prior study of "direct" ADCP measurements of turbulent stress ($\overline{\rho u'w'}$, not utilizing the variance method) at the same semi-diurnal tidal phase in a more weakly stratified estuarine pycnocline found qualitative agreement with a small number of microstructure turbulence profiles [Ott et al., 2002]. In our data, these periods are responsible only for a small fraction of total IML turbulence (P_{int}), but warrant further analysis. The computed characteristic vertical length scale

(Ellison) is ~ 0.5 m, yet the integral horizontal length scale (L_H) for stress [Stacey *et al.*, 1999a] increases with height from ~ 2 m near the bed to ~ 50 m near the shear layer. This may reflect production of turbulence at the scales of internal gravity waves (e.g. sheared wave breaking), but may also reflect stress biases related to internal wave motions. A further possibility is convective motions, which have been shown to account for more than 10% of turbulent kinetic energy production at the end of flood tide in a partially mixed estuary [Simpson *et al.*, 2005]. To verify that internal waves were not biasing the results of our study, we separately computed stress in 15-second periods (with averaging afterward), excluding contributions to stress from longer-period motions. This conservatively excludes motions directly associated with internal waves, which have a maximum frequency of N – our CTD database shows N is always below 0.2 s^{-1} (2 cycles per minute) at the ADCP sites (**Figure 6**). Results of the new correlation analyses are highly similar to those displayed in **Table 1**. Nevertheless, these results underline the need for additional verification of ADCP stress measurements at the pycnocline in stratified shear flows.

5.3. IML and BBL turbulence variability on sub-tidal to seasonal timescales

The cross-correlation analysis summarized in **Table 1** and **Secs. 3.2 and 4** is useful for seeking external forcing agents that cause variability in Hudson IML and BBL turbulence. Results are generally consistent with strong tidal control (14 day period) of both BBL and IML turbulence, related to neap-spring variations in stratification. They are also consistent with riverflow exerting influence on both types of turbulence at Site C, with the interesting result that IML turbulence at that site increases during periods of high river flow. However, as with any correlation analysis, one cannot distinguish significant

correlations arising from physical connections from those that can be expected to arise from noise. Here, we examine the most significant correlations and seek consistent physical explanations.

Cross-correlation results suggest that fortnightly modulation of the semi-diurnal tidal range has a very strong effect on BBL and IML turbulence, though with varying phase. The highly significant positive correlations between BBL P_{int} and D2 tidal range at both sites are not surprising, as tides are generally understood to be the main drivers of BBL turbulence in partially mixed estuaries [Geyer *et al.*, 2000; Peters, 1999]. Turbulence in an estuarine BBL is produced due to interaction of tidal currents with the frictional bottom boundary, and because these current velocities increase with increasing tidal range, so does the intensity of the turbulence (to first order). D2 tidal range is inversely correlated with IML turbulence at Site C, with a two day lag (on average, P_{int} minima occurs 3 days after spring tide, during a post-spring transitional tide).

The phase lags of the significant Site C correlations between turbulence and tidal range represent a hysteresis pattern between turbulence in either layer and the fortnightly tidal phase, as shown in **Figure 11**. The pattern was strong in the first half of the study period, and moderate in the latter half. This pattern likely exists due to a similar hysteresis that occurs between D2 range and stratification (N^2) in the Hudson [Bowen and Geyer, 2003]. Hysteresis between stratification and tidal range is a fundamental feature in moderate depth (~20 m) partially mixed estuaries [MacCready, 1999]. The stratification hysteresis was also stronger in the first half of the study, likely due to weaker neap tides or unsteadiness of the estuarine circulation and salt intrusion in the face of rapidly changing riverflow and tidal forcing. For cycle #1 (**Figure 11**), during the post-spring transitional

tide, bulk N^2 was 25 times smaller than during the post-neap transition, for the same tidal range. During cycle #5, the difference in N^2 was only a factor of 4. The turbulence hysteresis likely follows the intensity of the stratification hysteresis, considering the strong in-phase correlations of N^2 with IML or BBL turbulence.

A likely mechanism for increased stratification (and decreased tidal range) increasing IML turbulence is increased shear due to increased baroclinic forcing. The strongest Site C IML turbulence for the first neap-spring cycle occurred from 2-5 days after neap, because neap tide up-estuary salt pumping built stratification to maximal levels, and mean vertical shear was as high as 0.14 s^{-1} (in contrast, the mean shear during spring tides is 0.04 s^{-1}).

Prior studies have observed impacts of strong winds in the Hudson, either through the indirect effect of sea-surface height forcing due to Ekman transport in the New York Bight [*Peters and Bokhorst, 2000*], or the more direct effect of wind shearing the upper water column [*Peters, 1999*]. Due to conservative removal of turbulence data with potential for wave bias (see **Sec. 2.2**), the only influence of wind on turbulence we may see in our data is through straining the density field or coastal sea level set-up. Our correlation analysis of wind and integrated TKE production (P_{int}), however, did not support the hypothesis of a substantial causal relationship. The one significant wind correlation is consistent with IML turbulence being strong three days before a period with a strong east wind, which does not appear to have any physical explanation. This result was strongly dependent on only one wind event that occurred during high riverflow soon after neap tide, so can be explained with other significantly correlated variables. Moreover, three other east-west wind events had no sign of elevated turbulence.

The spring season typically has higher riverflow (Q) into the estuary than any other season [USGS, 2006], with impacts on stratification and turbulence. Higher riverflow is associated with enhanced stratification, with the exception being cases where high riverflow spring tides flush all stratification seaward of a given site. The summer season has the lowest riverflow, with the exception being rare storms. Positive correlations when BBL P_{int} lags 8 days behind Q at Sites B and C are marginally significant ($\alpha = 0.12$ and $\alpha = 0.08$, respectively). These correlations and the substantial lag may arise from the tendency for sustained high riverflow events (e.g. the freshet) to wash the salt wedge seaward of the site, reducing stratification to riverine levels and allowing stronger turbulence.

The impact of increasing riverflow on IML turbulence at Site C is unique, and likely related to local bathymetry, discussed in **Sec. 5.1**. The positive correlation between Site C IML P_{int} and riverflow is significant at a 0 or 1 day lag ($\alpha=0.06$ for both lags). This lag is reasonable, considering that approximating the travel time for changes in river stage from Green Island to the study area as shallow water wave propagation, $c = \sqrt{gh}$, gives a travel time of six hours.

The mechanism for increased river flow increasing IML turbulence at Site C is not clear because it should increase barotropic forcing, not baroclinic forcing, so have little effect on shear. Possible mechanisms are: (1) Shear can be set up by differential friction on the bottom layer, with an effect much like that of a baroclinic pressure gradient force [Monismith and Fong, 1996]. (2) Increased internal hydraulic effects, which can cause IML turbulence regardless of the local Richardson number. An increased barotropic pressure gradient likely drives stronger ebb currents in both the surface and bottom layers at Stony Point, increasing the two-layer composite internal Froude number, $G^2 = u_1^2/(g'h_1) +$

$u_2^2/(g'h_2)$, where g' is reduced gravity $g(\rho_0 - \rho_1)/\rho$, u is velocity, h is layer thickness, and subscripts denote layer numbers [Armi, 1986]. The Hudson is mostly confined to a channel by geologic features, and this result might not be observed in estuaries with a larger floodplain, where high riverflow may not necessarily increase ebb tide currents.

There was moderate correlation between Site C bulk N and riverflow during the study period ($r^2 = 0.22$). The cross-correlation analysis shows that stratification has a very strong influence on IML turbulence, so it is useful to look at how riverflow improves that correlation when added in a multiple linear regression. It is important to only consider cases where Site C has moderate stratification, which is required for all the mechanisms discussed above. Including cases of bulk $N > 0.05 \text{ s}^{-1}$ only, a linear regression of IML P_{int} with N^2 gives an r^2 value of 0.46, whereas adding Q^2 in a multiple linear regression gives an improved r^2 of 0.61. That is, when at least mildly stratified, a linear model of IML P_{int} that includes stratification and riverflow performs substantially better than one including only stratification.

5.4 Implications for estuarine circulation, modeling and transports

Studies have clarified the important role of bottom boundary layer (BBL) turbulence for estuarine circulation [e.g., Chant *et al.*, 2007; Geyer *et al.*, 2000], but few observational studies exist quantifying IML turbulence and its role. Here, we have shown that IML turbulence, represented by TKE production, is maximal when the BBL turbulence in the estuary is at a minimum (**Figs. 3, 10, 11**) – during a neap or post-neap transitional tide, and (for Site C) stratified periods with high river input. The observed intensity and temporal variability for IML turbulence also has important implications for scalar transports, because

vertical fluxes of buoyancy and dissolved constituents in stratified waters are approximately proportional to P . Moreover, these observations suggest that the mixing efficiency may be at its highest during neap and post-neap transitional tides, because IML turbulence acts near the pycnocline, whereas BBL turbulence predominantly stirs well-mixed water. Extrapolating our results to estuary-wide budgets will require observations with greater spatial coverage, but below we discuss several important implications of these observations for energetics and circulation modeling, then for scalar transports.

This increased importance of IML turbulence during neap and post-neap transitional tides provides an important test for estuarine models. These are the periods that have provided the greatest discrepancy between observed and modeled estuarine circulation from an analytical [Geyer *et al.*, 2000] and a numerical model [Warner *et al.*, 2005]. Our observations show that strong IML turbulence increases the drag on the upper layer flow during such periods, which should reduce the magnitude of the estuarine exchange velocity. Models developed with the assumption that all turbulence is related to bed friction, or having mixing parameterizations that require manual adjustments for background turbulence, will generally have difficulty modeling circulation during neap and post-neap transitional tides. Modifying mixing parameterizations to better account for IML turbulence may improve model predictions.

Examining the Hudson's energy budget, Peters [Peters, 2003] concluded from microstructure turbulence measurements that the localized region of elevated IML dissipation near the George Washington Bridge (GWB) did not appear to be of great importance. However, that study acknowledged that only a narrow range of conditions were sampled. Our results show tidally-averaged pycnocline TKE production rates at Site

C that are as much as a factor of 10 higher than dissipation rates in that study, and suggest that the estuary-wide importance of IML turbulence at GWB should be re-evaluated for both high riverflow conditions and periods of peak stratification.

Our results have particularly strong implications for estuarine trapping of river-derived sediment and particle-associated pollutants during flood events such as the spring freshet. The buoyant fresh water and associated stratification that arrives with these constituents can weaken vertical mixing, yet our results suggest that IML turbulence in bathymetrically complex regions is increased during these periods. Fine suspended sediment transport should be highly sensitive to IML turbulence due to entrainment of saltwater into the upper layer and the non-linearity of flocculation. Flocculation is the aggregation of riverine particles when exposed to saline water, increasing settling rates by a factor of 10-100 [*Kineke and Sternberg, 1989*], typically with a threshold onset at salinities of 1-2 [*Dyer, 1986, p.204*]. In our observations, the surface salinity (1 m depth) is never below 2 at George Washington Bridge or southward, with riverflow as high as $1800 \text{ m}^3 \text{ s}^{-1}$. A significant fraction of river-derived fine sediments are therefore flocculating and settling to the bed, preventing or delaying export. Unsurprisingly, the Hudson appears to generally be depositional in the region south from GWB, except in rare ~ 10 year events where very high riverflow coincides with a spring tide [*Geyer et al., 2001*]. A model that doesn't accurately predict IML turbulence under a wide range of stratification will be less likely to predict these sediment trapping patterns accurately.

IML turbulence can enhance air-water gas transfer, as it increases turbulent overturning near the sea surface. This is illustrated in **Figure 7**, when Site C upper water column P is higher during post-neap transitional ebb tides than it is at Site B during

vigorously mixed spring tides, with sustained values of 10^{-1} W m^{-3} . P is roughly proportional to dissipation ϵ [Rippeth *et al.*, 2003], and gas transfer typically goes as dissipation near the sea-surface [Zappa *et al.*, 2007], so high IML P should enhance air-water gas transfer. The role may be especially important around sea-surface fronts (where the IML intersects with the sea-surface) which we found to cause 15% of P_{int} at Site B, and also cause bubble injection [Marmorino and Trump, 1996]. Moreover, many pollutants that are remobilized during floods and freshets (e.g. PCBs, N_2O , PAH) have a gaseous phase and thus their transport (and possible evasion from water to air) will be particularly affected by IML turbulence during these stratified periods.

6. Summary and Conclusions

We have used along-channel density transects and two continuous 100-day full water column turbulence datasets to characterize stratification and turbulence in the Hudson River estuary. Separately, we quantify bottom boundary layer (BBL) and internal mixing layer (IML) turbulence, the latter of which is increasingly being recognized for its importance for scalar transports in the coastal ocean [Rippeth, 2005]. The ADCP sites are chosen to maximize dynamical contrast, and thus display a diverse range of turbulence processes; Site B is in channelized regular bathymetry, while Site C is in a region of more complex bathymetry, with depth increasing up-river. While extrapolating our results to estuary-wide budgets will require measurements at a wider range of along-channel locations, several important conclusions are reached.

Prior studies have suggested that BBL turbulence dominates in the Hudson, at least for estuarine dynamics [Chant *et al.*, 2007; Geyer *et al.*, 2000], and our results for Site B

generally do not contradict those. However, we observe relatively strong IML turbulence that doesn't fit that model during neap or post-neap transitional tides (between neap and spring), and that is particularly strong and independent of bed-stress at Site C. This expands upon the findings of Stenstrom [2004], who showed with a non-hydrostatic numerical model of the Hudson that IML mixing is spatially variable, with turbulent mixing during stratified periods highly dependent upon local bed slope.

A major advantage of ADCP turbulence measurements is that our long-term autonomous deployments also capture the role of unpredictable extremes in riverflow and wind, as well as extreme tides. While bottom boundary layer turbulence is generally dominant at spring and post-spring transitional tides in the estuary, we find an increasing relative magnitude for IML turbulence at times of maximum stratification (at neap or the post-neap transition) and riverflow. Duplication of these differing patterns of BBL and IML turbulence provides a stringent test for numerical models, but an important one if they are to accurately predict transports of constituents through partially mixed or highly stratified estuaries.

References

Armi, L. (1986), The hydraulics of two flowing layers with different densities, *J. Fluid Mech.*, 163, 27-58.

Bowen, M., and W. Geyer (2003), Salt transport and the time-dependent salt balance of a partially stratified estuary, *J. Geophys. Res.*, 108(C5), 3158.

Chant, R., and R. Wilson (2000), Internal hydraulics and mixing in a highly stratified estuary, *J. Geophys. Res.*, 105, 14.

- Chant, R. J., W. R. Geyer, R. Houghton, E. Hunter, and J. Lerczak (2007), Estuarine Boundary Layer Mixing Processes: Insights from Dye Experiments, *J. Phys. Oceanogr.*, 37(7), 1859-1877.
- Deines, K. (1999), Backscatter estimation using broadband acoustic Doppler current profilers.
- Dyer, K. (1986), *Coastal and estuarine sediment dynamics*, 358 pp., John Wiley and Sons, Chichester, Sussex (UK).
- Dyer, K. (1997), *Estuaries: a physical introduction*, 2 ed., John Wiley & Sons London.
- Flinchem, E., and D. Jay (2000), An introduction to wavelet transform tidal analysis methods, *Estuar. Coast. Shelf Sci.*, 51(2), 177-200.
- Gargett, A., J. Wells, A. Tejada-Martinez, and C. Grosch (2004), Langmuir supercells: A mechanism for sediment resuspension and transport in shallow seas, *Science*, 306(5703), 1925.
- Geyer, W., J. Woodruff, and P. Traykovski (2001), Sediment transport and trapping in the Hudson River Estuary, *Estuaries Coasts*, 24(5), 670-679.
- Geyer, W. R., and J. D. Smith (1987), Shear Instability in a Highly Stratified Estuary, *J. Phys. Oceanogr.*, 17(10), 1668-1679.
- Geyer, W. R., J. H. Trowbridge, and M. M. Bowen (2000), The dynamics of a partially mixed estuary, *J. Phys. Oceanogr.*, 30, 2035-2048.
- Kineke, G., and R. Sternberg (1989), The effect of particle settling velocity on computed suspended sediment concentration profiles, *Marine Geology*, 90(3), 159-174.
- Large, W. G., and S. Pond (1981), Open ocean momentum flux measurements in moderate to strong winds, *J. Phys. Oceanogr.*, 11, 324-336.
- Lewis, R. (1996), Relative contributions of interfacial and bed generated mixing to the estuarine energy balance, *Mixing in estuaries and coastal seas*, 250-266.

Lu, Y., and R. G. Lueck (1999), Using a Broadband ADCP in a Tidal Channel. Part II: Turbulence, *J. Atmos. Oceanic Technol.*, *16*(11), 1568-1579.

Lu, Y., R. G. Lueck, and D. Huang (2000), Turbulence Characteristics in a Tidal Channel, *J. Phys. Oceanogr.*, *30*(5), 855-867.

Lueck, R., and Y. Lu (1997), The logarithmic layer in a tidal channel, *Cont. Shelf Res.*, *17*(14), 1785-1801.

MacCready, P. (1999), Estuarine adjustment to changes in river flow and tidal mixing, *J. Phys. Oceanogr.*, *29*, 708-726.

Marmorino, G., and C. Trump (1996), High-resolution measurements made across a tidal intrusion front, *J. Geophys. Res.*, *101*(C11), 25661.

Martinson, D., and R. Iannuzzi (2003), Spatial/temporal patterns in Weddell gyre characteristics and their relationship to global climate, *J. Geophys. Res.*, *108*, 8083.

Monismith, S., and D. Fong (1996), A simple model of mixing in stratified tidal flows, *J. Geophys. Res.*, *102*, 28583-28595.

Nitsche, F. O., W. B. Ryan, S. M. Carbotte, R. E. Bell, A. Slagle, C. Bertinado, R. Flood, T. Kenna, and C. McHugh (2007), Regional patterns and local variations of sediment distribution in the Hudson River Estuary, *Estuar. Coast. Shelf Sci.*, *71*(1-2), 259-277.

NOAA-NOS (2006), National Oceanographic and Atmospheric Administration, National Ocean Service online data, <http://spo.nos.noaa.gov/bathy/>, accessed February 10, 2006.

NOAA (2006), National Oceanographic and Atmospheric Administration, National Data Buoy Center online data, <http://ndbc.noaa.gov/>, accessed February 10, 2006.

Orton, P. M., and D. A. Jay (2005), Observations at the tidal plume front of a high-volume river outflow, *Geophys. Res. Lett.*, *32*, L11605, DOI: doi:10.1029/2005GL022372.

Ott, M., R. Dewey, and C. Garrett (2002), Reynolds stresses and secondary circulation in a stratified rotating shear flow, *J. Phys. Oceanogr.*, *32*, 3249-3268.

Peters, H. (1999), Spatial and temporal variability of turbulent mixing in an estuary, *J. Mar. Res.*, *57*, 805-845.

Peters, H., and R. Bokhorst (2000), Microstructure observations of turbulent mixing in a partially mixed estuary. Part I: Dissipation rate, *J. Phys. Oceanogr.*, *30*, 1232-1244.

Peters, H. (2003), Broadly distributed and locally enhanced turbulent mixing in a tidal estuary, *J. Phys. Oceanogr.*, *33*, 1967-1977.

Peters, H., and W. Johns (2006), Bottom layer turbulence in the Red Sea outflow plume, *J. Phys. Oceanogr.*, *36*, 1763-1785.

Rippeth, T. P., E. Williams, and J. H. Simpson (2002), Reynolds Stress and Turbulent Energy Production in a Tidal Channel, *J. Phys. Oceanogr.*, *32*(4), 1242-1251.

Rippeth, T. P., J. H. Simpson, E. Williams, and M. E. Inall (2003), Measurement of the Rates of Production and Dissipation of Turbulent Kinetic Energy in an Energetic Tidal Flow: Red Wharf Bay Revisited, *J. Phys. Oceanogr.*, *33*(9), 1889-1901.

Rippeth, T. P. (2005), Mixing in seasonally stratified shelf seas: a shifting paradigm, *Philosophical Transactions of the Royal Society A: Mathematical, Physical and Engineering Sciences*, *363*(1837), 2837-2854, DOI: 10.1098/rsta.2005.1662.

Rippeth, T. P., M. R. Palmer, J. H. Simpson, N. R. Fisher, and J. Sharples (2005), Thermocline mixing in summer stratified continental shelf seas, *Geophys. Res. Lett.*, *32*, DOI: 10.1029/2004gl022104.

Seim, H., and M. Gregg (1994), Detailed observations of a naturally occurring shear instability.

Seim, H. (1999), Acoustic backscatter from salinity microstructure, *J. Atmos. Oceanic Technol.*, *16*, 1491-1498.

Sharples, J. (2005), Turbulence measurements in highly stratified estuaries, in *Marine Turbulence, Theories, Observations and Models*, edited by H. Baumert, et al., Cambridge University Press, Cambridge.

- Simpson, J., W. Crawford, T. Rippeth, A. Campbell, and J. Cheok (1996), The vertical structure of turbulent dissipation in shelf seas, *J. Phys. Oceanogr.*, 26(8), 1579-1590.
- Simpson, J., N. Fisher, and P. Wiles (2004), Reynolds stress and TKE production in an estuary with a tidal bore, *Estuar. Coast. Shelf Sci.*, 60(4), 619-627.
- Simpson, J., E. Williams, L. Brasseur, and J. Brubaker (2005), The impact of tidal straining on the cycle of turbulence in a partially stratified estuary, *Cont. Shelf Res.*, 25(1), 51-64.
- Stacey, M. T., S. G. Monismith, and J. R. Burau (1999a), Measurements of Reynolds stress profiles in unstratified tidal flow, *J. Geophys. Res.*, 104, DOI: 10.1029/1998jc900095.
- Stacey, M. T., S. G. Monismith, and J. R. Burau (1999b), Observations of Turbulence in a Partially Stratified Estuary, *J. Phys. Oceanogr.*, 29(8), 1950-1970.
- Stenström, P. (2004), Hydraulics and mixing in the Hudson River estuary: A numerical model study of tidal variations during neap tide conditions, *J. Geophys. Res.*, 109(C4), C04019.
- Strang, E., and H. Fernando (2001), Entrainment and mixing in stratified shear flows, *J. Fluid Mech.*, 428, 349-386.
- USGS (2006), United States Geological Survey National Water Information System (NWISWeb) online data, <http://waterdata.usgs.gov/nwis/>, accessed February 10, 2006.
- Visbeck, M., and J. Fischer (1995), Sea Surface Conditions Remotely Sensed by Upward-Looking ADCPs, *J. Atmos. Oceanic Technol.*, 12(1), 141-149.
- Warner, J. C., W. R. Geyer, and J. A. Lerczak (2005), Numerical modeling of an estuary: A comprehensive skill assessment, *J. Geophys. Res.*, 110, DOI: 10.1029/2004jc002691.
- Williams, E., and J. Simpson (2004), Uncertainties in estimates of Reynolds stress and TKE production rate using the ADCP variance method, *J. Atmos. Oceanic Technol.*, 21(2).
- Zappa, C., W. McGillis, P. Raymond, J. Edson, E. Hints, H. Zemmelen, J. Dacey, and D. Ho (2007), Environmental turbulent mixing controls on air-water gas exchange in marine and aquatic systems, *Geophys. Res. Lett.*, 34(10), 10601.

Figure Captions

Figure 1: Conceptual mixing layer diagram with salinity profiles and boundary layer heights (δ). Shown are examples of (a) the case where IML and BBL mixing interact, common in partially mixed estuaries, and (b) the case where the two layers are separate, common in highly stratified estuaries. Adapted from Dyer [1997, p.53].

Figure 2: Hudson River estuary coastline (left) with a zoom-in (right panel) to shaded NOAA-NOS [2006] bathymetry data, and ADCP sites marked '+'. Along-channel distance up-estuary from The Battery (rkm 0 line) is also shown in river kilometers (rkm).

Figure 3: Time series view of ambient conditions and turbulence variables during the ADCP deployments. Panel (a) shows freshwater input. Panels (b, c and d) show data derived from CTD observations at Site B (0.5 m above the bed), including total depth, semidiurnal (D2) and diurnal (D1) tidal ranges computed with a wavelet transform tidal analysis of depth, water density (σ_t). Panels (e) and (f) show estimates of bed stress (τ_b ; **Sec. 3**) at Site B, and wind stress (τ_w). Panels (g) and (h) show integrated turbulent kinetic energy production (P_{int} ; **Sec. 3.2**) for the IML and BBL. The dotted vertical line shows the beginning of the year day range for **Figure 7**.

Figure 4: Relationship between bed frictional forcing (U_*^3) and turbulence (vertically integrated shear production) for Sites B and C. For Site C, there appear to be two distinct regimes, one where turbulence increases with U_*^3 , and another where it is strong in spite of low U_*^3 .

Figure 5: Three along-channel density transects during spring freshet season, for (a) a weak spring tide (2004 year-day 111, riverflow $Q=470 \text{ m}^3 \text{ s}^{-1}$), (b) one day prior to neap tide (2004 year-day 117, $Q=740 \text{ m}^3 \text{ s}^{-1}$), and three days after neap tide (2005 year-day 108, $Q=400 \text{ m}^3 \text{ s}^{-1}$). Vertical red lines show the ADCP sites, and the thalweg depth is shaded black. The aspect ratio exaggerates bed topography, and actual bed slopes are rarely greater than one percent south of 41.2° N latitude. The salt intrusion length maximum typically lags behind the minimum in tidal forcing, with maximum intrusion length occurring during the post-neap transitional period (see **Sec. 5.3**).

Figure 6: Summary of stratification (local N) observations the Hudson, with respect to along-channel location (latitude), riverflow (Q ; prior 10-day mean) and semi-diurnal (D2; prior 5-day mean) tidal range. The plots summarize data from 30 along-channel transects like those in **Figure 5**, between 2001 and 2006. Horizontal dotted lines show Sites B and C. Each colored box shows the observed maximum water column stratification from a single profile (from 1.5 m vertical running averages of density). Symbols are (WP) West Point, (IP) Indian Point, (TZ) Tappan Zee Bridge, (GW) George Washington Bridge, and (TB) The Battery.

Figure 7: (a) Site B and (b) Site C zoom-ins of a neap-spring transition with high riverflow. Plotted variables are: density (σ_t), along-stream velocity (u), along-stream vertical shear ($\partial u / \partial z$), acoustic backscatter (ABS), turbulent stress (τ_{xz}), eddy viscosity (A_z), and turbulent kinetic energy production (P). Turbulence data is masked when it is

likely dominated by noise (blanked white) or side lobe and wave contamination (grey; see **Sec. 2.2**). The sea surface and bottom boundary layer height (black lines), and log layer height (white line) are shown. The vertical dotted lines show the times for the two figures that follow. Site C exhibits no log layer within our measurement range for most of this period.

Figure 8: Zoom-ins to 0.5 Hz raw data for 20-minute periods at (a) Site B, and (b) Site C. Shown are: along-stream velocity (u), vertical shear ($\partial u / \partial z$), vertical velocity (w), and acoustic backscatter from a single ADCP beam (ABS). For Site C, shear is box-filtered with a 1.5 m by 10 s window, due to excessive variability. The following plot shows averaged turbulent stress profiles from these periods.

Figure 9: (a) Site B and (b) Site C, 20-minute averages of data from the periods shown in the prior figure. From left-to-right are along-stream velocity, turbulent stress, and the characteristic (Ellison) turbulent length scale ($L_E \approx 3\sqrt{\tau_{xz} / \rho S^2}$) [Stacey *et al.*, 1999a].

Figure 10: Comparison of stratification (bulk buoyancy frequency, N , for Site B) with the percentage of total turbulence (integrated production) that occurs in the IML (% IML). IML turbulence takes on a relatively larger role during periods of strong stratification.

Figure 11: At Site C, post-neap transitional tides can have ~15 times higher (lower) IML (BBL) turbulence and mixing than post-spring transitional tides, a hysteresis pattern. The top panel shows the time series of semidiurnal (D2) tidal range, and the two periods shown

in the bottom panels are marked with squares and circles for each tidal day, respectively.

The lower panels show P_{int} for the bottom boundary layer (BBL) and internal mixing layer (IML). Since the buoyancy flux is roughly proportional to IML P_{int} [Rippeth, 2005], this hysteresis should also exist for the vertical mixing of dissolved constituents.

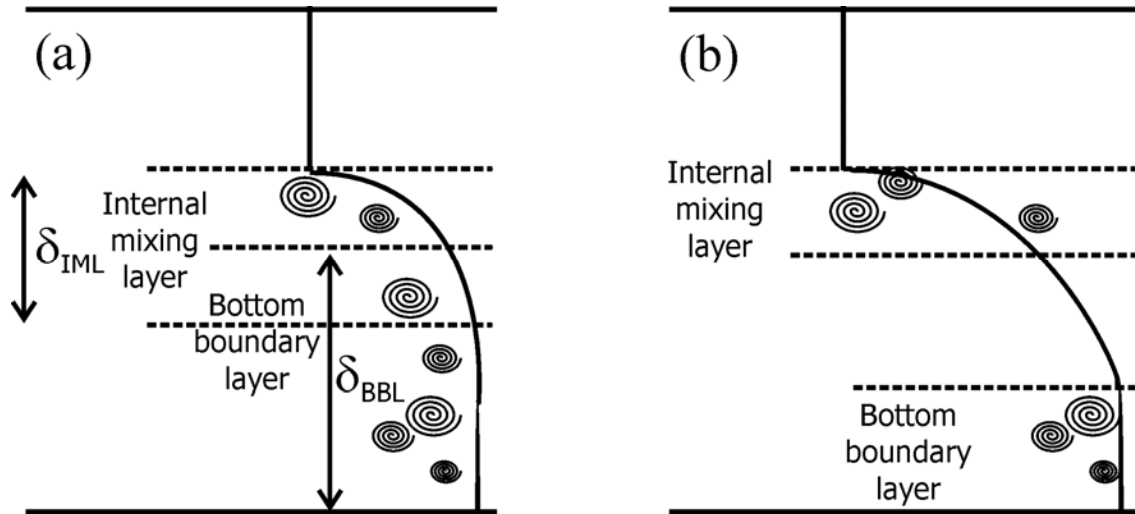


Figure 1: Conceptual mixing layer diagram with salinity profiles and boundary layer heights (δ). Shown are examples of (a) the case where IML and BBL mixing interact, common in partially mixed estuaries, and (b) the case where the two layers are separate, common in highly stratified estuaries. Adapted from Dyer [1997, p.53].

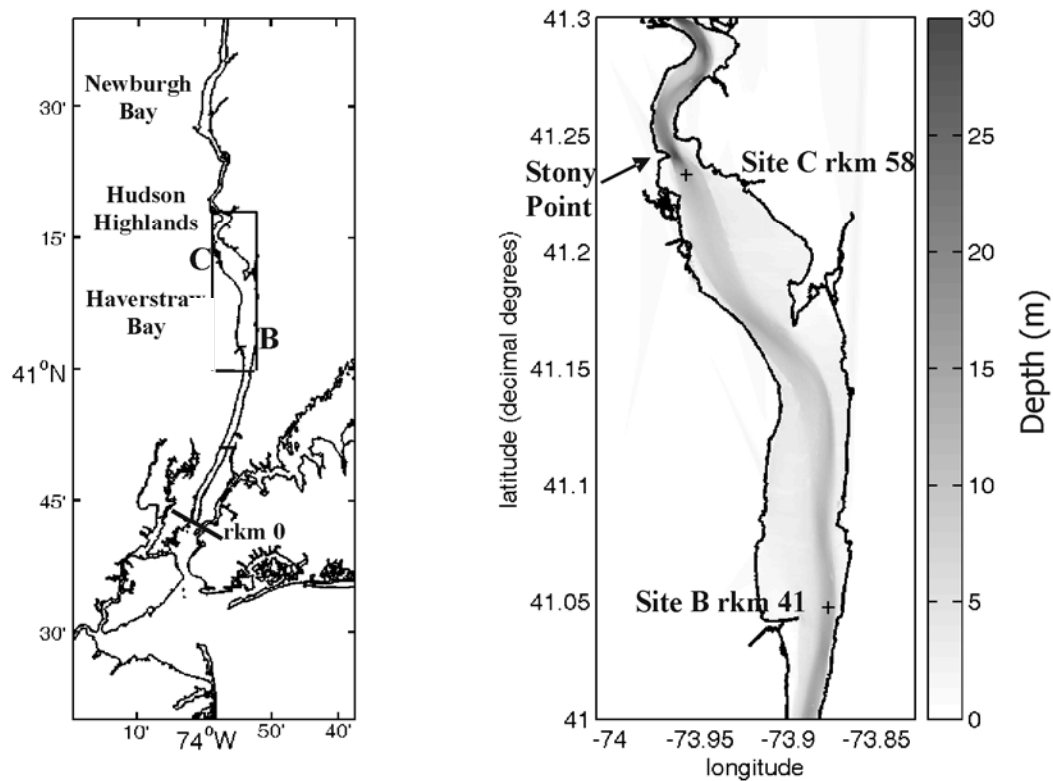


Figure 2: Hudson River estuary coastline (left) with a zoom-in (right panel) to shaded NOAA-NOS [2006] bathymetry data, and ADCP sites marked '+'. Along-channel distance up-estuary from The Battery (rkm 0 line) is also shown in river kilometers (rkm).

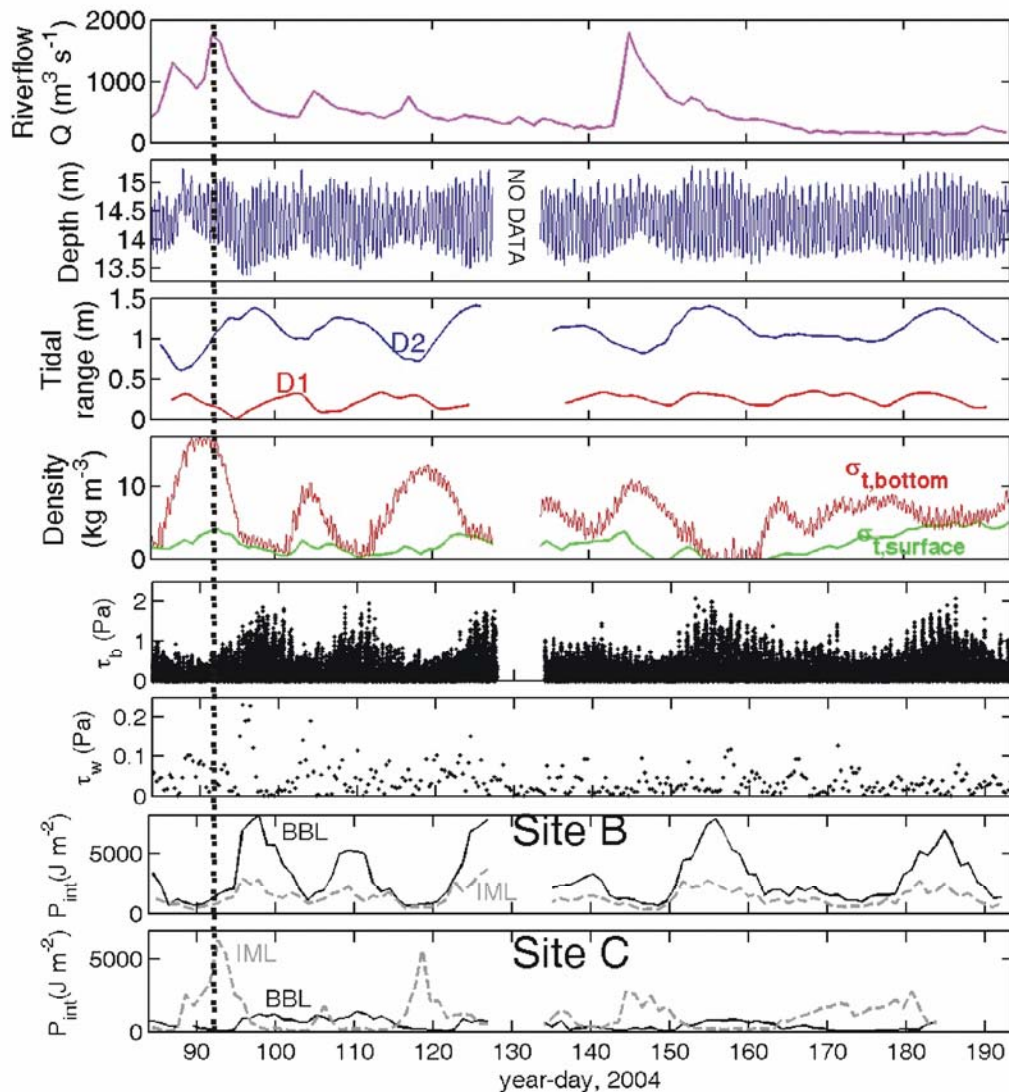


Figure 3: Time series view of ambient conditions and turbulence variables during the ADCP deployments. Panel (a) shows freshwater input. Panels (b, c and d) show data derived from CTD observations at Site B (0.5 m above the bed), including total depth, semidiurnal (D2) and diurnal (D1) tidal ranges computed with a wavelet transform tidal analysis of depth, water density (σ_t). Panels (e) and (f) show estimates of bed stress (τ_b ; **Sec. 3**) at Site B, and wind stress (τ_w). Panels (g) and (h) show integrated turbulent kinetic energy production (P_{int} ; **Sec. 3.2**) for the IML and BBL. The dotted vertical line shows the beginning of the year day range for **Figure 7**.

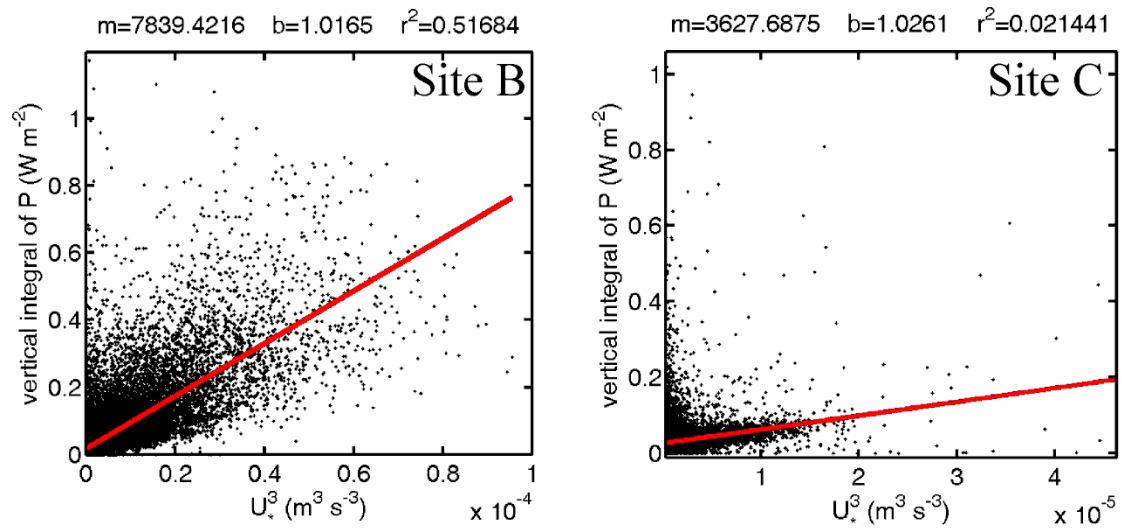


Figure 4: Relationship between bed frictional forcing (U_*^3) and turbulence (vertically integrated shear production) for Sites B and C. For Site C, there appear to be two distinct regimes, one where turbulence increases with U_*^3 , and another where it is strong in spite of low U_*^3 .

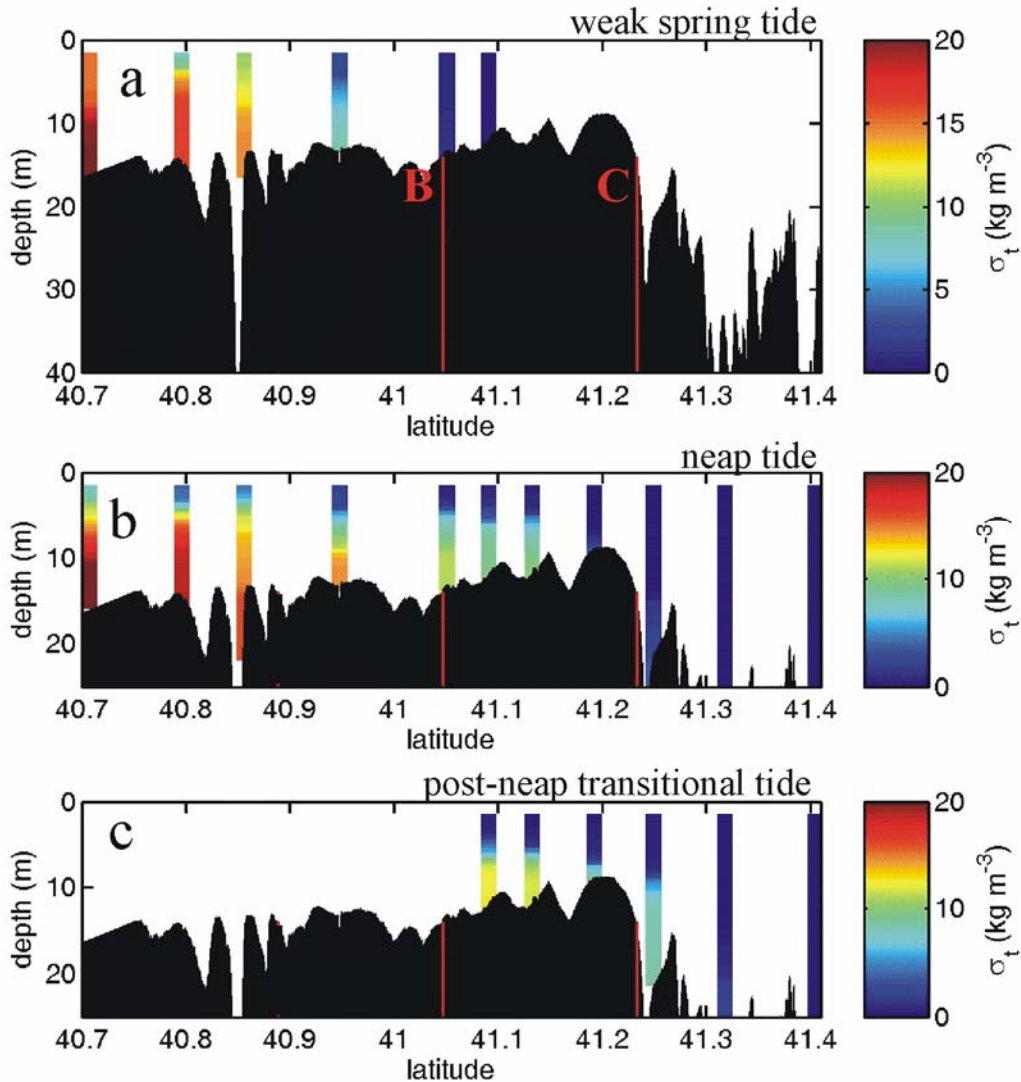


Figure 5: Three along-channel density transects during spring freshet season, for (a) a weak spring tide (2004 year-day 111, riverflow $Q=470 \text{ m}^3 \text{ s}^{-1}$), (b) one day prior to neap tide (2004 year-day 117, $Q=740 \text{ m}^3 \text{ s}^{-1}$), and three days after neap tide (2005 year-day 108, $Q=400 \text{ m}^3 \text{ s}^{-1}$). Vertical red lines show the ADCP sites, and the thalweg depth is shaded black. The aspect ratio exaggerates bed topography, and actual bed slopes are rarely greater than one percent south of 41.2° N latitude. The salt intrusion length maximum typically lags behind the minimum in tidal forcing, with maximum intrusion length occurring during the post-neap transitional period (see [Sec. 5.3](#)).

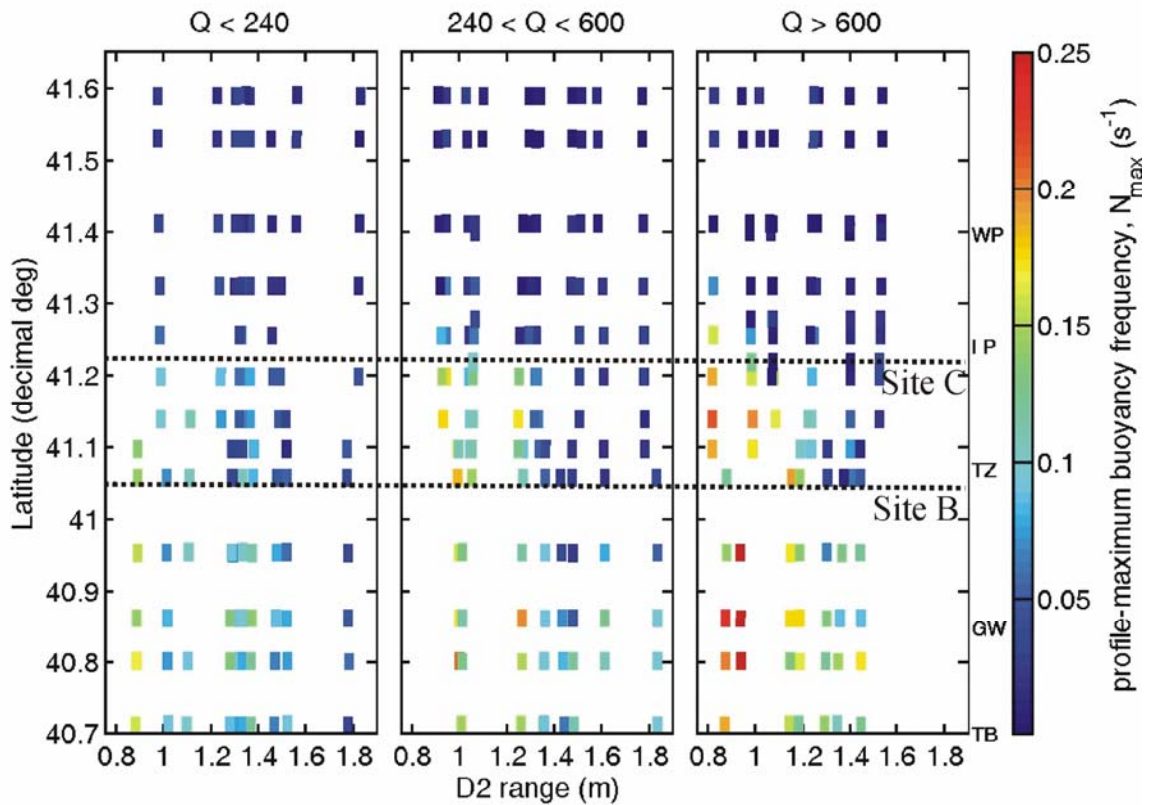


Figure 6: Summary of stratification (local N) observations in the Hudson, with respect to along-channel location (latitude), riverflow (Q ; prior 10-day mean) and semi-diurnal (D2; prior 5-day mean) tidal range. The plots summarize data from 30 along-channel transects like those in **Figure 5**, between 2001 and 2006. Horizontal dotted lines show Sites B and C. Each colored box shows the observed maximum water column stratification from a single profile (from 1.5 m vertical running averages of density). Symbols are (WP) West Point, (IP) Indian Point, (TZ) Tappan Zee Bridge, (GW) George Washington Bridge, and (TB) The Battery.

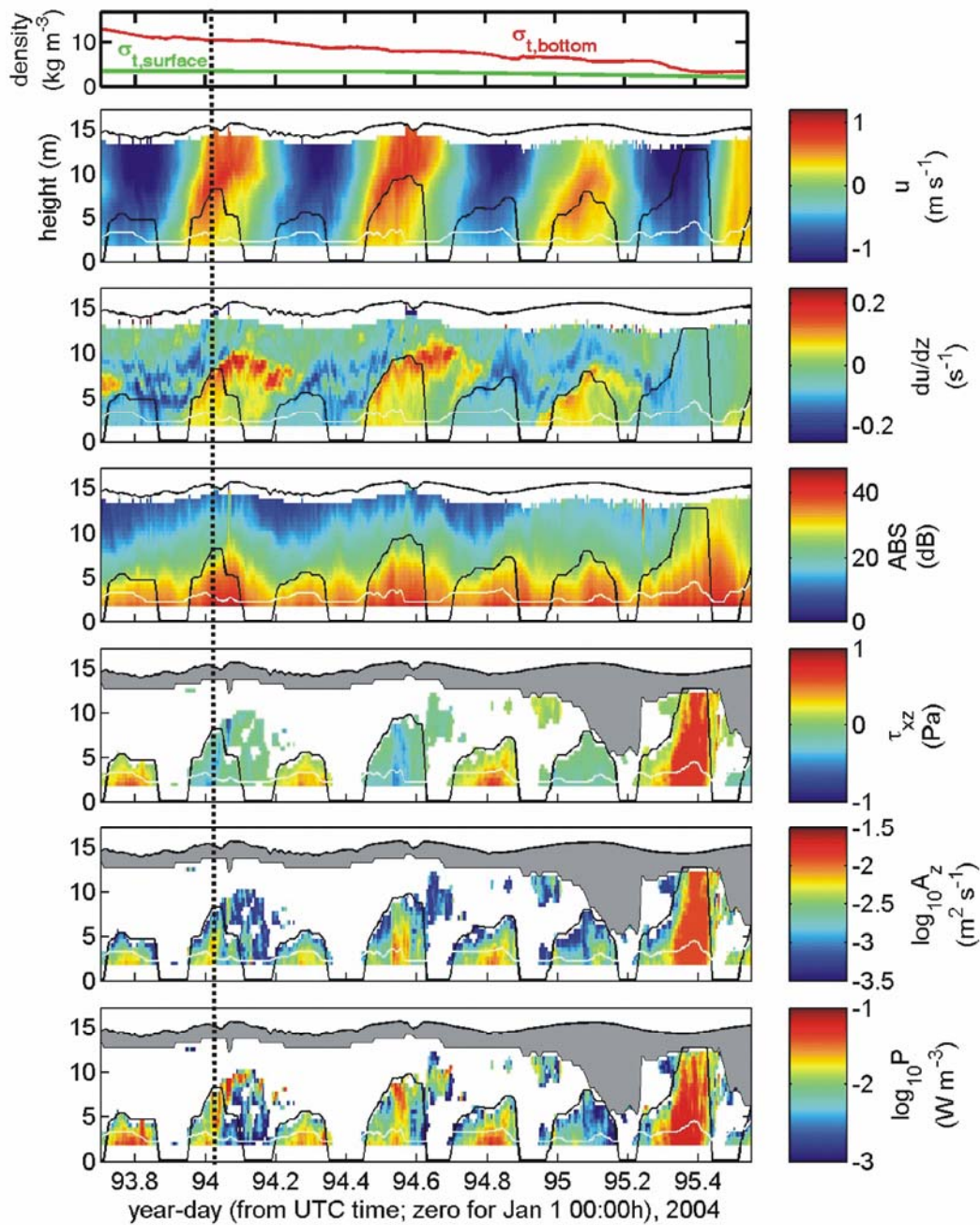


Figure 7a: (a) Site B and (b) Site C zoom-ins of a neap-spring transition with high riverflow. Plotted variables are: density (σ_t), along-stream velocity (u), along-stream vertical shear ($\partial u/\partial z$), acoustic backscatter (ABS), turbulent stress (τ_{xz}), eddy viscosity (A_z), and turbulent kinetic energy production (P). Turbulence data is masked when it is likely dominated by noise (blanked white) or side lobe and wave contamination (grey; see **Sec. 2.2**). The sea surface and bottom boundary layer height (black lines), and log layer height (white line) are shown. The vertical dotted lines show the times for the two figures that follow. Site C exhibits no log layer within our measurement range for most of this period.

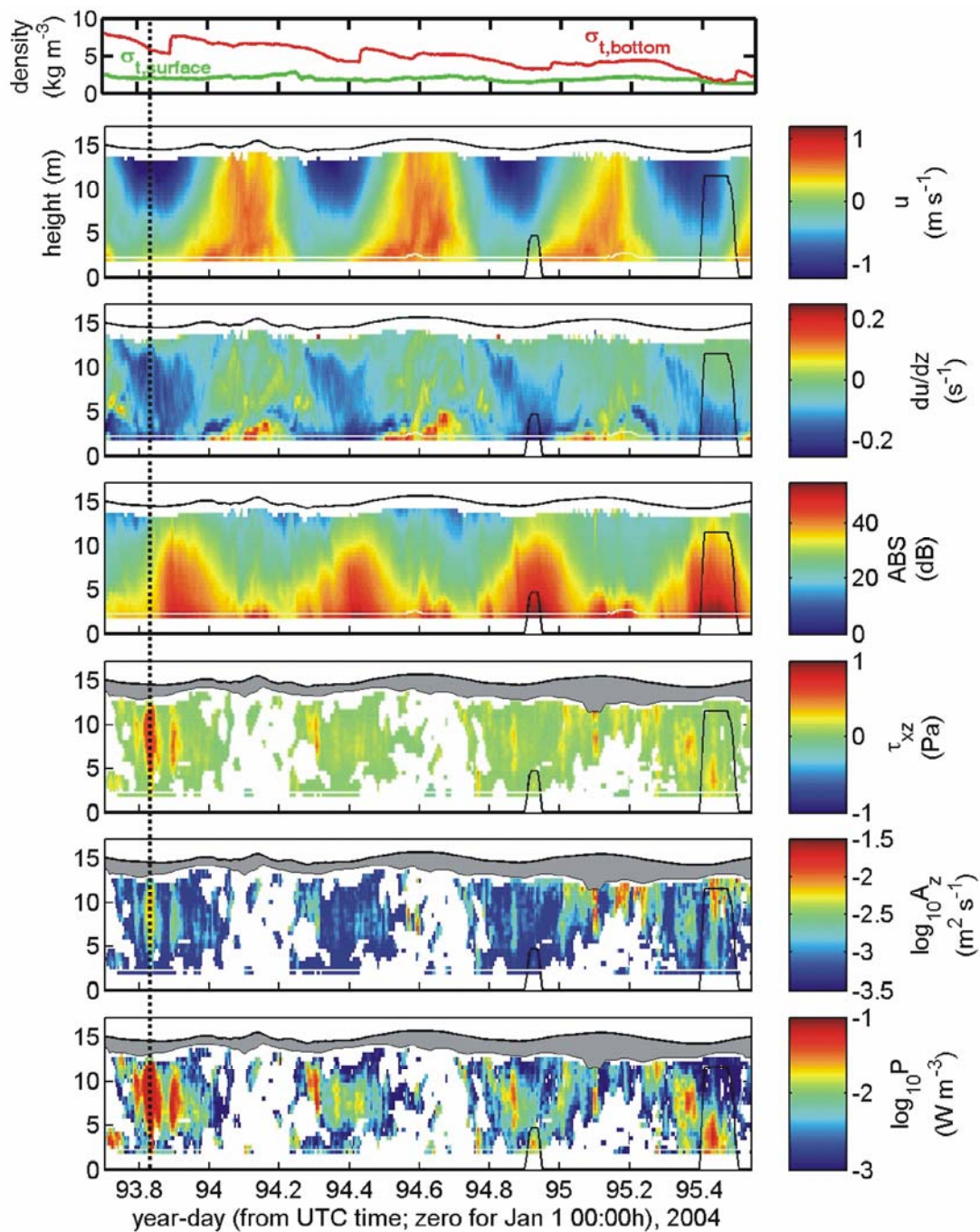


Figure 7b

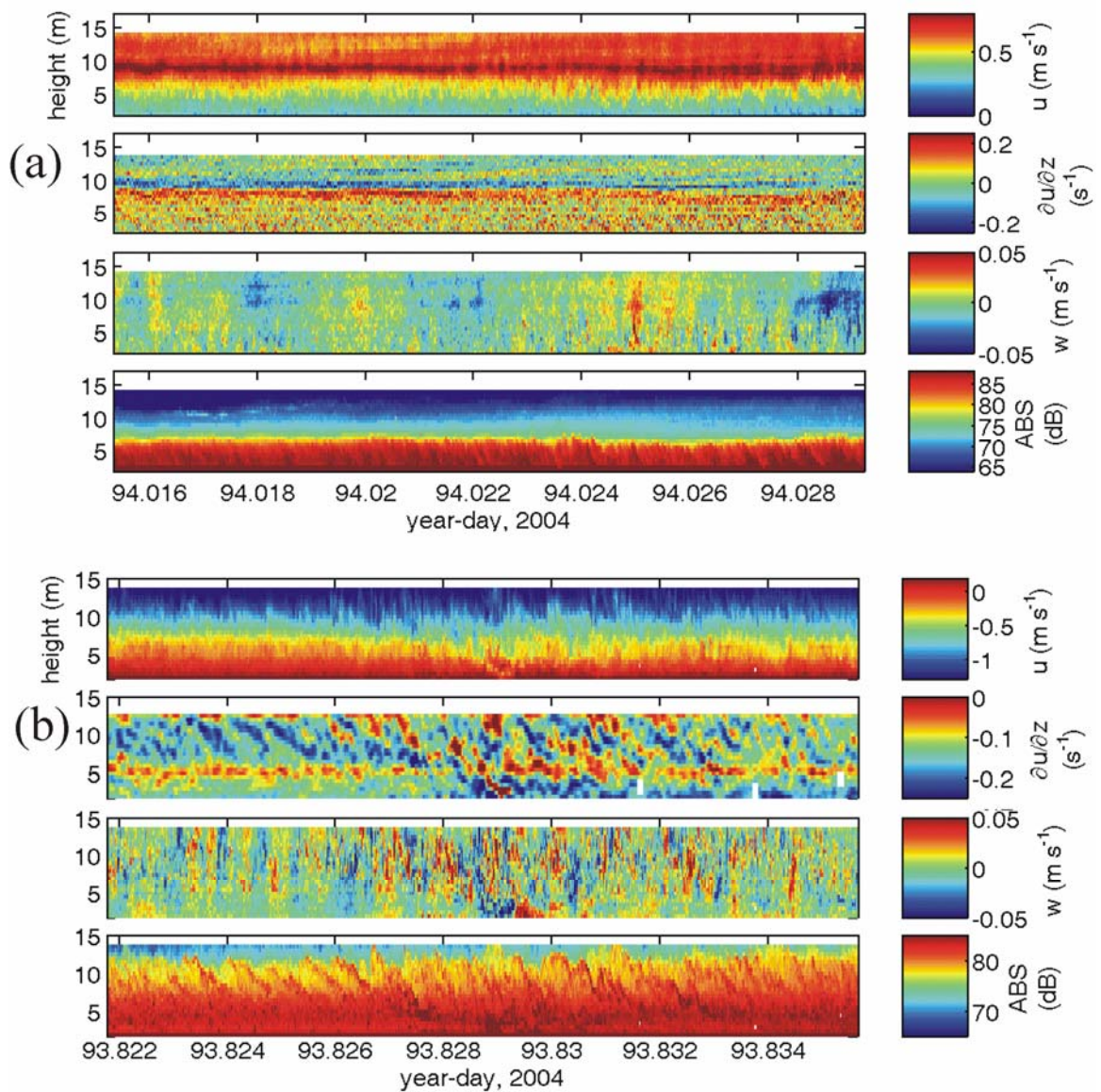


Figure 8: Zoom-ins to 0.5 Hz raw data for 20-minute periods at (a) Site B, and (b) Site C. Shown are: along-stream velocity (u), vertical shear ($\partial u/\partial z$), vertical velocity (w), and acoustic backscatter from a single ADCP beam (ABS). For Site C, shear is box-filtered with a 1.5 m by 10 s window, due to excessive variability. The following plot shows averaged turbulent stress profiles from these periods.

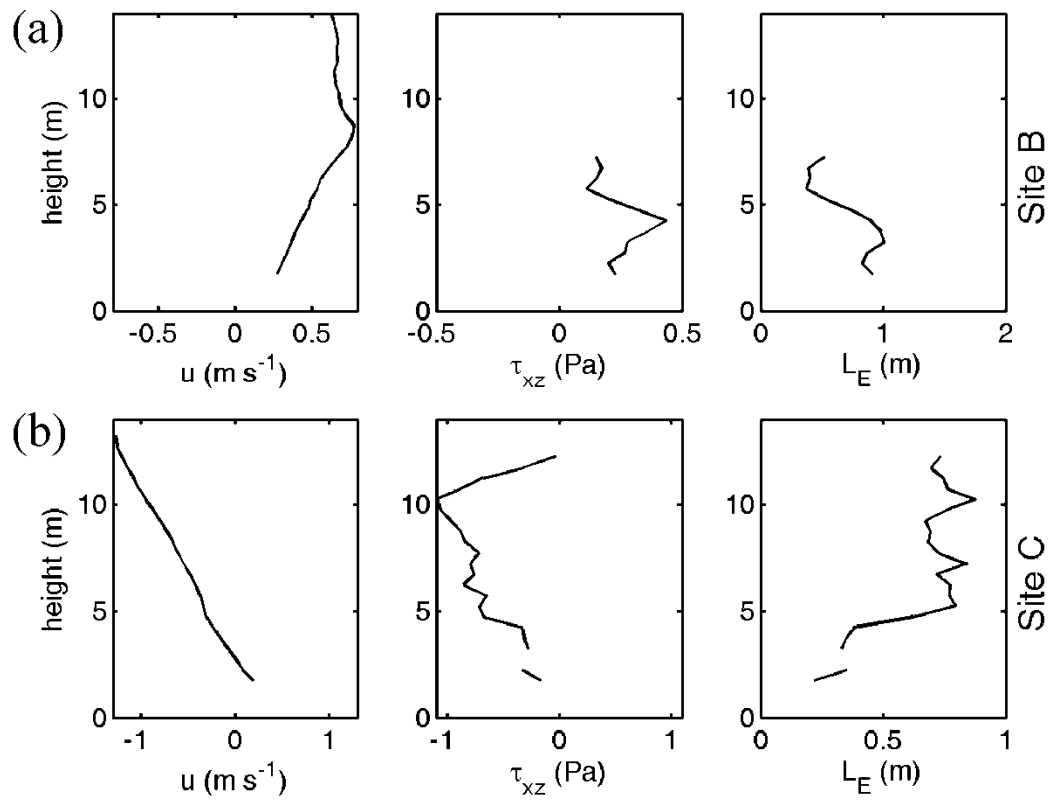


Figure 9: (a) Site B and (b) Site C, 20-minute averages of data from the periods shown in the prior figure. From left-to-right are along-stream velocity, turbulent stress, and the characteristic (Ellison) turbulent length scale ($L_E \approx 3\sqrt{\tau_{xz}/\rho S^2}$) [Stacey *et al.*, 1999a].

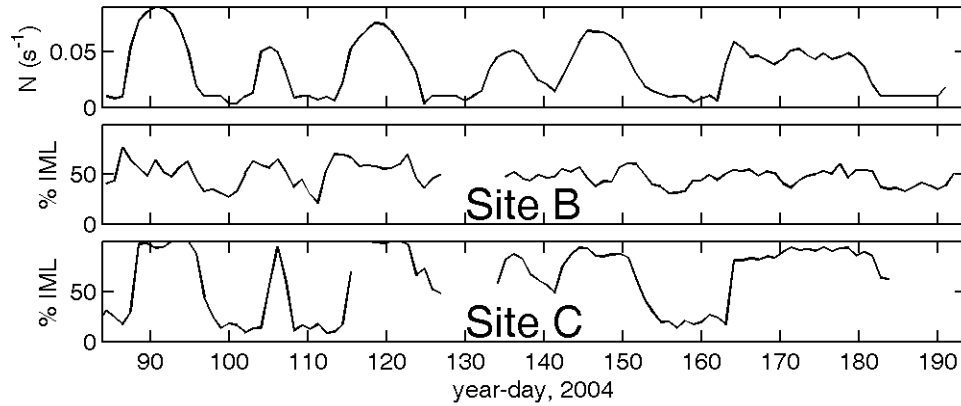


Figure 10: Comparison of stratification (bulk buoyancy frequency, N , for Site B) with the percentage of total turbulence (integrated production) that occurs in the IML (% IML). IML turbulence takes on a relatively larger role during periods of strong stratification.

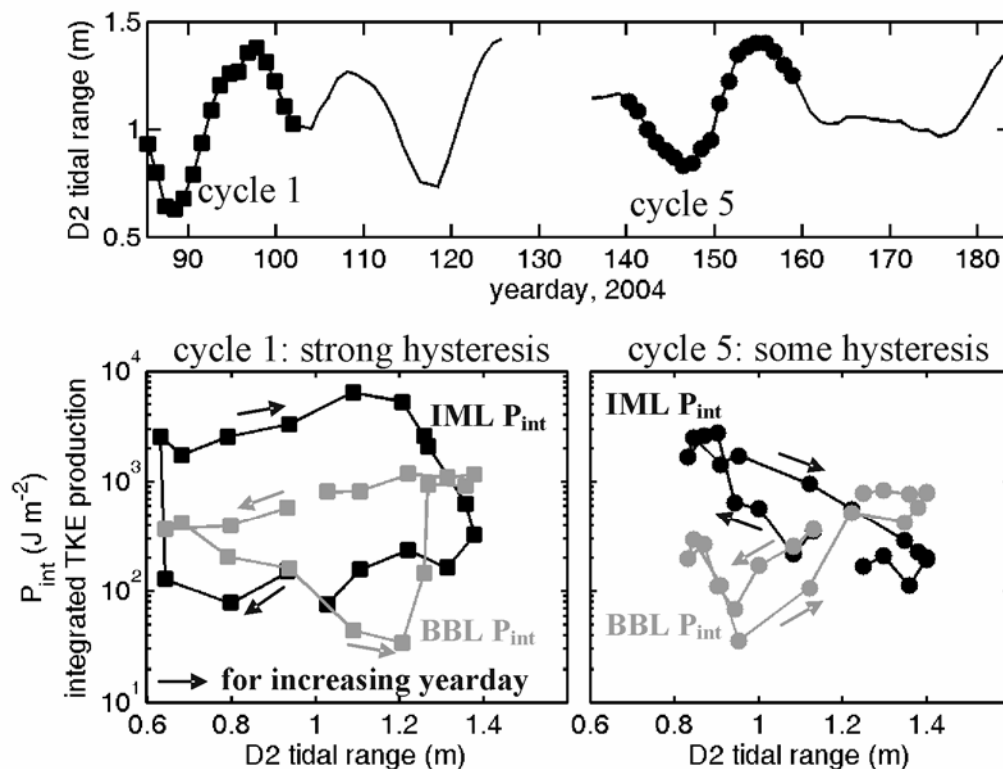


Figure 11: At Site C, post-neap transitional tides can have ~ 15 times higher (lower) IML (BBL) turbulence and mixing than post-spring transitional tides, a hysteresis pattern. The top panel shows the time series of semidiurnal (D2) tidal range, and the two periods shown in the bottom panels are marked with squares and circles for each tidal day, respectively. The lower panels show P_{int} for the bottom boundary layer (BBL) and internal mixing layer (IML). Since the buoyancy flux is roughly proportional to IML P_{int} [Rippeth, 2005], this hysteresis should also exist for the vertical mixing of dissolved constituents.

Chapter 3

AN AUTONOMOUS SELF-ORIENTING CATAMARAN

(SOCA) FOR MEASURING AIR-WATER

EXCHANGES AND FORCING

Abstract

An instrumented, Self-Orienting Catamaran (SOCa) has been developed to measure air-water mass, heat and momentum exchange, as well as physical properties just above and below the air-water interface. The autonomous capabilities of SOCa include an atmospheric CO₂ profiling and air-water flux (F_{CO_2}) measurement system, surface-following measurements of water velocity and turbulent energy dissipation, and rotational orientation of water sensors into a surface current to avoid flow distortion. The gradient flux technique (GFT) is used with simplified assumptions of atmospheric eddy diffusivity to estimate F_{CO_2} . Using field data from the Hudson River estuary, SOCa is shown to orient properly to direct water measurements into the current for different combinations of wind and water velocity, up to mean wind speeds of at least 10 m s^{-1} . Water velocity and turbulence data are validated with instrument comparisons and a turbulent energy budget. Uncertainty and biases in F_{CO_2} estimates are quantified using null tests. A technique is presented for determining the applicability of GFT for a given study site, including consideration of wind fetch, flux footprint, and the air-water CO₂ partial pressure difference. This paper describes procedures for building a similar platform, and data processing methods that will be useful for a variety of autonomous platforms designed to study air-water interaction.

1. Introduction

Air-water interaction processes driving mass, heat, momentum transfer are being studied and modeled at increasing levels of detail because of their important influence on ocean circulation and climate. Due to the small scales involved in processes such as wave

breaking or Langmuir circulation, these processes are typically parameterized in numerical ocean and climate models, and several recent field campaigns have sought to improve these parameterizations [e.g., *Edson et al.*, 2007; *McGillis et al.*, 2001c; *McGillis et al.*, 2004; *Salter et al.*, 2008]. An important aspect of these studies is the application of autonomous platforms and tools for measuring air-water gradients and fluxes, which can greatly extend the duration and range of conditions sampled [e.g., *DeGrandpre et al.*, 1995; *Edson et al.*, 2000; *Graber et al.*, 2000].

Air-water gas exchange in rivers, estuaries and the continental shelf is also of growing interest due to the potentially important role of these regions in the global carbon budgets [*Birdsey et al.*, 2009; *Borges*, 2005], and growing concerns over hypoxia [e.g., *Dai et al.*, 2006]. Studies at the ocean's margins are particularly useful for improving our understanding of air-water interaction, due to their convenient access, and diverse characteristics (e.g. fetch, depth) and processes (e.g. winds, tides). Also, large air-water CO₂ partial pressure differences [$\Delta p\text{CO}_2$; *Borges*, 2005] lead to larger air-water gas fluxes that are easier to measure.

The design of a dual-purpose instrument platform that measures both air-water exchanges and turbulence just below the air-water interface is motivated by recent studies that have demonstrated fundamental links and feedbacks between these processes [e.g., *McGillis et al.*, 2004; *Moog and Jirka*, 1999; *Nimmo-Smith et al.*, 1999; *Zappa et al.*, 2007]. Air-water gas exchange is fundamentally an interfacial turbulent process in all but the most quiescent conditions, whether forced by tidal currents, wind, rain [*Zappa et al.*, 2007] or diurnally-forced convection and shear instability in the surface ocean [*McGillis et al.*, 2004]. A catamaran that is attached to a boom alongside a boat has recently been used

for field studies of estuarine air-water gas exchange and turbulence, but requires carefully timed manual profiling to collect vertical profiles of wind, temperature, humidity and CO₂ [Zappa *et al.*, 2007; Zappa *et al.*, 2003]. The observations collected from that platform have been highly valuable, and a goal of the present research is to collect data over a much wider range of conditions and locations using an autonomous platform and atmospheric profiling system.

This paper describes the construction and capabilities of the Self-Orienting Catamaran (SOCa) and its automated CO₂ profiling and air-water flux measurement system. SOCa is a versatile, shallow-draft instrument platform that is deployed at anchor and has properties assuring that its water velocity measurements and atmospheric profile measurements are made without structural flow interference. The gradient flux technique (GFT) is utilized to estimate air-water gas fluxes with a small spatial footprint, useful for studying small-scale aquatic systems or localized features in the coastal ocean. In the sections that follow, we: (a) describe SOCa construction, instrumentation, and measurement techniques; (b) assess SOCa behavior, instrument performance, and uncertainty using data from two field campaigns on the Hudson River estuary; (c) present methods for evaluating the applicability at a given site for GFT gas exchange measurements; and (d) discuss how SOCa can help broaden our understanding of air-water interaction processes.

2. Materials and Procedures

The primary desired attributes for designing SOCa were autonomy, mobility, and low labor and materials expenses. These were achieved by constructing a simple lightweight

catamaran that can be transported and deployed on short notice at a wide range of possible locations. The catamaran has a low deck for minimal windage and a keel that "vaned" or steers it into the current so that near-surface currents are measured without obstruction (**Figures 1 and 2**). A 15 m long bridle is fed through the front crossbar (**Figure 1**) to avoid anchor-line flow interference in front of the water velocity sensors. The catamaran's pontoons are lightweight, have a draft of only ~0.15 m, and allow waves to pass under the vessel unimpeded.

Atmospheric measurements are also collected in such a way as to minimize problems with structural flow interference. "High height" atmospheric wind velocity measurements and pumped air samples are taken at the top of a 2.25 m mast, located high enough that platform flow interference is negligible. "Low height" atmospheric air intakes are located on both sides of SOCa so that there is always a sample taken on the upwind side, undisturbed by structural flow interference (**Figure 1**). Optimally, a second wind measurement is made either on the windward side (e.g. **Figure 2b**) or at a height high enough to avoid structural flow interference.

2.1 SOCa construction and data logging

The materials and labor costs of the platform itself are relatively low, due in part to using commercially available components – below \$1000 and one day of assembly. Materials are shown in **Figure 1**, with the most critical being the pontoons (Hobie Floatcat 75), 119 cm long by 3.2 cm outer diameter pipe crossbars, a 0.01 m thick plastic deck with holes for water drainage (and easy hose-clamp or zip tie attachment for additional components), and a sheet of 89 x 52 x 1.9 cm plywood for a removable keel, held firmly in

place with a vice. Slide-on instrument posts were developed for the current meters and other water-side instruments to be mounted on the 3.8 x 3.8 x 150 cm aluminum rectangular tube boom at the front of the vessel – these can be fixed in an upright position while motoring in the near-shore, then manually removed, flipped, and clamped in a downward orientation when ready to sample. The reasoning here is that the instruments in deployment position are highly vulnerable, so flipping them makes setup and transport simpler and safer.

Power and data logging are achieved using one or two onboard 12-volt 100 amp-hour deep cycle batteries in (standard) vented water-resistant marine battery boxes, waterproof boxes, and a small computer and USB-to-serial box (8 serial ports). In-house software was used to log each serial data port separately to a file with hourly time stamps. Power draw with all systems running is ~5 amps, so batteries must be changed every 1-2 days with this setup (see the Discussion section for approaches to extending this duration). Battery changes have been made on the water with a visit with a small outboard inflatable boat.

2.2 Sensors and locations

SOCa is fitted with physical and chemical sensors for observing air-water gas fluxes and processes that directly influence these fluxes – wind velocity, water velocity and turbulence, water temperature, salinity and stratification, CO₂ concentrations in surface water and at two heights in the lower atmospheric surface boundary layer, and H₂O concentrations in the atmosphere. Water velocity is recorded at 25 Hz with an acoustic Doppler velocimeter (10 MHz Sontek ADV) with beams oriented downward to sample at a depth just below the sea surface (0.1-0.5 m), with the sensor head 0.2 m forward of the

vessel's pontoons. The turbulent kinetic energy dissipation rate is estimated using the inertial dissipation method (described below). An inertial sensor (Crossbow VG400MA-100) samples at 25 Hz to monitor vessel motion to assist in the turbulence data processing. One or two 2-D sonic anemometers (Gill Wind Observer II) continuously record wind velocity and air temperature above the platform (**Figure 2**). A chain of temperature or temperature-conductivity sensors is attached to the anchor line to measure density stratification. Instruments and their locations used in one particular field study are given in **Table 1**.

The automated atmosphere and water CO₂ profiling system is described here, and the Gradient Flux Technique (GFT) is utilized to estimate air-water fluxes (see sections below). Two closed path infrared CO₂/H₂O concentration sensors (Licor, LI-840) in the CO₂ box (**Figure 1**) are used for measuring (sensor 1) air samples from a gas valve switchbox, and (sensor 2) a stationary atmospheric timeseries from one height. The switchbox was built in collaboration with Fathom Research, Inc., and combines an electronically switched 4-port valve actuator (VICI Valco, model ECMT) with a computer controller, and reports its position via serial communication. The switchbox is used so that atmospheric and air-water gradients are measured using the same LI-840 sensor, avoiding problems with instrument inter-calibration. The stationary timeseries is collected so that the temporal change that occurs while a vertical profile is sampled can be removed before computing the vertical CO₂ gradient [McGillis *et al.*, 2001c]. Miniature pumps pull air through each sensor. Air for the first LI-840 (**Figure 1**; S1) is routed through the switchbox in 10-minute increments from four channels: (S1) the headspace of an equilibrator that processes surface water pumped from below the front of the vessel, with pump intake at 20

cm depth (7 L min^{-1}), (S2) 0.4 m height atmosphere at the back of the vessel, (S3) 2.25 m height atmosphere, (S4) 0.4 m height atmosphere at the front of the vessel. All air sample nozzles have filters to prevent water droplets or other particles from being pulled into the switchbox and LI-840s. Gradients in CO_2 or H_2O are computed using two-point "profiles" taken between channels 2 and 3 (wind from aft) or 3 and 4 (wind from fore). The watertight box holding the two LI-840s was shielded from solar heating with an additional white fiberglass panel with 2 cm of spacing.

The equilibrator is a smaller version of the design used to measure seawater pCO_2 by Broecker and Takahashi [1966], with a water volume of 0.8 L and air volume of 2.0 L, fashioned from off-the-shelf parts [Newberger, 2004]. Water is drawn with an immersion pump from a water depth of 20 cm and sprayed into the equilibrator. The water in the base of the equilibrator is steady at the level of a pipe outlet at 15 cm height, through which it drains out of the bottom. Air is drawn from the headspace through the LI-840 at a rate of 1.0 L min^{-1} , then routed back into the equilibrator to form a closed loop (**Figure 1**; SO), allowing equilibration of $[\text{CO}_2]$ in the water and headspace air to occur gradually. The equilibrator was insulated from heat loss or gain with 1.9 cm thick low-density foam rubber and from solar radiation with a thin flexible white plastic panel wrapped around.

2.3 The Inertial Dissipation Method (IDM)

IDM is based on Kolmogorov's turbulent cascade theory and has been used for decades to estimate the rate of dissipation of turbulent kinetic energy (ϵ) in a fluid flow [e.g., Voulgaris and Trowbridge, 1998; Zappa *et al.*, 2003]. This well-validated theory

holds that the spatial power spectral density (Φ) of velocity over the "inertial subrange" of eddy sizes is a simple function of ε and eddy size:

$$\Phi_i = \alpha_i \varepsilon^{2/3} \kappa_i^{-5/3} \quad (1)$$

Here, index i refers to either the along-stream ($i=1$), across-stream (2) or vertical velocity (3). Eddy size is represented by its inverse, the angular wavenumber, κ_i . Eq. 1 provides a means of computing ε , once the relationship between Φ_i and κ is found with spectral analysis. The constant α_i is 0.51 if the along-stream velocity is used to compute Φ_i , whereas it is 0.68 if the across-stream or vertical velocity is used [Jonas *et al.*, 2003]. The spatial spectrum Φ_i is required above, yet if timeseries data is used (e.g. with the ADV), only the temporal spectrum is known. In that case, Taylor's frozen turbulence hypothesis, which holds that the turbulent eddies are passively transported in a mean current, allows one to simply use the along-stream velocity to convert from a temporal to spatial spectrum and from frequency to wavenumber. However, this hypothesis has been shown to be invalidated when the wave orbital velocity is larger than the mean flow velocity [Lumley and Terray, 1983].

2.4 ADV data processing

Collecting ADV data and estimating ε from an autonomous surface-following platform requires special processing techniques for dealing with measurement noise, wave orbital velocities and velocities due to vessel motion. Dissipation 10-minute averages were computed by modeling the velocity spectrum over the inertial subrange with a least-squares best-fit linear combination of two basis functions (**Figure 3**), an approach we refer to as the

Kolmogorov + Noise (K+N) approach: (1) a constant, for the noise floor, and (2) the model in Eq. 1. This effectively subtracts off a white noise floor from the spectrum while computing ε . The confidence interval on the scaling of the second basis function allows computation of a confidence interval on the ε . Spectral analysis for the ADV involved the instrument's axial velocity, Φ_3 (parallel to the ADV probe orientation), to minimize effects of instrument noise, which is a factor of thirty lower on this axis [Voulgaris and Trowbridge, 1998]. The WOSA technique was used for spectral analysis – Weighted (or Welch's) Overlapping Segmented Averages – and applied to 2.5-second segments (ADV), producing 10-minute averages. Maximum wavenumbers for computing ε correspond to the smallest water motions that can be measured by a given sensor without substantial bias due to spatial or temporal averaging. Using a high-wavenumber cutoff of $2\pi/3\Lambda$ with the ADV vertical spatial averaging lengthscale of $\Lambda = 0.009$ m [YSI-Sontek, 2009], the maximum wavenumber observed in the inertial subrange is then 240 rad m^{-1} . Minimum wavenumbers also must be chosen to be above the wave mode to avoid bias in the ε estimate, and the inertial sensor mounted onboard SOCa is useful for determining this wavenumber and for monitoring all types of vessel motion.

Four quality control masks were developed with the goal of omitting periods that were not consistent with the K+N model, and their effects were tested by examining individual 10-minute timeseries and spectra: (1) a "quality-of-fit mask" when the rms:mean ratio for the least-squares fit of Φ_3 was above 0.15; (2) an "high uncertainty mask", when the 95% confidence on the ε estimate is greater than 50% of the ε estimate (typically periods dominated by sensor noise); (3) a "wave orbital mask" when the 10-minute velocity standard deviation was above half the mean velocity; and (4) on raw 25 Hz data, a "flow

interference mask" is applied when the timescale over which water is swept out of the sample volume by horizontal flow is not much smaller (less than half) than the timescale over which the vertical flow leads to a sensor wake in the sample volume. This last mask is useful for autonomous deployments and has the goal of omitting raw data from aperiodic events like boat wakes, common in inland waterways (especially on weekends).

2.5 Autonomous application of the Gradient Flux Technique (GFT)

Of the choices for automated air-water flux measurement techniques on SOCa, the most direct measurement is eddy covariance [McGillis *et al.*, 2001a]. However, when collected from a moving vessel, challenging motion corrections are required, and these may not be successful in wavy conditions onboard a small platform. A simpler and more robust method for estimating air-water exchanges from a free-floating platform is GFT, which has the advantage of requiring only measurements of mean vertical gradients, often much easier to measure than the eddy covariance. Flux estimates computed with GFT compare favorably with other, more direct flux measurements [Businger *et al.*, 1971; McGillis *et al.*, 2001c; Zappa *et al.*, 2003].

GFT utilizes the fact that a constituent's air-water exchange is proportional to its vertical gradient in the atmospheric surface layer (ASL), and corrects for the smearing of the gradient by turbulent mixing. A shortcoming of the method is its reliance on a parameterization to represent this mixing, but theory for ASL mixing is well-developed and has been validated extensively [e.g., Edson *et al.*, 2004; Edson *et al.*, 2007]. Additional shortcomings include an assumption that the atmospheric flow and fluxes are horizontally uniform, and a reliance on very small vertical gradients that may be similar to the

instrument resolution. The impacts of these shortcomings are addressed below, through consideration of the flux footprint (Eq. 6) and through an analysis of the minimum profile height required for GFT (Eq. 7) in the Assessment section.

The ASL turbulence parameterization used with GFT is Monin-Obukhov similarity theory [MOST; *Monin and Obukhov*, 1954], which states that various turbulence statistics are all universal functions of non-dimensional height $\zeta = z/L$, where:

$$L = -\frac{T_V}{0.41g} \frac{U_*^3}{F_{T_V}} \quad (2)$$

Here, z is the height above the sea surface, T_V is virtual temperature, g is gravity, U_* is the shear velocity (a scale for the turbulent wind velocity), F_{T_V} is the upward air-water buoyancy flux, and L is the Obukhov length, such that heights above $|L|$ have buoyancy (e.g., heat) forcing that is stronger than mechanical forcing (shear). For a sensor at height z , if the non-dimensional sensor height $\zeta = z/L$ is below -1, convection dominates, if it is above +1, stratification dominates, or if it has a magnitude close to zero, shear-generated turbulence dominates.

The water-to-air flux of CO_2 (F_{CO_2}) is defined with GFT as [*Edson et al.*, 2004; *McGillis et al.*, 2001b; *McGillis et al.*, 2004]:

$$F_{\text{CO}_2} = -K_C(z) \frac{\partial C(z)}{\partial z} = -\frac{0.41 U_* z}{\Phi(\zeta)} \frac{\partial C(z)}{\partial z} \quad (3)$$

Here, K_C is the eddy diffusivity for CO_2 , $C(z)$ is the CO_2 number density (moles per m^3 dry air) at height z , and $\Phi(\zeta)$ is an empirical stability function that accounts for atmospheric stability effects on scalar (e.g. heat, CO_2) turbulent diffusion. For neutral stability (no buoyancy effects), Φ equals one, for convective cases it is below one, and for stratified

cases it is above one. Taking the definite integral with respect to z between the two C measurement heights, the flux is:

$$F_{CO_2} = -0.41U_* \frac{\Delta C(z)}{\Delta[\ln z - \Psi(\zeta)]} \quad (4)$$

Here, the numerator $\Delta C(z)=C(z_2)-C(z_1)$ is the measured two-point vertical difference in C , the denominator is the stability-corrected vertical height difference, and $\Psi(\zeta)$ is the integrated form of the empirical stability function $\Phi(\zeta)$. If C data at more than two heights are collected, the slope of a regression of C versus $[\ln z - \Psi(\zeta)]$ is used in place of the two-point gradient estimate [e.g., *McGillis et al.*, 2004]. It is also important to eliminate temporal changes ($\partial C/\partial t$) – occurring over the time it takes to sample the different heights in a profile – from the measured vertical profile of C . Temporal change is removed by subtracting the stationary timeseries of C from 2.25 m off both $C(z_1)$ and $C(z_2)$ before computing ΔC , similar to the approach of *McGillis et al.* [2001c] but with the additional simplification that L is taken to be constant over the period it takes to sample the profile.

On SOCa, single-height measurements of wind velocity, temperature and humidity, and measurements of water velocity and temperature are used with the COARE 3.0 bulk flux toolbox in Matlab (*Fairall et al.* 2003) to estimate momentum and heat fluxes, U_* , L , $\Psi(\zeta)$ and the equivalent neutral wind speed at 10 m height (U_{10N}), for every 40-minute switchbox cycle. The COARE 3.0 bulk flux algorithms also use MOST, they have been extensively validated, and they are accurate to within 5% for wind speeds up to 10 m s^{-1} over the open ocean [*Fairall et al.*, 2003]. They were also recently demonstrated to give accurate momentum flux estimates for the coastal ocean for winds from $4\text{-}12 \text{ m s}^{-1}$, but had reduced accuracy during periods with a highly stratified lower atmosphere that occur when

the ocean is cold, atmosphere warm, and winds weak [Edson *et al.*, 2007]. An alternative to using COARE is to collect two-point (or more) profiles of velocity, temperature and humidity and use GFT to estimate momentum and heat fluxes and U_* through an iterative approach [e.g., Launiainen and Vihma, 1990], which would improve accuracy of the flux estimates but would still rely on the MOST mixing parameterization. Approaches for making automated profile measurements of these variables are presented in the Discussion section.

2.6 CO₂ data processing

CO₂ molar ratio measurements [CO₂] are used to compute 10-minute mean number density (C) values. First, spikes beyond two standard deviations from a running mean are omitted from the raw molar ratio data, and generally match well with notes in the log book that a boat is motoring by, upwind. Average [CO₂] and [H₂O] are then computed over 10-minute periods, following the switchbox schedule. Average [CO₂] data are corrected for dilution by water vapor, and then these data are converted to the number density using the ideal gas law with observed atmospheric pressure.

Computation of the average $\Delta p\text{CO}_2$ is performed for every 40-minute switchbox cycle by computing partial pressure from observed molar ratio concentration and atmospheric pressure [McGillis and Wanninkhof, 2006], assuming ideal gas behavior and estimating saturation water vapor pressure from water temperature and air pressure [Gill, 1982]. The CO₂ solubility K_0 is computed as a function primarily of water temperature, but also secondarily of salinity [McGillis and Wanninkhof, 2006; Wanninkhof, 1992; Weiss, 1974], both measured in situ.

The air-water CO₂ flux is computed using Eq. 4 and related to the gas transfer velocity (k) through the empirical parameterization $F_{\text{CO}_2} = k \Delta C_{\text{aq}}$, where ΔC_{aq} is the CO₂ concentration gradient across the mass aqueous boundary layer [Liss, 1983]. ΔC_{aq} is difficult to measure in the field, so the fugacity or partial pressure difference between surface water and air just above the sea-surface is typically employed instead [McGillis and Wanninkhof, 2006]:

$$k = F_{\text{CO}_2} / K_0(p\text{CO}_{2,\text{water}} - p\text{CO}_{2,\text{air}}) = F_{\text{CO}_2} / K_0\Delta p\text{CO}_2 \quad (5)$$

Here, the solubility K_0 is assumed to be constant across the aqueous mass boundary layer, and $p\text{CO}_{2,\text{water}}$ and $p\text{CO}_{2,\text{air}}$ are the partial pressures of CO₂ in water and air. Calculations of F_{CO_2} , K_0 and $\Delta p\text{CO}_2$ are used compute k . The Schmidt number is the ratio of momentum to mass diffusivity, and depends on the gas of interest as well as the temperature and salinity of the water. The gas exchange velocity k is normalized to a Schmidt number for CO₂ (Sc) of 660 (the value for a temperature of 20 °C and salinity of 35 psu) using observed salinity and temperature timeseries [Wanninkhof, 1992], and hereafter referred to as k_{660} .

2.7 The flux footprint

Several studies have evaluated the spatial area of interfacial flux represented by a concentration or flux measurement at a given height – the measurement footprint [reviewed in Vesala *et al.*, 2008]. These studies were for relatively rough surfaces, forests or cropland, but we are aware of no study of the footprint over relatively smooth surfaces like water. One simple analytically-derived footprint equation that has received wide use was developed by Gash [1986]:

$$\lambda_p = \frac{-z[\ln(z/z_0) - 1 + z_0/z]}{0.41^2 \ln(p/100)} \quad (6)$$

Here, λ_p is the footprint in the direction of the wind, p is the percent of the flux coming from within this distance, and z is the measurement height. GFT relies on multiple vertically-spaced measurements, each with its own footprint, so the footprint is a more complex function of the heights utilized. If there is a spatial change in the air-water exchange over the footprint of the high height concentration measurement, then the horizontal uniformity assumption is violated and the flux estimate may be inaccurate. Thus, it is important to consider the spatial variability expected for a given study site before choosing measurement heights.

3. Assessment

SOCa measurements of water velocity, turbulence, and gas exchange are assessed below using field data. In situ system tests and comparisons between different instruments are used to validate the measurements and quantify uncertainty. Additional validation is sought using comparisons of field observations with those from prior studies. Lastly, techniques are presented for determining whether GFT is applicable, based on $\Delta p\text{CO}_2$, wind fetch, sensor uncertainty, and other parameters.

3.1 Field evaluation

A study called Carbon and Air-Sea Interaction in an Estuary (CASsIE) was conducted in fall, 2007. fSOCa was frequently anchored at a shallow (5 m) site in the Hudson River estuary, during the period 23 September through 2 November, 2007 (year-

days 265-303), with instrumentation summarized in **Table 1**. The platform was anchored at this site collecting extensive datasets for periods as long as 11 days (year-day 269.5-280.5). A total of 19 complete days of wind and ADV data, and 14 days of CO₂ data were collected. The study site had a cross-channel wind fetch of 1.8 km in each direction and along-channel fetch of >10 km (it is a long straight estuary), resulting in significant wave heights estimated at 0-0.5 m. Nearby, a bottom-mounted acoustic Doppler current profiler measured vertical profiles of velocity and acoustic backscatter at 1 Hz, with a Seabird SBE-37 CTD on its frame. Also, a meteorological station on a pier 8 km to the south included measurements of atmospheric pressure. Observations during CASSIE are summarized in **Figure 4**.

3.2 Platform orientation

SOCa oriented properly to direct the ADV into the surface current for different combinations of wind and water flow direction, up to mean wind speeds of at least 10 m s⁻¹ (**Figure 5**). The current velocity angle relative to SOCa was small for low wind speeds, but its magnitude was sometimes larger for higher wind speeds. However, when water speed was at least 0.20 m s⁻¹, the water flowed into the ADV from an acceptable angle (+/- 60 deg) 99.8% of the time, avoiding current measurements biases due to wake effects (**Figure 6**). Pitching of the vessel moves the velocity sensor vertically, impacting vertical and potentially also stream-wise velocity measurements. Dissipation measurements are made possible, however, by the separation of wave-induced velocities from the inertial subrange in wavenumber space. Wave-induced variability in platform tilt was generally small but increased with wind speed (**Figure 7**).

In **Figure 6**, some points were characterized by relative current directions above 20 degrees and wind speeds above 8 m s^{-1} . These data were mostly from one period with strong north winds and weak (opposing) flood tide currents that peaked at 0.31 m s^{-1} , below normal due to the opposing wind (year-days 284.87-285.0). SOCa began rotating around the anchor point and into the current after slack tide, but the wind blowing across the side of the platform (during the rotation) appears to have provided enough force on the platform to stop SOCa from completely rotating into the current. The effect of wind drag on rotational orientation can be reduced by using lower-profile boxes on SOCa's deck, or a keel with more surface area below water and less above water.

3.3 Velocity and turbulence validation

When the ADV was collecting data during CASsIE, successful TKE dissipation (ϵ) estimates were available for 70% of 10-minute periods with currents above 0.4 m s^{-1} , or 50% of periods with currents above 0.2 m s^{-1} . Of all the data with 20 cm s^{-1} currents or higher, about 40% fail the wave orbital mask, 30% fail the quality-of-fit mask, 20% fail the flow interference mask, and 7% fail the high uncertainty mask. Of the cases with unmasked ϵ estimates, the mean observed 95% confidence interval is $\pm 25\%$.

The range in ADV ϵ estimates for CASsIE was from 5×10^{-8} to $8 \times 10^{-4} \text{ W kg}^{-1}$ (**Figure 4**), with detection of lower values generally prevented by the ADV noise floor. During low energy periods, ADV sampling noise led to white (flat) velocity spectra at high wavenumbers. The velocity range was maximized during this experiment, and this may generally be necessary with a moving platform in wavy conditions. In environments with small waves, it would likely be possible to observe lower ϵ values with a lower range

setting – instrument noise is proportional to the velocity range [Voulgaris and Trowbridge, 1998].

Validation for the ADV surface water speed measurements is provided by a comparison with ADCP data, with good agreement at all times (**Figure 8**). Validation for the ϵ estimates was accomplished on two fronts, though only for low-wind conditions (**Chapter 4**): (1) agreement typically within a factor of two in a comparison between the ADV and a fine-scale (2.6 cm resolution) spatial velocity profiler that does not require Taylor's assumption, and (2) closed spring tide turbulent kinetic energy (TKE) budgets based on ADV estimates of ϵ and ADCP estimates of TKE, TKE shear production, TKE time variation, and TKE turbulent transport.

The ϵ data also show reasonable trends with wind and water speed (**Figure 9**). Dissipation increases with increasing winds, regardless of current velocity, and increases with the water speed when winds are weak. These results are similar to those found by Zappa et al. [2007] for a relatively shallow and unstratified system, the Parker River estuary. However, with the SOCa data, there is no suggestion that ϵ increases with water speed when winds are moderate ($3 \leq U_{10N} \leq 6 \text{ m s}^{-1}$). This suggests that tidal currents play less of a role in controlling ϵ at the CASsIE site, likely due to stratification and a deeper water column over which bottom-generated turbulence decays.

3.4 CO₂ validation and uncertainty tests

Here, the unique autonomous CO₂ profiling and GFT approach used during CASsIE is evaluated with tests of system functionality, an examination of uncertainty, and with comparisons of the Hudson measurements with other studies. The performance of the

equilibrator was examined at the beginning of the study, when it was verified that the sampling time of 10 minutes was sufficient for equilibration to occur (the switchbox has adjustable timing). The $p\text{CO}_2$ rapidly changed from the atmospheric value to the (much higher) value for the equilibrator headspace, with an equilibration rate for the water $p\text{CO}_2$ measurement of 2-3 minutes (**Figure 10**). The initial abrupt change over ~ 10 seconds matches the time it takes for completely flushing the tubing and switchbox hardware, which we have observed in the laboratory when testing with tanks of known $[\text{CO}_2]$. The more gradual, 2-3 minute adjustment appears to correspond to the equilibration of $[\text{CO}_2]$ in the recirculating headspace air with the surface estuarine water flowing through the system. Rapid decreases in $p\text{CO}_2$ of as much as 42% are observed in the early-to-mid afternoon on sunny days (e.g. year-days 276-278, **Figure 4**), consistent with formation of a warm shallow stratified layer with high primary productivity. The sea breeze arrives in mid-afternoon, and wind- or tide-driven mixing of the stratified layer is associated with a rapid return of $p\text{CO}_2$ to near the original levels (**Chapter 5**). Few if any surface water $p\text{CO}_2$ measurements in the Hudson River estuary have been published, but fall season observations in the tidal Hudson River are similar to the observed values [*Raymond et al.*, 1997].

GFT observations of air-water CO_2 flux (F_{CO_2} ; **Figure 4**) and transfer velocity (k_{660} ; **Figure 11**) are generally consistent with a small number of prior observations made in other studies of the Hudson's tidal river and estuarine regions [*Clark et al.*, 1994; *Zappa et al.*, 2007]. Mean values of F_{CO_2} and k_{660} were $21.1 \text{ mol CO}_2 \text{ m}^{-2} \text{ y}^{-1}$ and 8.4 cm h^{-1} respectively. Recent year-round measurements in the tidal Hudson River demonstrated the dominant terms in the annual CO_2 budget are gross benthic and water column respiration

(30.8 mol CO₂ m⁻² y⁻²), CO₂ advection (<2.58), air-water CO₂ flux estimated from wind speed and the air-water ΔpCO₂ (5.83-13.5), net primary production of phytoplankton (~6.67), and an unquantified DIC advective transport term, though the budget was not closed [the discrepancy term was 8.33-16.0; *Raymond et al.*, 1997]. Our estimates show a somewhat higher mean air-water exchange, but this is not surprising because we are comparing a published annual mean value with measurements that were made at one location at the end of the warm season, when ΔpCO₂ is expected to be above the annual mean due to high respiration rates [*Raymond et al.*, 1997].

A "residual moisture bias test" was conducted throughout CASSIE to check whether there was any bias in CO₂ flux estimates made using different switchbox channels, due to residual moisture droplets in the switchbox, sample lines or LI-840. Both of the low height atmospheric sample intakes (Ch. 2, Ch. 4) were placed at the front of the vessel for this test. After channel 1 samples the water-saturated air from the equilibrator's headspace, then channels 2-4 sample relatively low humidity atmospheric air in 10-minute intervals. Residual moisture was confirmed to be present – the "switcher LI-840" samples at 2.25 m (Ch. 3) often have higher [H₂O] levels than the "stationary timeseries LI-840", which always samples air from 2.25 m. ΔC estimates computed using Ch. 2 ($\Delta C = C(z_2) - C(z_1) = C_{Ch.3} - C_{Ch.2}$) and Ch. 4 ($\Delta C = C_{Ch.3} - C_{Ch.4}$) were very similar, and no significant difference was found between their means ($\alpha > 0.33$). However, for cases with low ΔC, ΔC from Ch. 4 was typically larger (more negative) than ΔC from Ch. 2. Flux results presented in the paper were computed using the average concentration from Ch. 2 and Ch. 4 for the low height atmosphere C. A useful protection against sample-line moisture that we are now using is to

install vials of air sample drying agent (e.g. magnesium perchlorate) to dry the air samples without causing any biases to the CO₂ measurements.

Two different null tests were used to verify system functionality and quantify uncertainty: (1) with the switchbox sampling air from only one channel for several days interspersed through the study, and (2) with the switchbox cycling through the four channels, with all atmospheric air intakes located at the same height (~30 cm) for over one day. The first test showed how noise in LI-840 sampling led to uncertainty in the atmospheric CO₂ vertical concentration difference, ΔC . The observed mean ΔC was 0.00010 with a standard deviation of 0.00266 mmol m⁻³. This is nearly identical to the expected standard error for a mean concentration difference, based on the manufacturer estimated measurement uncertainty. The resulting 95% confidence intervals in k_{660} are shown in **Figure 11**. The second test showed how measurements using different sample lines impact ΔC . A mean ΔC of -0.0029 with a standard deviation of 0.00250 mmol m⁻³, indicated that there was a bias towards a negative concentration difference (and therefore a very small positive F_{CO_2} and k_{660}). The reasons for this bias are unknown, but could be caused by sample line length differences or valve obstructions that lead to flow rate differences that are not corrected for by the LI-840. This bias in ΔC was subtracted prior to computing fluxes.

Atmospheric buoyancy effects were often important during CASsIE, as a result of winds typically being weak or moderate and the air-water temperature difference being very large, often 5-10 °C. The absolute value of the Obukhov length ($|L|$) is shown in **Figure 4**, and buoyancy effects are important to ASL mixing when $|L|$ is smaller than ten times the profile height [Fairall *et al.*, 2000] of 2.25 m. For 44% of cases with F_{CO_2}

estimates, L was negative and smaller than 22.5 m, signaling convective effects were important. For 2.5% of cases with F_{CO_2} estimates, L was positive and below 22.5 m, suggesting stratification effects were important. The prior finding that COARE air-sea momentum flux estimates were inaccurate during highly stratified conditions [Edson *et al.*, 2007] suggests that the F_{CO_2} estimates for the cases with strong stratification may be inaccurate. However, these cases are infrequent, have low winds, and very small fluxes (**Figure 4**), so the total flux error over the study should be very small. GFT should be used with caution in springtime in the coastal zone because highly stable atmospheric conditions are more common.

Figure 11 shows a comparison of SOCa observations of the gas exchange velocity as a function of wind speed, versus a set of parameterizations [McGillis *et al.*, 2001a; Nightingale *et al.*, 2000; Wanninkhof, 1992]. Observed values are similar to the parameterizations, but frequently higher (double) for low and moderate wind speeds, yet generally lower for high wind speeds. The enhanced gas transfer at low winds could be a result of many factors, including rain (which will be quantified in future studies) or tidal currents. The weaker gas transfer at high winds is likely due to fetch limitation, because a fully developed sea state with frequent whitecapping was not observed to develop over a fetch as low as 1.8 km during high wind periods.

3.5 GFT applicability, profile height and footprint

The applicability of GFT relies in part on the detection of a gradient in $[\text{CO}_2]$ over distances spanned in the atmospheric profile. It can also depend on the flux footprint of the GFT measurements, for study sites with a limited wind fetch. Here, we make some simple

computations that can help determine if GFT is feasible for a given study site, based on the open space upwind (fetch), $\Delta p\text{CO}_2$, and the gas exchange velocity. The analysis can also help guide decisions on CO_2 measurement heights.

Combining Eqns. 3 and 6, assuming a quadratic drag law ($U_* = U_{10N}C_D^{0.5}$), a typical drag coefficient (C_D) of 0.0015, and negligible stability effects ($\Psi_C=0$), one can compute the profile height required to successfully observe a $[\text{CO}_2]$ gradient:

$$z_2 = z_1 \exp\left(\frac{0.41 U_* (\Delta C)_{95}}{F_{\text{CO}_2}}\right) = z_1 \exp\left(\frac{0.41 U_{10N} C_D^{0.5} (\Delta C)_{95}}{k_{660} \rho_w K_0 \Delta p\text{CO}_2}\right) \quad (7)$$

Here, z_1 and z_2 are the lowest and highest $[\text{CO}_2]$ measurements, respectively, and $(\Delta C)_{95}$ is the 95% confidence interval on the atmospheric ΔC measured in the null tests. The first equation can be used very generally with GFT for any case where *a priori* estimates of the shear velocity and flux are available (e.g. for a terrestrial canopy study). The equation to the right is only useful for air-water exchanges. The low height (z_1) profile point is typically constrained by complexity near the boundary, and was set at 10 cm for the computations below because the lower air intakes must be high enough to avoid pumping water – in calm waters (e.g. a tidal marsh channel), this could likely be reduced to a few centimeters.

The gas exchange velocity (k_{660}) for use in Eq. 7 may be computed either using a wind-based or dissipation-based parameterization. Resulting values of z_2 using the parameterization of $k_{660} = 0.31 U_{10N}^2$ [Wanninkhof, 1992] are shown in the top panel of **Figure 12**. Using this parameterization leaves U_{10N} and $\Delta p\text{CO}_2$ as the only free parameters to govern the height z_2 . The resulting heights are shown with corresponding footprints (the minimum required fetch) computed from Eq. 6. Resulting values of z_2 using the

parameterization $k_{sc} = 0.419(\epsilon\nu)^{1/4}Sc^{-1/2}$ from Zappa et al. [2007] are shown in the bottom panel, corresponding to the more general case where turbulence drives gas exchange. Here, we have assumed a constant U_{10N} of 3 m s^{-1} for use in Eq. 7. These results are based upon an assumption of negligible atmospheric stability influences, as well as a constant drag coefficient, and should be viewed as rough approximations.

For CASsIE, using Eq. 6 with $z_2 = 2.25 \text{ m}$ and typical roughness of $z_0 = 0.00025$, the footprint (λ_{90}) is 1030 m upwind from the platform. According to the top panel of **Figure 12**, z_2 was sufficiently high to observe gas exchange at any wind speed. Given that ϵ was typically above $10^{-7} \text{ W kg}^{-1}$, the bottom panel shows that the profile height and footprint could likely have been reduced below 1 m and footprint reduced to $\sim 200 \text{ m}$.

4. Discussion

The positive attributes of SOCa are not replicated in any other existing platform, and it provides a valuable new perspective for studies of air-water gas exchange and turbulence in coastal, estuarine and freshwater systems. The CO_2 profiling and flux system can also be used separately from SOCa, such as recent work examining air-canopy CO_2 fluxes on green roofs [DeLanoy et al., 2008], and is being used on air-sea CO_2 flux transects across the continental shelf using robotic boats [Higinbotham et al., 2009]. Below, we discuss the benefits of the small measurement footprint/timescale, the wider temporal and spatial coverage that can be sampled, the longer deployment durations (and prospects for extending battery life), and the unobstructed surface-following measurements of turbulence. We also suggest some simple approaches for improving the air-water exchange and turbulence measurements.

SOCa provides F_{CO_2} measurements with a relatively small footprint and timescale, and sufficient accuracy but significantly less effort relative to tracer experiments [e.g., *Clark et al.*, 1994] or studies where personnel must be present to profile instruments [e.g., *Zappa et al.*, 2003]. Compared with a timescale of days to weeks for tracer studies, the timescale of minutes or tens of minutes for GFT enables us to study sub-tidal timescales. Furthermore, small-scale features can be targeted if there are large air-water $p\text{CO}_2$ differences. Several coastal ocean sites regularly exhibit ϵ values between 10^{-4} and 10^{-3} W kg^{-1} over at least 100 m lengths, including sills [e.g., *Klymak and Gregg*, 2004], salt wedge estuaries [*MacDonald and Geyer*, 2004] and the Columbia River tidal plume front [*Orton and Jay*, 2005]. These likely exhibit strong gas exchange, and GFT measurements could be made with profile spacing of a few centimeters and a footprint below 50 m if $\Delta p\text{CO}_2$ is 1000 or greater, or a few decimeters and a footprint below 100 m if $\Delta p\text{CO}_2$ is 100 or greater (**Figure 12**).

The low expense and relative ease of deploying one or more SOCa in different locations for autonomous measurements make it a useful tool for obtaining data with broad temporal and spatial coverage. The shallow-draft SOCa may be valuable for studies of air-water gas transfer in shallow coastal regions that are inaccessible for normal research vessel based sampling, yet may be highly important for local biogeochemistry or global carbon budgets [*Borges*, 2005]. The CASsIE deployments captured the passage of fall season storm systems with mean along-estuary winds as high as 11.0 m s^{-1} (1.2 m height) gusting as high as 19 m s^{-1} (e.g. year-days 273.5-275.0 and 299.8-300.2; **Figure 4**). These periods exhibited very high air-water CO_2 fluxes ($100\text{-}200 \text{ mmol m}^{-2} \text{ d}^{-1}$), air-water

temperature differences as large as $-12\text{ }^{\circ}\text{C}$, extreme upward net air-water heat fluxes as high as 500 W m^{-2} , and strong turbulent mixing (**Chapter 4**) and deepwater ventilation.

Another strength is longevity – because all the onboard measurements are relatively insensitive to calibration drift, long-term deployments are possible. The acoustic measurements of water velocity (and turbulence) and wind velocity have negligible calibration drift. The CO_2 flux algorithm relies on air-water pCO_2 differences and vertical gradients in the lower atmosphere, and since these are made with a single sensor, the flux measurement is also relatively insensitive to calibration drift. Deployments during CASsIE were as long as 11 days, and much longer durations are possible; SOCa was only towed in for equipment upgrades. This is a substantial improvement upon prior sampling that required a boat and personnel for manual profiling (e.g. Zappa et al., 2003). Looking ahead, replacement of the powerful water pump and large equilibrator with a commercial long-term pCO_2 monitoring system [e.g., SAMI-CO₂, Sunburst Sensors; *DeGrandpre et al.*, 1995] and the computer with a low-power data logger would greatly reduce the need for battery changes.

A shortcoming with the SOCa measurements is that use of the bulk heat and momentum fluxes in the processing will obscure some detail of the CO_2 flux variability and forcing. One relatively simple improvement to address this issue has already been made in a more recent experiment, by adding a second sonic anemometer (**Figure 2**). Sonic anemometers have virtually no calibration drift, so collecting a two-point wind profile with an additional wind velocity sensor at a different height can provide accurate atmospheric gradients and improved estimates of momentum fluxes and U^* . An additional relatively simple improvement would be to add a thermocouple for a highly accurate two-point

atmospheric temperature gradient, improving estimates of the air-water sensible heat flux. The LI-840 measurement of humidity was sampling different atmospheric heights through the switchbox, but residual moisture in the system made estimation of the humidity gradient difficult. Relative humidity probes can be mounted at different heights, but care must be taken that the sensors are inter-calibrated and the sensor resolution is sufficient to capture a sufficiently small humidity gradient.

SOCa self-orientates and provides undisturbed turbulence measurements near the water surface, which are rarely made because free-falling micro-scale sensors typically begin their profile at 2-3 m depth [e.g., *Peters and Bokhorst, 2000*]. Turbulent mixing of constituents in the upper meter of the water column is relatively poorly understood, yet can be highly important for surface oriented pollutants, surface-oriented biological constituents, or air-water exchanges [*Nimmo-Smith et al., 1999*]. A potential weakness of the platform is applicability in cases with steep or breaking waves, when the turbulence measurements become difficult due either to (1) orbital velocities being larger than mean velocities, violating Taylor's assumption, and (2) pitching of the vessel. Currently, data is masked during wavy conditions, but field testing with multiple instruments and windy conditions would be useful to better understand the impact of winds and waves on measurement accuracy. A potential solution to these problems that could extend the applicability of the platform is to use a high-resolution pulse-coherent sonar with O(1 cm) spatial resolution to measure water velocity, avoiding the use of Taylor's assumption (e.g. a Nortek Aquadopp with high-resolution sampling upgrade).

Our goal in the ongoing research with SOCa is to make observations under a wide range of conditions at several sites and provide the research community with improved,

multi-parameter gas exchange and turbulence models. More broadly, methods presented in this paper may be useful for any autonomous study of air-water mass, heat or momentum exchange. These studies are becoming more common due to interest in climate change and the movement toward construction of a complete Earth observation system.

References

- Birdsey, R., et al. (2009), Carbon Cycle Observations: Gaps Threaten Climate Mitigation Policies, *EOS Trans. AGU*, 90(34).
- Borges, A. V. (2005), Do we have enough pieces of the jigsaw to integrate CO₂ fluxes in the coastal ocean?, *Estuaries*, 28(1), 3-27.
- Broecker, W. S., and T. Takahashi (1966), Calcium Carbonate Precipitation on the Bahama Banks, *J. Geophys. Res.*, 71.
- Businger, J. A., J. C. Wyngaard, Y. Izumi, and E. F. Bradley (1971), Flux profile relationships in the atmospheric surface layer, *J. Atmos. Sci.*, 28, 181-189.
- Clark, J. F., R. Wanninkhof, P. Schlosser, and H. J. Simpson (1994), Gas exchange rates in the tidal Hudson River using a dual tracer technique, *Tellus*, 46B, 274-285.
- Dai, M., X. Guo, W. Zhai, L. Yuan, B. Wang, L. Wang, P. Cai, T. Tang, and W.-J. Cai (2006), Oxygen depletion in the upper reach of the Pearl River estuary during a winter drought, *Mar. Chem.*, 102(1-2), 159-169.
- DeGrandpre, M. D., T. R. Hammar, S. P. Smith, and F. L. Sayles (1995), In situ measurements of seawater pCO₂, *Limnol. Oceanogr.*, 40(5), 969-975.
- DeLanoy, J. T., P. M. Orton, and W. R. McGillis (2008), Quantification of green roof carbon dioxide, heat, and water fluxes using the gradient flux technique, *EOS Trans. AGU*, 89(53), Fall Meet. Suppl., Abstract B43D-0470.
- Edson, J. B., W. R. McGillis, and T. C. Austin (2000), A new coastal observatory is born, *Oceanus*, 42(1), 31-33.

- Edson, J. B., C. J. Zappa, J. Ware, W. R. McGillis, and J. E. Hare (2004), Scalar flux profile relationships over the open ocean, *J. Geophys. Res.*, *109*(C08S09).
- Edson, J. B., et al. (2007), The Coupled Boundary Layers and Air-Sea Transfer Experiment in Low Winds (CBLAST-LOW), *Bulletin of the American Meteorological Society*, *88*(3), 341-356.
- Fairall, C. W., J. E. Hare, J. B. Edson, and W. McGillis (2000), Parameterization and Micrometeorological Measurement of Air-Sea Gas Transfer, *Boundary-Layer Meteorol.*, *96*(1), 63-106.
- Fairall, C. W., E. F. Bradley, J. E. Hare, A. A. Grachev, and J. B. Edson (2003), Bulk Parameterization of Air-Sea Fluxes: Updates and Verification for the COARE Algorithm, *J. Clim.*, *16*(4), 571-591.
- Gash, J. H. C. (1986), A note on estimating the effect of a limited fetch on micrometeorological evaporation measurements, *Boundary-Layer Meteorol.*, *35*(4), 409-413.
- Gill, A. E. (1982), *Atmosphere-Ocean Dynamics*, 662 pp., Academic Press, San Diego.
- Graber, H. C., E. A. Terray, M. A. Donelan, W. M. Drennan, J. C. Van Leer, and D. B. Peters (2000), ASIS: A New Air-Sea Interaction Spar Buoy: Design and Performance at Sea, *J. Atmos. Oceanic Technol.*, *17*(5), 708-720.
- Higinbotham, J. R., J. R. Moisan, and P. M. Orton (2009), Solar Powered Autonomous Surface Vehicle Development and Operation, *Sea Technol.*, *50*(7), 10-13.
- Jonas, T., A. Stips, W. Eugster, and A. Wuest (2003), Observations of a quasi shear-free lacustrine convective boundary layer: Stratification and its implications on turbulence, *J. Geophys. Res.*, *108*.
- Klymak, J. M., and M. C. Gregg (2004), Tidally Generated Turbulence over the Knight Inlet Sill, *J. Phys. Oceanogr.*, *34*(5), 1135-1151.
- Launiainen, J., and T. Vihma (1990), Derivation of turbulent surface fluxes - an iterative flux-profile method allowing arbitrary observing heights, *Environmental Software*, *5*, 113-124.

Liss, P. S. (1983), Gas transfer: experiments and geochemical implications, in *Air-sea exchange of gases and particles*, edited by P. S. Liss and W. G. Slinn, pp. 241-299, Reidel, Dordrecht, The Netherlands.

Lumley, J. L., and E. A. Terray (1983), Kinematics of turbulence converted by a random wave field, *J. Phys. Oceanogr.*, *13*, 2000-2007.

MacDonald, D. G., and W. R. Geyer (2004), Turbulent energy production and entrainment at a highly stratified estuarine front, *J. Geophys. Res.*, *109*, C05004.

McGillis, W., J. B. Edson, J. E. Hare, and C. W. Fairall (2001a), Direct covariance air-sea CO₂ fluxes, *J. Geophys. Res.*, *106*, 16,729-716,745.

McGillis, W. R., J. B. Edson, J. D. Ware, J. W. H. Dacey, J. E. Hare, C. W. Fairall, and R. Wanninkhof (2001b), Carbon dioxide flux techniques performed during GasEx-98, *Mar. Chem.*, *75*, 267-280.

McGillis, W. R., J. B. Edson, J. D. Ware, J. W. H. Dacey, J. E. Hare, C. W. Fairall, and R. Wanninkhof (2001c), Carbon dioxide flux techniques performed during GasEx-98, *Mar. Chem.*, *75*, 267-280.

McGillis, W. R., et al. (2004), Air-sea CO₂ exchange in the equatorial Pacific, *J. Geophys. Res.*, *109*, C08S02.

McGillis, W. R., and R. Wanninkhof (2006), Aqueous CO₂ gradients for air-sea flux estimates, *Mar. Chem.*, *98*(1), 100-108.

Monin, A. S., and A. M. O. Obukhov (1954), Fundamentale Gesetzmäßigkeiten der turbulenten Vermischung in der bodennahen Schicht der Atmosphäre, in *Sammelband zur Statistischen Theorie der Turbulenz*, edited by H. Goering, pp. 199-226, Dtsch. Akad. der Wissensch zu Berlin, Berlin.

Moog, D. B., and G. H. Jirka (1999), Air-water gas transfer in uniform channel flow, *J. Hydraul. Engin.*, *125*(1), 3-10.

Newberger, T. (2004), Underway P_{CO2} System Users Manual, edited, Lamont-Doherty Earth Observatory CO₂ Group.

Nightingale, P. D., G. Malin, C. S. Law, A. J. Watson, P. S. Liss, M. I. Liddicoat, J. Boutin, and R. C. Upstill-Goddard (2000), In situ evaluation of air-sea gas exchange parameterizations using novel conservative and volatile tracers, *Glob. Biogeochem. Cycle*, 14(1), 373-387.

Nimmo-Smith, W. A. M., S. A. Thorpe, and A. Graham (1999), Surface effects of bottom-generated turbulence in a shallow tidal sea, *Nature*, 400, 251-254.

Orton, P. M., and D. A. Jay (2005), Observations at the tidal plume front of a high-volume river outflow, *Geophys. Res. Lett.*, 32, L11605.

Peters, H., and R. Bokhorst (2000), Microstructure Observations of Turbulent Mixing in a Partially Mixed Estuary. Part I: Dissipation Rate, *J. Phys. Oceanogr.*, 30(6), 1232-1244.

Raymond, P. A., N. F. Caraco, and J. J. Cole (1997), Carbon dioxide concentration and atmospheric flux in the Hudson River, *Estuaries*, 20(2), 381-390.

Salter, M. E., R. C. Upstill-Goddard, and P. D. Nightingale (2008), DOGEE-SOLAS: The role of surfactants in air-sea gas exchange, *EOS Trans. AGU Fall Meet. Suppl., Abstract OS22B-03*, 89(53).

Vesala, T., N. Kljun, Ü. Rannik, J. Rinne, A. Sogachev, T. Markkanen, K. Sabelfeld, T. Foken, and M. Y. Leclerc (2008), Flux and concentration footprint modelling: State of the art, *Environmental Pollution*, 152(3), 653-666.

Voulgaris, G., and J. H. Trowbridge (1998), Evaluation of the acoustic- Doppler velocimeter (ADV) for turbulence measurements, *J. Atmos. Oceanic Technol.*, 15, 272-289.

Wanninkhof, R. (1992), Relationship between wind speed and gas exchange over the ocean, *J. Geophys. Res.*, 97(C5), 7373-7382.

Weiss, R. F. (1974), Carbon dioxide in water and seawater: The solubility of a non-ideal gas, *Marine Chemistry*, 2(203-215).

YSI-Sontek (2009), Sontek ADV principles of operation, <http://www.sontek.com/princop/adv/advpo.htm>, edited.

Zappa, C., W. McGillis, P. Raymond, J. Edson, E. Hints, H. Zemelink, J. Dacey, and D. Ho (2007), Environmental turbulent mixing controls on air-water gas exchange in marine and aquatic systems, *Geophys. Res. Lett.*, 34(10), 10601.

Zappa, C. J., P. A. Raymond, E. Terray, and W. R. McGillis (2003), Variation in surface turbulence and the gas transfer velocity over a tidal cycle in a macro-tidal estuary, *Estuaries*, 26(6), 1401-1415.

Figure Captions

Figure 1: Plan view of SOCa with the autonomous atmosphere and water CO₂ profiling system, focusing on basic structural components and the air sampling lines. The keel "vanes" (spins) the float so that the water velocity sensor on mount bracket #1 is always oriented into the current. The bracket holds one or more acoustic Doppler velocimeters (ADVs) at user-selectable depths, typically 10-50 cm.

Figure 2: Photos of SOCa during (a) the 2007 CASsIE study (Carbon and Air-Sea Interaction in an Estuary), and (b) a 2008 experiment with only water turbulence and wind shear measurements. Sensor heights for CASsIE are given in **Table 1**, and the equilibrator (Eq) is shown at center, with insulation and a white cover, to minimize solar heating. The 2008 study included two anemometers to measure atmospheric shear.

Figure 3: Example inertial dissipation method fits of the power spectral density of vertical velocity (Φ_3) for estimating TKE dissipation (ϵ), using the Kolmogorov + Noise (K+N) approach – (top) a case where the Kolmogorov model dominates; (bottom) a case where the scaled Noise basis function is of a similar magnitude to the Kolmogorov basis function. The low-wavenumber boundary to the inertial subrange estimated using the inertial sensor and the high-wavenumber boundary due to ADV spatial averaging are also shown (bound1, bound2), as well as the ratio of rms model-data fit to spectral mean, $\text{rms}/\text{mean}(\Phi_3)$.

Figure 4: CASsIE field experiment observations and flux estimates made from SOCa, including (from the top, down): air and water temperature (T_{air} , T_{water}) and relative humidity

(RH), measured wind speed ($U_{1,2}$) and equivalent neutral 10 m speed (U_{10N}), sensible and latent heat flux, the absolute value of Obukhov length (L), water $p\text{CO}_2$, air-water CO_2 flux (F_{CO_2}), and dissipation (ϵ). SOCa was out of the water for upgrades from year-day 288-298.

Figure 5: SOCa rotational orientation, with each black point representing a 10-minute mean water velocity vector emanating from the point and aiming toward the target center (direction of fluid movement), relative to the direction SOCa is pointing (0°). Observed wind velocity (U) vectors divided by 10 are also shown as grey points.

Figure 6: SOCa rotational orientation as a function of 10 m wind speed, for water speeds above 0.2 m s^{-1} . Dashed lines show -60° and $+60^\circ$, conservative cutoffs beyond which flow interference from the pontoons could bias velocity or turbulence estimates.

Figure 7: SOCa pitch angle standard deviations for 10-minute periods over the entire CASsIE study, plotted as a function of the equivalent neutral 10 m wind speed. Roll angle variability was typically similar or smaller than pitch variability.

Figure 8: Comparison of catamaran-mounted ADV and bottom-mounted ADCP measurements of surface water speed (points) during CASsIE, with a linear regression (line) and regression statistics in the upper left corner.

Figure 9: Dissipation bin-averages for different wind and water speeds, with errorbars showing 95% confidence intervals. At least five 10-minute average ϵ estimates were

required in a bin to compute an average for display on the plot. Wind speed bins are shown in the legend, and water speed bins were 0.20-0.35, 0.35-0.50, 0.50-0.65, and 0.65-0.80 m s⁻¹.

Figure 10: Three typical cases showing the fractional equilibration of pCO₂ in the equilibrator headspace over 10-minute intervals. The switchbox initially (time zero) sends the LI-840 air from an atmospheric sample, and then switches to the equilibrator sample. The headspace is not initially at equilibrium because the LI-840 return flow is always routed to the equilibrator – a closed loop only exists when the switchbox is sampling the equilibrator air. Equilibrator air sample pCO₂ typically reaches 95% equilibration in ~2 minutes.

Figure 11: The relationship between observed wind speed and gas transfer velocity, compared with three well-known parameterizations, for CASsIE. Errorbars show how the estimated 95% confidence in ΔC from null tests, a constant, propagates into k_{660} – the uncertainty grows as a linear function of U_{10N} (or similarly U_*) because the computed F_{CO_2} and k_{660} are linearly proportional to U_* (Eqs. 4-5). The errorbars were computed using mean K_0 and ΔpCO_2 values from the study, using integer values of U_{10N} to compute U_* .

Figure 12: Guidance for planning the CO₂ profile height for the gradient flux technique (GFT) when (**top**) wind or (**bottom**) turbulence (due to other processes) governs gas exchange. The lower height air sample intake is assumed to be 0.10 m above the water line, and 0.10 + Δz is the height of the upper air intake (Eq. 7). Shading shows the Δz required to

detect a gradient greater than the 95% confidence interval on the ΔC measurement. The corresponding 90% footprint length (λ_{90}) is also shown, based on the profile height (Eq. 6).

Gas exchange is parameterized as a quadratic function of U_{10N} for the top panel [Wanninkhof, 1992], and proportional to $\varepsilon^{1/4}$ for the bottom panel [Zappa *et al.*, 2007].

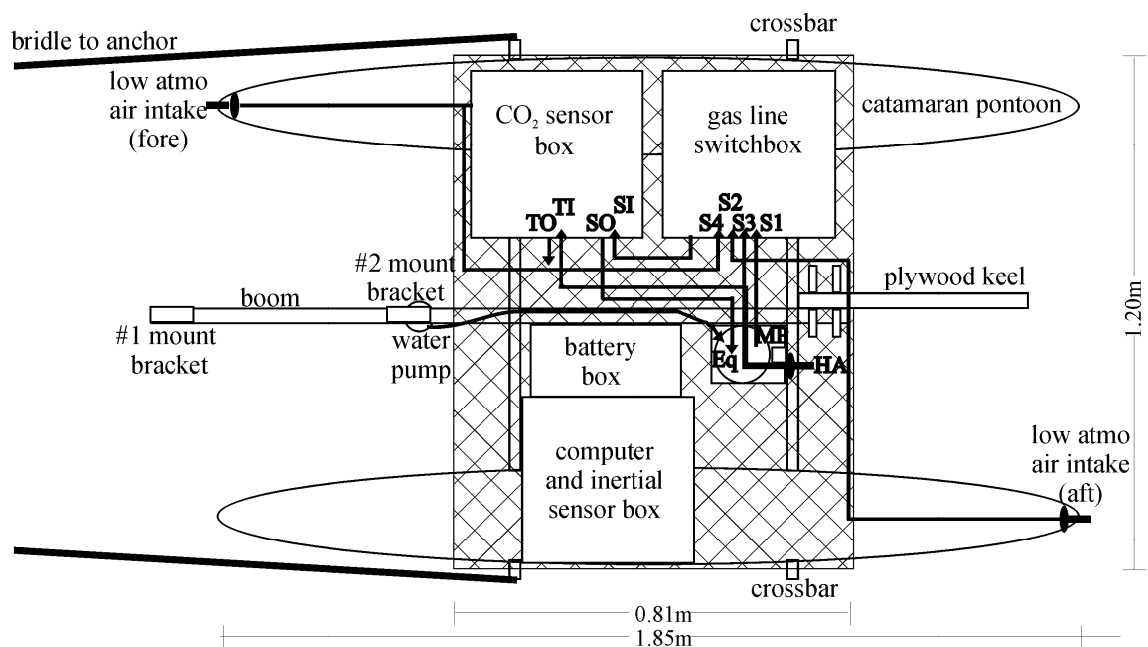
These results are based on uncertainty from null tests with SOCa and using 10-minute averaging; reduced uncertainty (lower Δz , λ_{90}) is possible with additional averaging or more precise measurement systems.

Table 1: Sensors, their vertical locations, and sample rates on SOCa during the CASsIE study

Model / description	Variables	z^a (m)	Location	Rate (Hz)
Gill Wind Observer II	temperature, wind velocity	1.2	top of mast	2
Sontek 10 MHz ADV	water u, v, w, ϵ	-0.5	forward	25
Licor LI-840 (switchbox)	equilibrator (water)	-0.2	forward	1
	[CO ₂]	0.4	forward ^b	1
	air [CO ₂], [H ₂ O]	2.25	top of mast	1
	air [CO ₂], [H ₂ O]			
Licor LI-840 (timeseries)	air [CO ₂], [H ₂ O]	2.25	top of mast	1
RBR chain of TR-1050s	water temperature	profile	anchor line	0.02
Crossbow VG400MA-100	angular rates, linear accels.	0.3	box on deck	25

a: shows measurement height (depths negative), or gas intake height for Licor sensors

b: both intakes were at the front for a residual moisture test throughout CASsIE (see Assessment section)



MP: mast on rectangular mounting plate
 Eq: water sample CO₂ equilibrator, draining downward through hole in mounting plate
 HA: high atmosphere air intakes (2 separate) at top of mast
 TI, TO, SI, SO: air sample inputs (I) and outputs (O) for (T) time series and (S) switchbox
 S1, S2, S3, S4: air sample inputs to switchbox

Figure 1: Plan view of SOCa with the autonomous atmosphere and water CO₂ profiling system, focusing on basic structural components and the air sampling lines. The keel "vanes" (spins) the float so that the water velocity sensor on mount bracket #1 is always oriented into the current. The bracket holds one or more acoustic Doppler velocimeters (ADVs) at user-selectable depths, typically 10-50 cm.

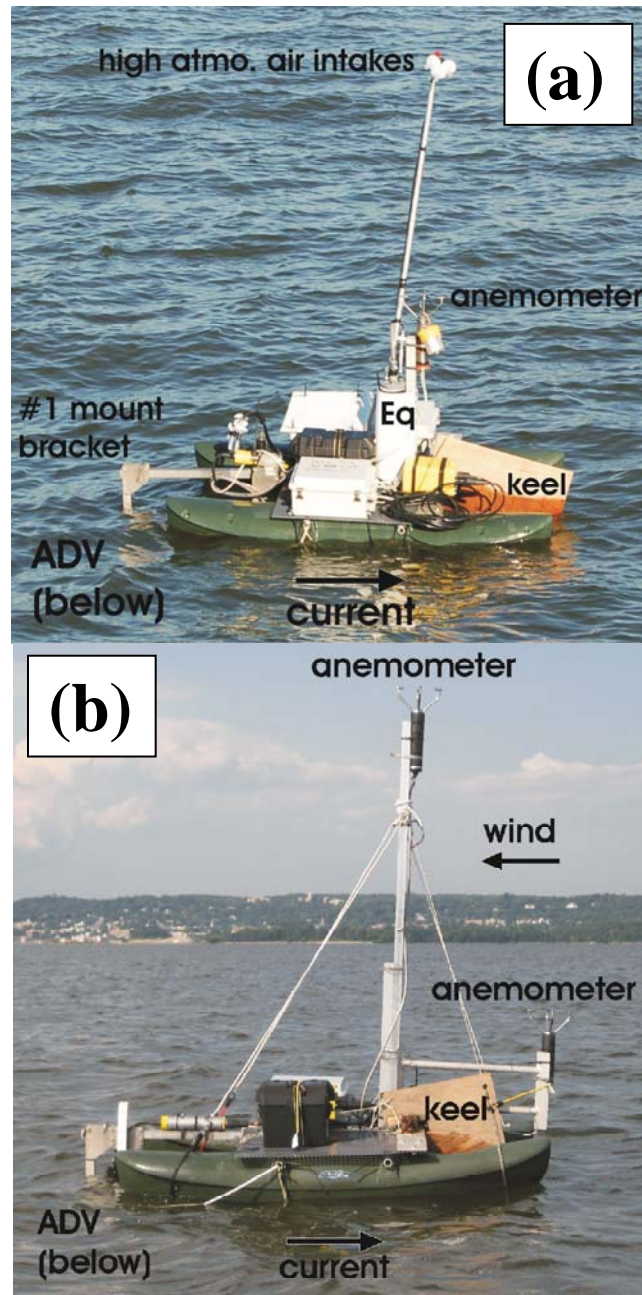


Figure 2: Photos of SOCa during (a) the 2007 CASsIE study (Carbon and Air-Sea Interaction in an Estuary), and (b) a 2008 experiment with only water turbulence and wind shear measurements. Sensor heights for CASsIE are given in **Table 1**, and the equilibrator (Eq) is shown at center, with insulation and a white cover, to minimize solar heating. The 2008 study included two anemometers to measure atmospheric shear.

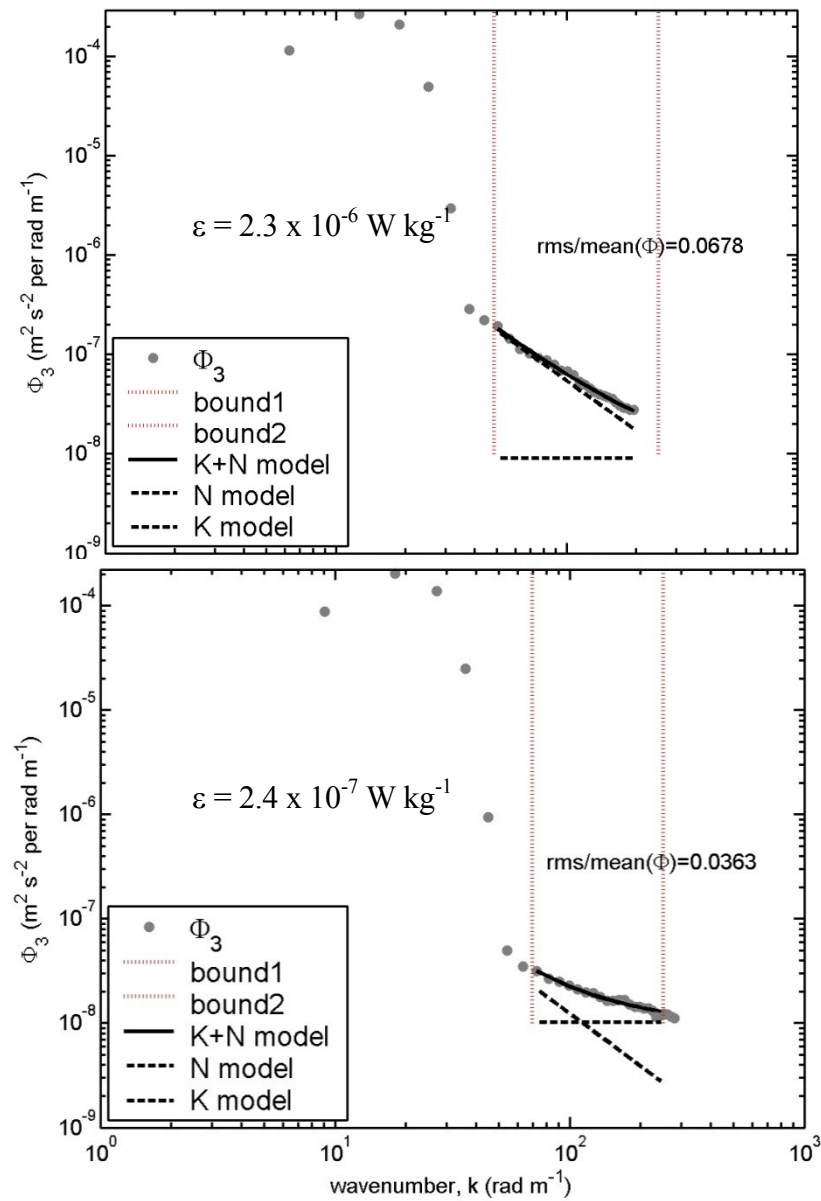


Figure 3: Example inertial dissipation method fits of the power spectral density of vertical velocity (Φ_3) for estimating TKE dissipation (ε), using the Kolmogorov + Noise (K+N) approach – (top) a case where the Kolmogorov model dominates; (bottom) a case where the scaled Noise basis function is of a similar magnitude to the Kolmogorov basis function. The low-wavenumber boundary to the inertial subrange estimated using the inertial sensor and the high-wavenumber boundary due to ADV spatial averaging are also shown (bound1, bound2), as well as the ratio of rms model-data fit to spectral mean, $\text{rms/mean}(\Phi_3)$.

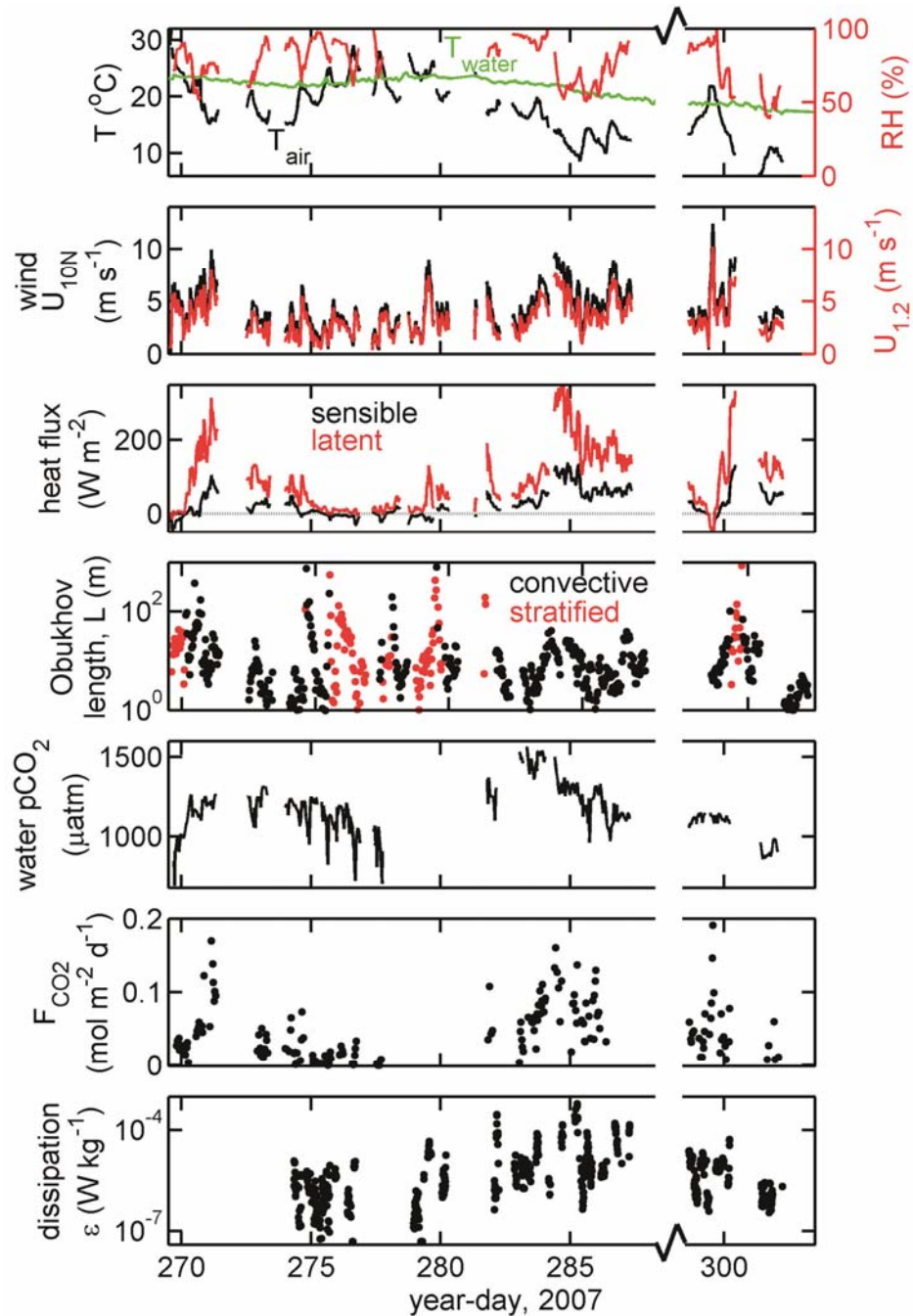


Figure 4: CASsIE field experiment observations and flux estimates made from SOCa, including (from the top, down): air and water temperature (T_{air} , T_{water}) and relative humidity (RH), measured wind speed ($U_{1,2}$) and equivalent neutral 10 m speed (U_{10N}), sensible and latent heat flux, the absolute value of Obukhov length (L), water $p\text{CO}_2$, air-water CO_2 flux (F_{CO_2}), and dissipation (ϵ). SOCa was out of the water for upgrades from year-day 288-298.

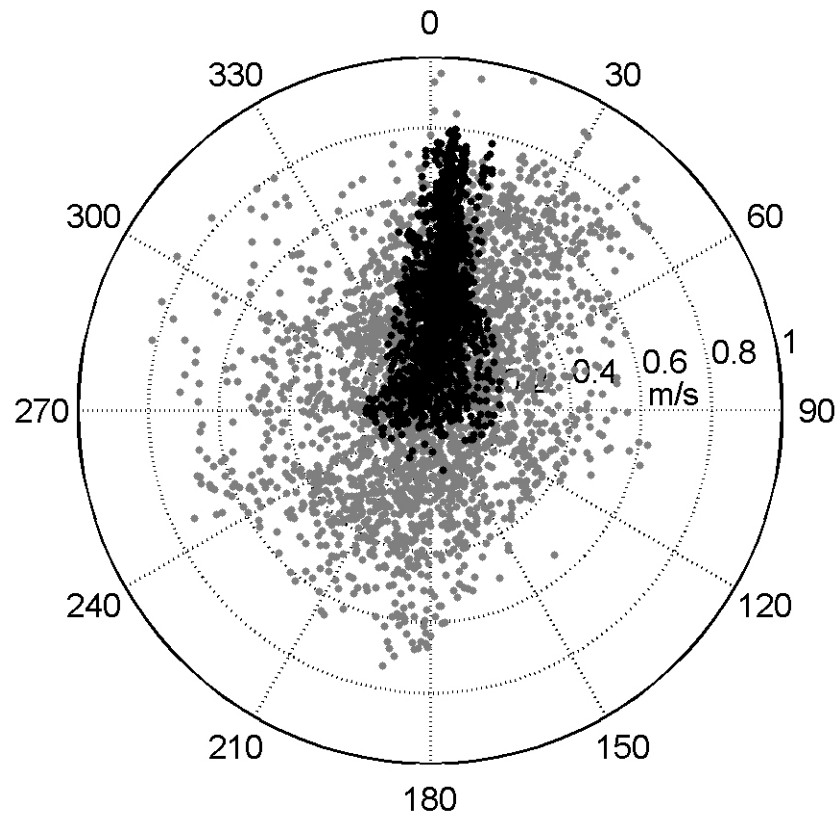


Figure 5: SOCa rotational orientation, with each black point representing a 10-minute mean water velocity vector emanating from the point and aiming toward the target center (direction of fluid movement), relative to the direction SOCa is pointing (0°). Observed wind velocity (U) vectors divided by 10 are also shown as grey points.

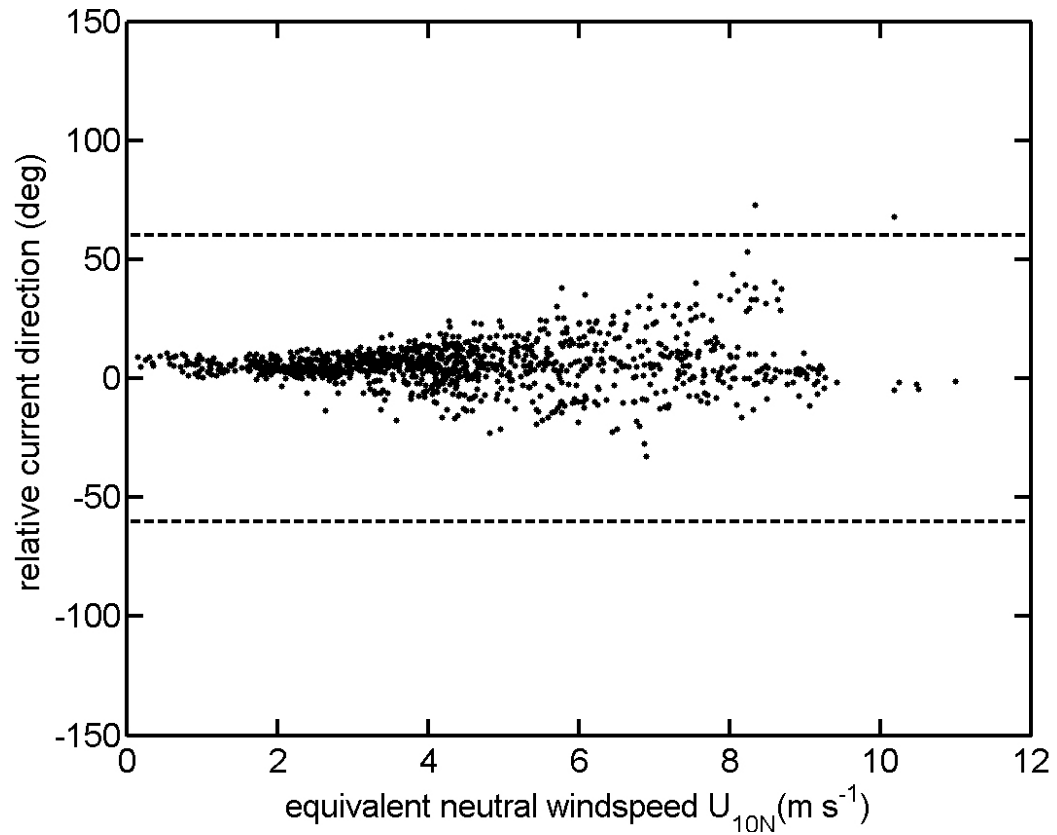


Figure 6: SOCa rotational orientation as a function of 10 m wind speed, for water speeds above $0.2 m s^{-1}$. Dashed lines show -60° and $+60^\circ$, conservative cutoffs beyond which flow interference from the pontoons could bias velocity or turbulence estimates.

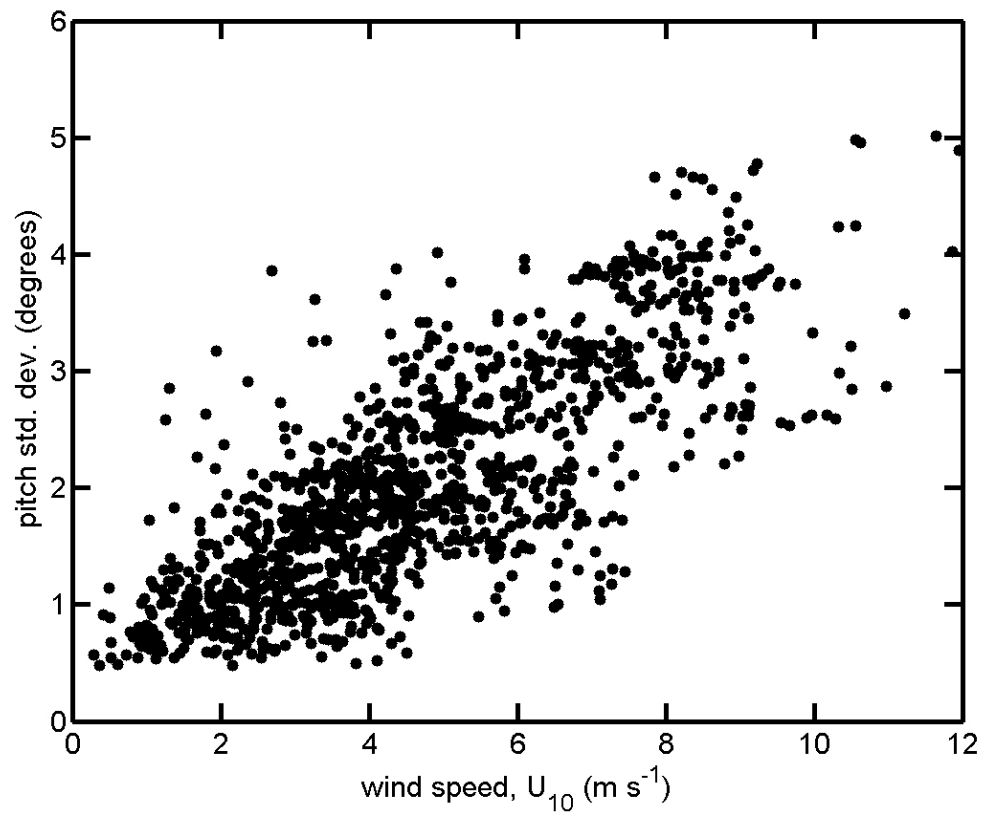


Figure 7: SOCa pitch angle standard deviations for 10-minute periods over the entire CASSIE study, plotted as a function of the equivalent neutral 10 m wind speed. Roll angle variability was typically similar or smaller than pitch variability.

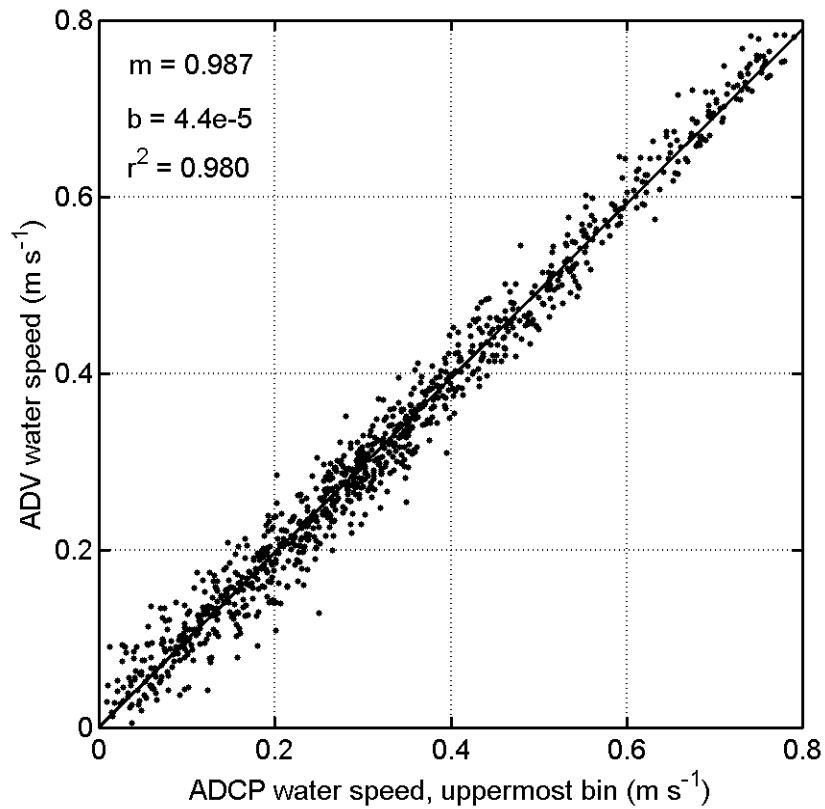


Figure 8: Comparison of catamaran-mounted ADV and bottom-mounted ADCP measurements of surface water speed (points) during CASSIE, with a linear regression (line) and regression statistics in the upper left corner.

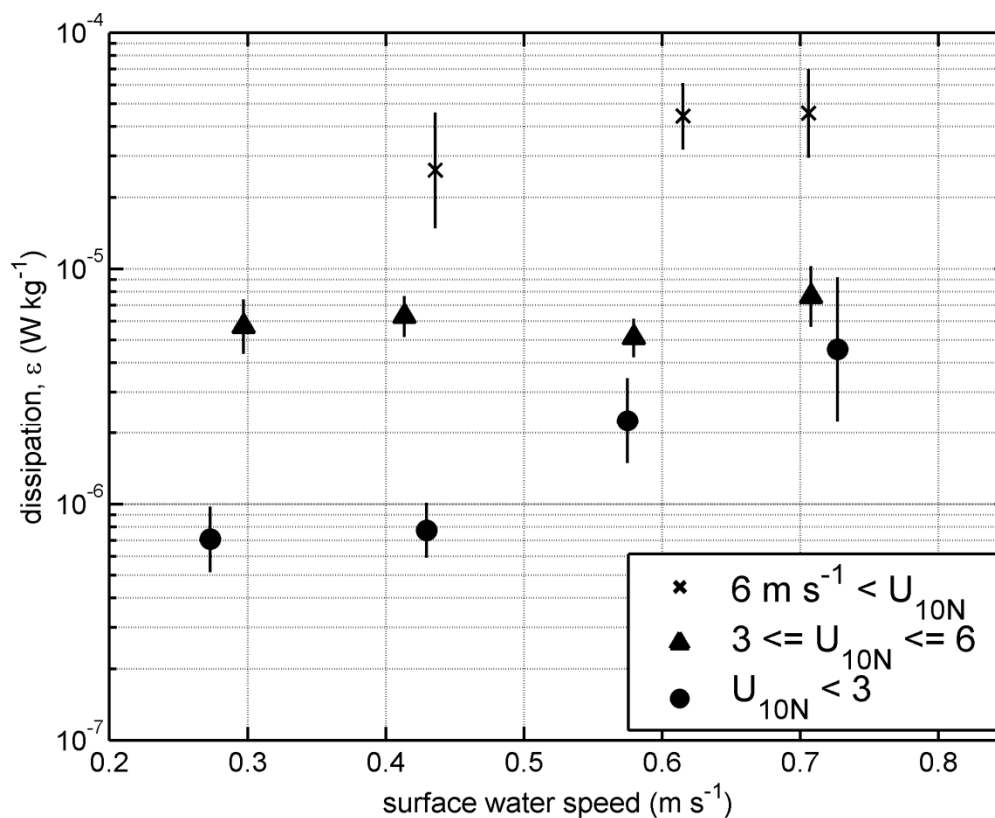


Figure 9: Dissipation bin-averages for different wind and water speeds, with errorbars showing 95% confidence intervals. At least five 10-minute average ϵ estimates were required in a bin to compute an average for display on the plot. Wind speed bins are shown in the legend, and water speed bins were 0.20-0.35, 0.35-0.50, 0.50-0.65, and 0.65-0.80 m s^{-1} .

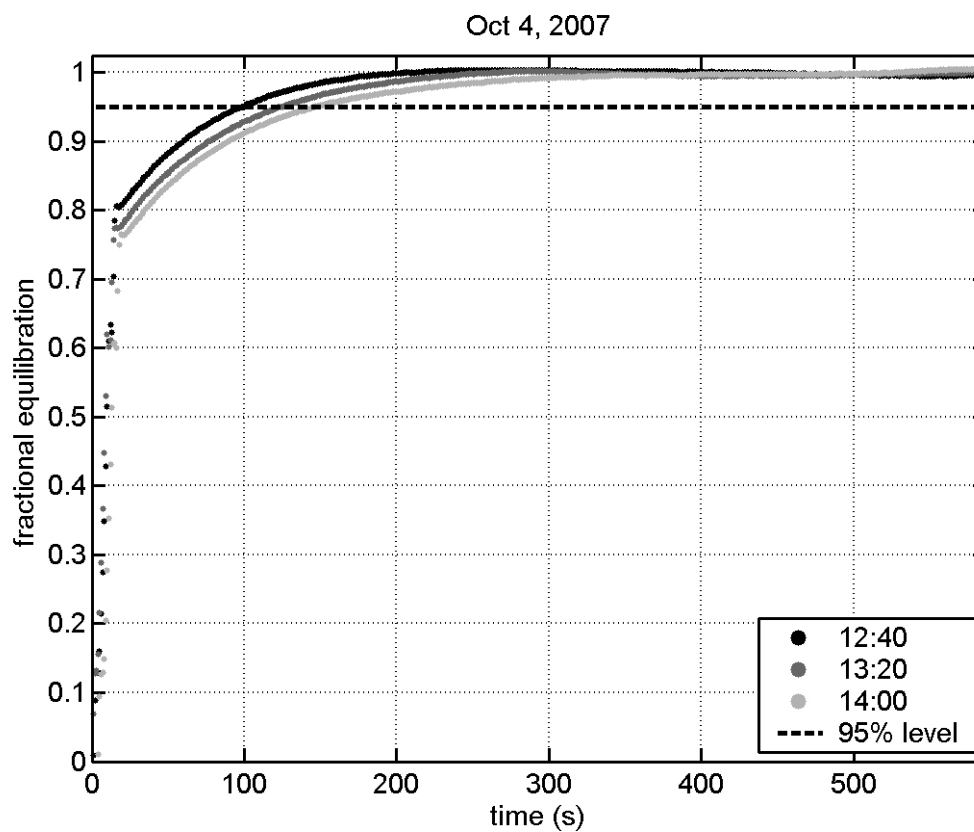


Figure 10: Three typical cases showing the fractional equilibration of $p\text{CO}_2$ in the equilibrator headspace over 10-minute intervals. The switchbox initially (time zero) sends the LI-840 air from an atmospheric sample, and then switches to the equilibrator sample. The headspace is not initially at equilibrium because the LI-840 return flow is always routed to the equilibrator – a closed loop only exists when the switchbox is sampling the equilibrator air. Equilibrator air sample $p\text{CO}_2$ typically reaches 95% equilibration in ~ 2 minutes.

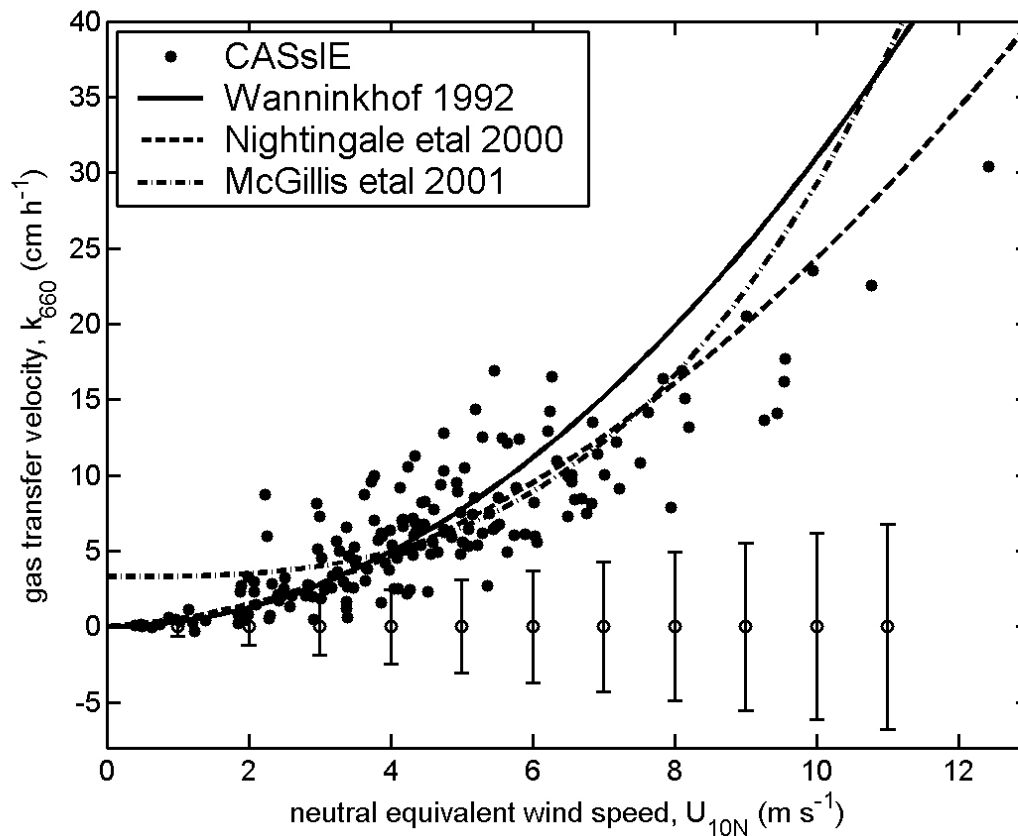


Figure 11: The relationship between observed wind speed and gas transfer velocity, compared with three well-known parameterizations, for CASSIE. Errorbars show how the estimated 95% confidence in ΔC from null tests, a constant, propagates into k_{660} – the uncertainty grows as a linear function of U_{10N} (or similarly U_*) because the computed F_{CO_2} and k_{660} are linearly proportional to U_* (Eqs. 4-5). The errorbars were computed using mean K_0 and ΔpCO_2 values from the study, using integer values of U_{10N} to compute U_* .

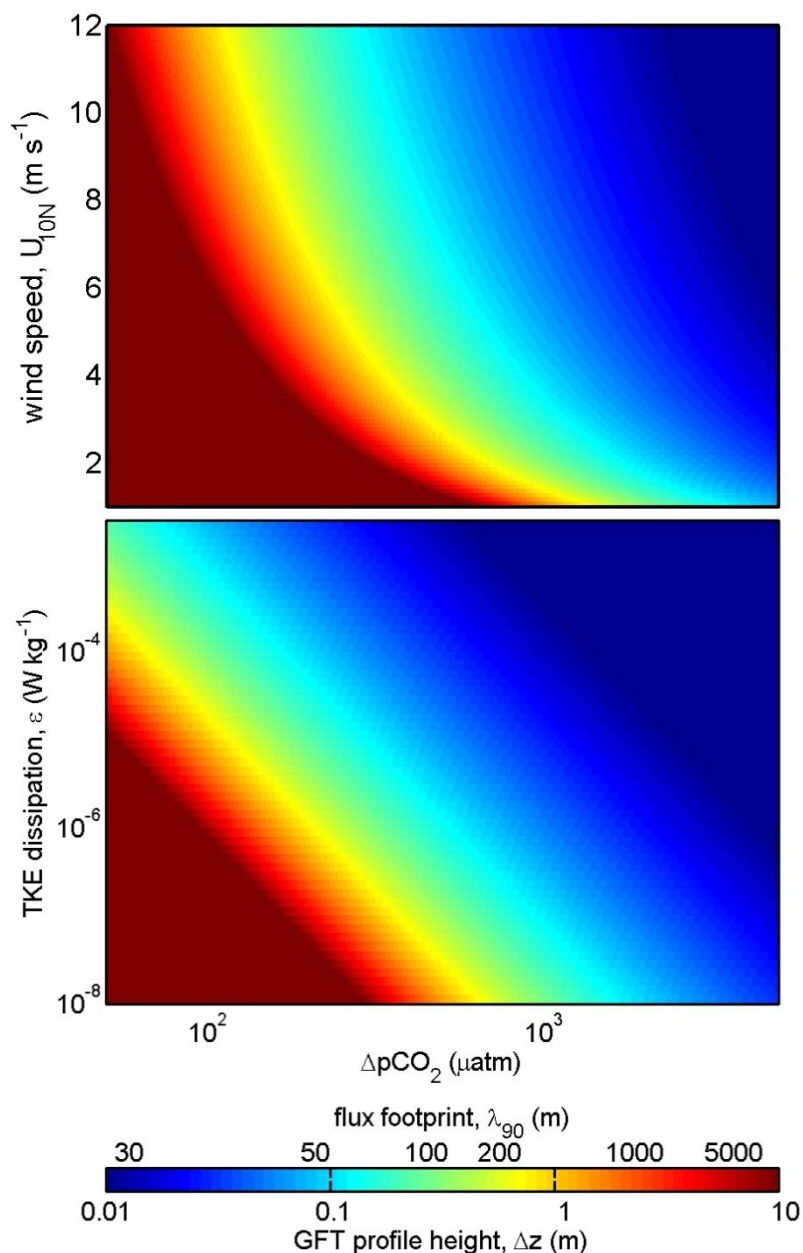


Figure 12: Guidance for planning the CO₂ profile height for the gradient flux technique (GFT) when (**top**) wind or (**bottom**) turbulence (due to other processes) governs gas exchange. The lower height air sample intake is assumed to be 0.10 m above the water line, and 0.10 + Δz is the height of the upper air intake (Eq. 7). Shading shows the Δz required to detect a gradient greater than the 95% confidence interval on the ΔC measurement. The corresponding 90% footprint length (λ_{90}) is also shown, based on the profile height (Eq. 6). Gas exchange is parameterized as a quadratic function of U_{10N} for the top panel [Wanninkhof, 1992], and proportional to $\varepsilon^{1/4}$ for the bottom panel [Zappa *et al.*, 2007]. These results are based on uncertainty from null tests with SOCa and using 10-minute averaging; reduced uncertainty (lower Δz, λ_{90}) is possible with additional averaging or more precise measurement systems.

Chapter 4

TIDAL AND ATMOSPHERIC INFLUENCES ON NEAR-SURFACE TURBULENCE IN AN ESTUARY

Abstract

Estuarine near-surface turbulence is important for transport, mixing, and air-water exchanges of many important constituents, but has rarely been studied in detail. Here, we analyze a unique set of estuarine observations of *in situ* atmospheric and full water column measurements, estimated air-sea exchanges, and acoustic measurements of several terms in the turbulent kinetic energy (TKE) budget. Observations from a 5.1 m deep site in the Hudson River estuary include dissipation at 50 cm depth (ϵ_{50}), as well as profiles of TKE, shear production of TKE (P), and net turbulent vertical TKE transport (T_D). Regressions suggest that the principal controlling factor for ϵ_{50} was wind (through the surface shear velocity, U_*), and that the surface heat flux and tidal currents also play a role. For spring tides, the TKE budget at 50 cm depth is closed within noise levels. Ebbs have high ϵ_{50} similar to the bed-driven wall layer model, due to local shear production, which nearly balances ϵ_{50} . Floods have T_D approaching P in the upper water column, but generally weak near-surface shear and turbulence. Examining buoyancy fluxes that impact stratification and can indirectly control turbulence, solar heat input and tidal straining caused similar buoyancy fluxes on a sunny, calm weather day, promoting ebb tide restratification. Wind-driven mixing was found to dominate during a fall-season storm event, but strong overnight heat loss after the storm helped delay restratification afterward. These results demonstrate the utility of combining detailed air-sea interaction and physical oceanographic measurements in future estuary studies.

1. Introduction

Turbulent mixing in the upper water column of the coastal ocean, in contrast to its well-known neighbor bottom boundary layer mixing, is not well-understood and presents difficulties for observations and numerical modeling. One of the primary remaining shortcomings of coastal and estuarine three-dimensional numerical models is that the upper water column salinity structure is poorly predicted [*Li et al.*, 2005; *Souza et al.*, 2008; *Warner et al.*, 2005]. Moreover, due to the role of salt determining density, an inaccurate modeled vertical salinity structure leads to reduced skill in predicting the estuarine circulation and longitudinal salinity gradient [*Warner et al.*, 2005].

Near-surface turbulence in the upper few meters of estuaries and the coastal ocean is also important for constituent transport. This is especially the case for surface oriented pollutants such as oil slicks or contaminants transported in buoyant freshwater in combined sewer overflows; biological particles such as plankton, which can often only grow in surface estuarine waters because of light limitation by turbidity [*Malone*, 1977]; and fine sediments and particle-associated pollutants that arrive in the estuary in buoyant river water and have a nonlinear response to turbulent mixing (and thus, increasing salinity) because it facilitates particle aggregation and sedimentation. There is a strong role for near-surface turbulence for constituents with fluxes across the air-water interface in a gaseous phase (e.g. oxygen, carbon dioxide, PCBs), because turbulence near the sea-surface governs gas transfer [*Zappa et al.*, 2007].

Estuaries are highly diverse in terms of stratification, wind fetch, tidal range and depth, as well as many other factors. As a result, in some cases near-surface turbulence will have similarity to lakes, rivers, or the open ocean. In the open ocean, processes resulting

from wind forcing such as direct wind-driven shear, wave breaking [e.g., *Gemmrich and Farmer, 2004*] or Langmuir circulation [e.g., *Gargett and Wells, 2007*] are often dominant. In lakes, the surface heat flux is an important factor for turbulence, with seasonal or diurnal convective overturning [*Imberger, 1985*]. In rivers and strongly forced, unstratified systems, near-surface turbulence is mainly related to water speed and depth. Even in 30 m depth waters in the North Sea, large-scale coherent turbulent flow structures have been observed to reach the water surface, and Nimmo-Smith et al. [1999] present evidence that dispersion of materials due to currents is greater than dispersion due to Langmuir circulation when the water speed is greater than $\sim 2\%$ of the wind speed. In an unstratified laboratory open-channel flow, *Hurther et al.* [2007] found that vertical turbulent transport (**Figure 1**) of turbulent kinetic energy (TKE) due to large coherent stress structures generated in the wall layer controls turbulence at heights above 80% of the boundary layer height. Lastly, in many cases, stratification will be important, but can have complex effects due to its impact of damping turbulence but also accompanying and promoting enhanced shear on ebb tides – a recent estuarine study showed that stratification could reduce turbulence to well below wall-layer predictions during neaps, but increase it above those levels through local shear instability in the middle of the water column during spring tides [*Peters and Bokhorst, 2000*].

Our ability to observe and understand near-surface turbulence in natural water bodies has been limited by several factors, including: (1) the fact that it is often highly heterogeneous in space and time, (2) it can be too subtle to be measured by conventional instruments, (3) it is in a moving reference frame with tides and waves displacing the sea surface, and (4) the turbulent velocity fluctuations of interest are much smaller than surface

wave orbitals. Observations of turbulent mixing far from the bottom boundary have until recently required costly and labor-intensive instrumentation. Turbulence near the sea surface is also complicated by processes occurring at the air-water interface that are difficult to measure, such as wave breaking and heat fluxes.

A study was designed with the overriding goals of (1) studying the influence of water column and atmospheric processes on near-surface turbulence in an estuary, and (2) demonstrating a framework for making autonomous (long-term, continuous) measurements of these processes that capture the breadth of their heterogeneity. The study utilized surface- and bottom-based autonomous measurement platforms and a combination of small-scale and large-scale turbulent velocity measurements with acoustic velocity sensors, which are relatively insensitive to calibration drift and biofouling. A bottom-mounted acoustic Doppler current profiler (ADCP) was used for measuring velocity of the mean flow field and the larger turbulent motions. An acoustic Doppler velocimeter (ADV) on an anchored catamaran was used for observing small-scale motions relevant to the TKE dissipation near the sea surface, and separating these motions from wave velocities through spectral analysis.

This paper begins with a review of aspects of the TKE budget, and then describes the measurement campaign on the Hudson River estuary that included acoustic velocity and turbulence observations, as well as detailed meteorological measurements, full water column density timeseries, spatial density transects, and estimates of the net air-sea heat flux. The forcing of TKE dissipation at 50 cm depth (ϵ_{50}) is examined from the air- and water-side through regressions and dynamical analyses. Additionally, the drivers of near-surface ϵ are examined from a different perspective, by quantifying the sources and sinks in

the TKE budget for periods when winds are below 3 m s^{-1} . The paper concludes by considering the indirect role of factors that can influence stratification such as tidal straining or surface heat fluxes.

2. Background

The most common way that turbulence is generated in the coastal ocean is when kinetic energy of the mean flow is converted into turbulent kinetic energy (TKE) by shear-driven instabilities. This energy flux from the mean flow field (e.g. \bar{u}) to the turbulent flow field (e.g. u') is referred to as shear production of TKE (P). A turbulent cascade has been theoretically and observationally shown to exist, where turbulent vortices interact and larger ones split into successively smaller ones. The vortices become smaller and smaller until they reach the scale at which they dissipate into heat due to molecular viscosity. The scales over which this occurs is called the inertial subrange, which spans the scale of the large eddies, roughly the scale of the shear layer depth, down to the scale of the smallest eddies where molecular viscosity causes dissipation.

This energy flux from turbulent kinetic energy to heat is known as TKE dissipation (ϵ). TKE dissipation has been studied widely not only because it is important for turbulence energetics, but also for interdisciplinary reasons. It is valuable for understanding turbulent constituent fluxes, since these fluxes are roughly proportional to ϵ [Rippeth *et al.*, 2005]. It also is a useful variable for studying biological oceanography, because small-scale turbulence plays an important role in many of the life processes of many planktonic organisms (e.g. food, nutrient or predator encounters).

If waters are vertically stratified with differing densities, not all turbulent kinetic energy that is produced runs through the turbulent cascade and is converted to heat. Instead, a small percentage of the TKE is expended in mixing water of differing densities, moving denser water upward and lighter water downward. This process, termed buoyancy destruction, increases the potential energy of the water column, so the TKE has been converted to potential energy, and energy is still conserved. Typically in the stratified portion of the water column, 5-20% of the TKE from shear production is expended through a buoyancy flux, and the remainder through dissipation [*Peters, 1999*]. Buoyancy destruction has an important negative counterpart, however – processes such as evaporation or surface cooling can cause water to become negatively buoyant, and the convective movement of this water to a more stable position is a buoyancy flux. This positive buoyancy flux can also be a source of TKE, a process often referred to as buoyancy production.

2.1 The turbulent kinetic energy budget

Assuming horizontal spatial uniformity and a negligible vertical mean velocity, the TKE budget is:

$$\frac{\partial TKE}{\partial t} = P + B - \varepsilon + T_D + T_p \quad (1)$$

Here, the time-derivative of TKE (k) per unit mass is on the left-hand side, where $TKE = \frac{1}{2}(\overline{u'^2} + \overline{v'^2} + \overline{w'^2})$, where bars are time averages and primes are perturbations from the mean. TKE shear production is $P = -\overline{u'w'}\partial U/\partial z - \overline{v'w'}\partial V/\partial z$, U, V, and W, and u', v', and w' are mean and turbulent velocities from a Reynolds decomposition, buoyancy

production is $B = -(g/\rho_0)\overline{w'\rho'}$, the dissipation rate of TKE is ε , the TKE transport due to turbulent pressure fluctuations (T_p) is typically considered to be negligible, and the net turbulent vertical transport of TKE is the divergence of the vertical turbulent flux of TKE, $T_D = \partial/\partial z(\overline{-w'TKE})$.

Order of magnitude estimates of T_D and $\partial TKE/\partial t$ in the ocean interior are similar to P and ε on short timescales (seconds to minutes), but much smaller when averaged over longer timescales [Tennekes and Lumley, 1972]. As a result, T_D and $\partial TKE/\partial t$ are often assumed to be negligible over the long averaging or time-step periods in observational and modeling studies of turbulent mixing. Two-equation turbulent models (e.g. Mellor-Yamada, k- ε , k- ω) are utilized widely for ocean circulation or coastal ocean numerical modeling, and typically represent the terms T_D and T_p jointly using a gradient diffusion model [Warner *et al.*, 2005].

3. Methods

3.1 Field Experiments

The Hudson River has a micro- to meso-tidal estuary, dominant semi-diurnal tide, and a mean river input of $430 \text{ m}^3 \text{ s}^{-1}$ from the upper watershed north of Troy (1984-2008 average). The estuary and study area are shown in **Figure 2**. The brackish section of the estuary is typically 45-110 km long, yet with typical peak velocities of $\sim 1 \text{ m s}^{-1}$ (**Chapter 2**), the tidal excursion during a flood or ebb tide is only $\sim 10 \text{ km}$. The region of the estuary from Piermont Pier to Indian Point has been studied less than the narrower, more channelized region to the south. The study area is 3.6 km wide, has relatively low ship traffic and is ideal for studying a range of estuarine processes such as interacting wind-,

wave-, and tide-forced currents, as well as deep channel (15 m depth) and shallow shoal (3-6 m depth) estuarine flows.

An experiment referred to as CASSIE (Carbon and Air-Sea Interaction in an Estuary), was conducted at a 5 m deep shoal site along a broad region of the Hudson River estuary (**Figure 2**). The shoal site was chosen near the center of the estuarine cross-section to have a large fetch in either direction, and several miles north of the Tappan Zee Bridge, to avoid contamination of air-sea CO₂ exchange measurements. A small Self-Orienting Catamaran (SOCa; **Chapter 3**) was anchored at this site over the period 23 September - 2 November, 2007 (year-days 265-303), to provide a surface-based view of turbulence, wind and air-sea heat fluxes. Nearby, a bottom-mounted 1200 kHz acoustic Doppler current profiler (ADCP) measured vertical profiles of velocity, acoustic backscatter, and several turbulence parameters over year-days 261-286 (see below). TRDI's rapid sampling mode-12 was used to record one ensemble average every second, an average of 21 sub-pings that were collected over 0.63 s (30 ms intervals). The vertical cell size was 0.25 m, and the resulting manufacturer estimate of velocity standard error for each ensemble average is 2.7 cm s⁻¹. Four 12-hour anchor stations and a few truncated ones (by foul weather), two along- and four across-channel transects were also conducted with a small boat and CTD profiling to observe density stratification (locations in **Figure 2**). A CTD was attached to the ADCP frame, and temperature probes along the SOCa anchor line, for continuous time series measurements. A meteorological station was set up at Piermont Pier (**Figure 2**), 8 km to the south, and these data were used to validate and supplement the SOCa datasets. Piermont measurements included solar radiation, which helped estimate the net water-to-air heat flux (**Section 3.6**).

The Self-Orienting Catamaran (SOCa) is an innovative platform useful for studying near-surface physical oceanography and air-sea interaction, with the name reflecting the fact that its keel rotates the vessel's instrumented boom into the current, so that measurements are never made in the wake. SOCa held an acoustic Doppler velocimeter (ADV) to measure near-surface currents and turbulent kinetic energy dissipation at 0.5 m depth, a sonic anemometer for wind velocity and temperature measurements at 1.2 m height, an inertial sensor to monitor platform motion, a water temperature probe at 0.5 m depth, and Licor LI-840 sensors for measuring CO₂ and H₂O concentrations and air-sea CO₂ fluxes. Single-height measurements of wind velocity, temperature and humidity, along with water velocity and temperature were used to compute bulk air-sea gradients, which were used with the COARE 3.0 bulk flux toolbox in Matlab [Fairall *et al.*, 2003] to estimate momentum and heat fluxes, wind stress, and the effective neutral wind velocity at 10 m height (U_{10N}). A detailed summary of the instrument platform and evaluation of its measurements during CASsIE is given in **Chapter 3**.

An additional 15 m depth "channel site" ADCP dataset from a 2004 deployment 7.5 km to the south (**Figure 2**) is utilized in this study for contrast against spring tide turbulence observed at the 5 m deep CASsIE shoal site. In 101 days of data collection, ensemble averages were recorded at 0.5 Hz, with vertical cell sizes of 0.5 m and standard error of 1.5 cm s⁻¹. These data are described in greater detail in **Chapter 2**.

A moderately wide range of ambient conditions was covered during CASsIE (**Figure 3**). The period had ranges in 10-minute averages of neutral equivalent 10 m height wind from 0 to 14.4 m s⁻¹, water depth from 4.7 to 6.2 m, surface water speed from 0 to 0.80 m s⁻¹, air temperature from 6 to 32 °C, water temperature from 17 to 25 °C, water salinity from

4 to 14, stratification from 0 to 4 kg m^{-4} , and significant wave height from 0 to $\sim 0.5 \text{ m}$. Daily-mean Hudson freshwater input from the upper watershed varied from 80 to $760 \text{ m}^3 \text{ s}^{-1}$ (measured at Green Island), corresponding to a range from mild drought conditions through most of the study to a moderately high flow rate just prior to the end of the period. This resulted in near-bottom salinities of 9-16 through most of the study, but dropping as low as 3.7 for the last few days. The estimated net water-to-air heat flux ranged from -710 to 620 W m^{-2} , corresponding to a range from warm sunny days to very cold dry-air mornings with surface waters $12 \text{ }^\circ\text{C}$ warmer than the overlying air (methods described in **Section 3.6**).

3.2 Acoustic data processing

ADCP and ADV velocity data were bin-averaged in 10 minute intervals. ADCP data were rotated from the earth reference frame into the direction of maximum near-bed velocity variance, to an along-stream (x) and across-stream (y) orthogonal reference frame. Data from the upper 6-8% of the water column were omitted, a standard procedure required because of acoustic side-lobe reflections off the sea surface, so velocity data is available from 1.25 m above the bed to $\sim 0.3 \text{ m}$ below the sea surface. ADV velocity data collected aboard SOCa are already oriented into the along-stream and across-stream directions for the surface current, due to the platform self-orienting capability (**Chapter 3**).

3.3 Dissipation estimates from ADV data

The Inertial Dissipation Method (IDM) is a well-validated technique has been used for decades to estimate the rate of dissipation of turbulent kinetic energy (ε) in a fluid flow [e.g., *Grant et al.*, 1961; *Voulgaris and Trowbridge*, 1998; *Zappa et al.*, 2003]:

$$\varepsilon = \Phi_i^{3/2} \kappa_i^{5/2} \alpha_i^{-3/2} \quad (2)$$

Here, dissipation is a function of angular wavenumber (κ_i) and the spatial power spectral density (Φ_i) of velocity over the "inertial subrange" of wavenumbers, index i refers to either the along-stream ($i=1$), across-stream (2) or vertical velocity (3). The constant α_i is 0.51 if the along-stream velocity is used to compute Φ_i , whereas it is 0.68 if the across-stream or vertical velocity is used.

Mean dissipation estimates were computed from spectra for 10-minute periods of the ADV's axial velocity data, which typically exhibits the lowest noise levels [*Voulgaris and Trowbridge*, 1998]. Taylor's frozen turbulence hypothesis was utilized to convert from the measured temporal spectrum to the spatial spectrum Φ_i required above. Dissipation and 95% confidence intervals were computed using an approach we refer to as the Kolmogorov + Noise (K+N) approach that subtracts off a white noise floor from the spectrum while computing dissipation (**Chapter 3**). This approach was particularly useful in this study, in which relatively noisy ADV data were collected using the highest velocity range setting on the instrument. Maximum wavenumbers used to compute ε correspond to the smallest water motions that could be measured by each sensor without substantial bias due to spatial or temporal averaging. Given the ADV spatial averaging lengthscale of 0.009 m, the maximum wavenumber was 240 rad m^{-1} . Minimum wavenumbers were chosen to be above

the wave mode to avoid wave bias in the dissipation estimate, which was determined from the pitch angular rate data measured by the vessel's inertial sensor (**Chapter 3**).

Strict quality control procedures were applied to omit periods that were not consistent with the K+N approach (a poor model-data fit), or wavy periods not consistent with Taylor's assumption. This included masking periods with estimated wave orbital velocities above 40% of mean velocity. Only 3% of the ϵ data were below $5 \times 10^{-8} \text{ W kg}^{-1}$, but these were set to 5×10^{-8} , which is an estimate of the noise floor on the ADV dissipation measurement with this velocity range setting. While these data have high uncertainty, low values of dissipation are as important to keep as high values, to avoid biasing averages or regressions (**Chapter 3**).

ADV estimates of ϵ were compared with estimates from a pulse-coherent Doppler current profiler (a 2 MHz Nortek Aquadopp) on SOCa, for a spring flood tide with light winds (up to 3.2 m s^{-1}) similar to the periods used for compiling TKE budgets in this paper. The ADV relies on Taylor's frozen field assumption, but the Aquadopp measures the spatial velocity profile at 2.7 cm resolution (and 4 Hz), and does not require this assumption. Pulse-coherent Doppler profilers have been used previously to estimate near-surface ϵ in wavy conditions from a moving surface platform [*Gemmrich and Farmer, 2004*] and in the laboratory [*Veron and Melville, 1999*]. Dissipation computations for the Aquadopp used spectra for the along-stream velocities (an acoustic beam aimed forward at 50 cm depth from the front of SOCa), and was performed on each 1.02 m length profile, with spectra averaged over 10-minute periods. The comparison showed moderate agreement over two orders of magnitude, from $\sim 9 \times 10^{-8}$ to $8 \times 10^{-6} \text{ W kg}^{-1}$, but the Aquadopp estimates were a factor of 1.1-2.5 higher for the highest turbulence levels, and

results were more scattered at low turbulence levels. Differences may arise due to the different range of wavenumbers used for IDM with the two instruments, from 60-80 rad m^{-1} for the Aquadopp and from 80-250 rad m^{-1} for the ADV. Given the range of two orders of magnitude in the measured ε during the comparison, and other sources of uncertainty in dissipation measurements, the level of agreement of this comparison is encouraging and lends support to the ADV ε estimates during low winds during this study.

3.4 TKE budget terms from ADCP data: P , B , T_D , $\partial TKE/\partial t$

Acoustic Doppler current profilers (ADCPs) are useful for measuring velocity of both the mean flow field and the larger turbulent motions over monthly or longer timescales. Janus configuration four-beam ADCPs sample along-beam velocity (b_i) with two pairs of opposing beams angled at angle θ from vertical, where the subscript indicates a measurement at a numbered beam path ($i = 1, 2, 3, 4$). Accounting for the beam angles, beam velocities may be related to velocities in an orthogonal reference frame, u , v , and w , assuming that the velocities are homogeneous across the beam width.

The four acoustic beams diverge to sample water parcels that are increasingly far apart, with increasing distance from the transducer. The larger this distance, the greater the spatial averaging of u , v , w , if the along-beam velocity data are transformed to an orthogonal velocity frame. This spatial averaging prevents accurate turbulence measurements, except in cases where the turbulent eddy scale is much larger than the spatial averaging scale. That is, in order to make an unbiased “direct computation” of Reynolds stress with ADCP orthogonal velocities, the flow velocities must be homogeneous across the distance between beams.

The ADCP variance method avoids this bias, providing the vertical Reynolds stresses $-\overline{u'w'}$ and $-\overline{v'w'}$ directly from the beam angle and variances of the along-beam velocity data. This computation only assumes that the ADCP is perfectly level and motionless and the second statistical moments (e.g. $\overline{u'^2}$, $\overline{u'w'}$) are horizontally homogeneous between beams [Lu and Lueck, 1999; Stacey et al., 1999]:

$$-\overline{u'w'} = \frac{\left(\overline{b_2'^2} - \overline{b_1'^2}\right)}{4 \sin \theta \cos \theta}, \quad -\overline{v'w'} = \frac{\left(\overline{b_4'^2} - \overline{b_3'^2}\right)}{4 \sin \theta \cos \theta} \quad (3)$$

Kinetic energy in the mean flow is continually converted into small-scale turbulence, an energy flux measured by our ADCP as turbulent kinetic energy production (P). This is computed directly from these stresses and the shear:

$$P = -\overline{u'w'} \partial U / \partial z - \overline{v'w'} \partial V / \partial z \quad (4)$$

For cases where waters are vertically stratified with differing densities, some TKE rearranges parcels of denser water above less dense water, increasing the potential energy of the water column. A method for estimating this buoyancy flux when P is available is to assume a constant value or model for the fraction of buoyancy flux relative to the dissipation, which is referred to as the flux Richardson number, R_f [Peters, 1999]:

$$B = -R_i f * P \quad (5)$$

Considering that vertical profiles of density are not available for all periods, we simply assume an R_f of 0.2, a typical ceiling value for stratified waters [Ivey and Imberger, 1991]. This term is typically at least a factor of four smaller than the P and ϵ terms [e.g., Peters, 1999], and the uncertainty of this assumption for periods with variable stratification will be taken into consideration when interpreting the results.

Along-beam velocity variances may also be used to observe TKE, first computing the quantity [Lu *et al.*, 2000; Stacey *et al.*, 1999]:

$$Q = \frac{1}{4 \sin^2 \theta} \left(\overline{b_1'^2} + \overline{b_2'^2} + \overline{b_3'^2} + \overline{b_4'^2} - 4D \right) \quad (6)$$

Here, D is a bias due to Doppler noise. Doppler noise levels (D) are often assumed to be zero, but may have some variability due to the availability of waterborne particles for sound scattering [Lu *et al.*, 2000]. The TKE per unit mass is:

$$\text{TKE} = 0.5 * Q / \gamma, \text{ where } \gamma = (1 + 2\alpha \tan^2 \theta) / (1 + \alpha) \quad (7)$$

Here, α is the anisotropy, $\overline{w'^2} / (\overline{u'^2} + \overline{v'^2})$, γ ranges from 1-2.7, corresponding to α from 0 to 0.5, from extremely anisotropic turbulence and isotropic turbulence, respectively [Lu *et al.*, 2000]. The TKE budget (Eq. 1) contains the time variation of TKE, $\partial \text{TKE} / \partial t$, computed by differencing successive 10-minute averages of TKE.

A technique for observing the turbulent vertical flux of TKE was recently developed and validated in the near-bed region of a bottom boundary layer by Stacey [Stacey, 2003], utilizing a sum of the third-order moments of along-beam velocity b_i :

$$K_3 = -\left(\overline{b_1'^3} + \overline{b_2'^3} + \overline{b_3'^3} + \overline{b_4'^3} \right) \quad (8)$$

This observed quantity contains information on the contribution of velocity along each beam axis to the flux, and accounting for the geometry of a Janus ADCP with 20-degree beam angles (default for a T-RDI ADCP), the vertical turbulent flux of TKE is [Stacey, 2003]:

$$F_D = -\overline{w' \text{TKE}} = \frac{1}{2} K_3 \frac{1 + A_n}{0.6595 + 3.3191 A_n} \quad (9)$$

This requires an estimate of an anisotropy factor defined as:

$$A_n = \frac{\overline{w'^3}}{\overline{w'u'^2 + w'v'^2}} \quad (10)$$

This is the ratio of contributions to TKE vertical turbulent transport from vertical versus horizontal TKE, and has been estimated to vary from 0.5 for isotropic bottom boundary layers to 1.5 for stratified, low-shear regions [Stacey, 2003].

Finally, to return to the term of import to the TKE budget, the net turbulent transport, or vertical flux divergence of F_D is:

$$T_D = \frac{\partial}{\partial z} \left(- \overline{w'TKE} \right) = \frac{\partial}{\partial z} F_D \quad (11)$$

Single 10-minute averages of T_D are noisy, so bin-averaging of large quantities of data from similar phases of the tidal cycle is required [Stacey, 2003].

3.5 ADCP turbulence data quality control

Potential sources of substantial bias in ADCP turbulence estimates include: instrument tilts, tilts with waves, and averaging in the vertical or temporal domain. An ADCP tilt of just 2° results in a bias of up to 17% in stress and shear production [Lu and Lueck, 1999]. Tilts for the CASsIE dataset were ~ 0.6 degrees, so tilt-bias should be negligible. Avoidance of biases related to waves is of particular importance due to our interest in near-surface turbulence, especially given the large wind fetch at the CASsIE site in the Hudson. Wave-filtration approaches have recently been presented, but generally risk biasing results because of additional assumptions on eddy scales or turbulence spectral shapes. In this paper, we focus on ADCP processing and the TKE budget for periods without waves (winds below 3 m s^{-1}), instead of taking on this additional complication. As an additional approach to avoid wave-bias in turbulent quantities (beyond limiting our

analyses to low-wind periods), we found it necessary to use the coherence between each acoustic beam's estimate of sea surface height (h_i) estimate and raw along-beam velocity (b_i) to omit entire profiles of turbulence data when near-surface bins have potential for wave bias (**Chapter 2**).

A comparison of low and high-resolution datasets is typically used to estimate the low-bias in stress due to averaging in time and space [e.g., *Lu et al.*, 2000]. The temporal averaging is over the period where raw samples (subpings) are taken, with a simple bin average of equal weighting. The effective vertical averaging is similar to a triangular filter of data and covers as much as two times the cell size (50% overlap). However, only ~16% of the weighting comes from outside the depth cell [*Pulkinen*, 1993], so the depth cell size is a good estimate of the vertical averaging lengthscale. Resolution bias correction factors were estimated by comparing turbulence estimates for the measured resolution and a coarser resolution dataset where neighboring samples were averaged in time (e.g. **Chapter 2**). The spring tide deep channel ADCP resolution bias correction factor for τ_{xz} (or P) was 1.21, and for F_D (or T_D) was 1.13. The spring tide shallow shoal ADCP correction factors were 1.22 and 2.24, respectively, likely higher due to the shallower water and smaller turbulent lengthscales, as well as weaker turbulence.

3.6 Surface heat flux estimates

The net upward surface heat flux (Q_{net}) was estimated as a sum of latent, sensible, solar shortwave, and longwave fluxes. Solar absorption was assumed to occur within the water column, not at the bed, because minimum turbidity levels during calm wind and tide conditions with low riverflow are typically 15-20 mg L^{-1} [e.g., *Orton and Kineke*, 2001]

suggesting a minimum light extinction coefficient of ~ 1.5 - 2.0 , so that 90% of light is typically attenuated in the upper 1-2 m [Cloern, 1987]. This is consistent with CASsIE observations during sunny, calm periods, when water temperature increases were mainly in the upper meter, and were negligible below 2 m (**Chapter 5**). The net longwave flux was estimated using the bulk formulae of Clark *et al.* [1974], which are shown to perform better in midlatitudes than other parameterizations and have low mean bias when compared with extensive observations [Josey *et al.*, 1997]. Daily mean cloud cover were estimated from the solar radiation data [Reed, 1977]. Net water-to-air surface heat fluxes ranged from -710 to 620 W m^{-2} (**Figure 3**), with specific components of the flux having the following ranges: solar -814 to 0 W m^{-2} , latent -40 to 370 W m^{-2} , longwave 5 to 189 W m^{-2} , and sensible -50 to 140 W m^{-2} .

The solar shortwave flux was measured, but the other budget terms were estimated using measured variables in bulk formulae, so it is useful to examine an overnight heat budget to evaluate their accuracy. A useful period for this test is from year-day 284.75 to 285.22, a period with strong heat loss when mean water column salinity change and velocity were near zero, suggesting that effects of advection on the budget should be negligible. The estimated Q_{net} was 504 W m^{-2} , and a simple heat budget suggests that this was accurate – the measured depth-averaged water column temperature decrease was $0.91 \text{ }^{\circ}\text{C}$, and if it is assumed that the air-water heat flux is the dominant controlling factor, this requires an average 463 W m^{-2} heat flux, 9% below the estimated value.

In spite of using bulk flux estimates of heat and momentum (wind stress), our approach utilizing *in situ* measurements from SOCa constitutes a significant improvement beyond many prior studies. Observational studies often use remotely-measured wind,

humidity and temperature to compute air-water fluxes (e.g. at an airport or offshore buoy), and this can lead to factor of two errors due to strong spatial variability in coastal regions (**Chapter 5**). Future studies should improve on our approach with either direct eddy covariance or atmospheric profile based flux estimates [McGillis *et al.*, 2001], the latter method of which has been used on subsequent deployments of the catamaran. Longwave radiation measurements are also possible with off-the-shelf products.

3.7 Additional derived quantities

A continuous wavelet transform (CWT) was used to quantify tidal forcing, decomposing observed water level data measured by the CTD on the ADCP tripod into semi-diurnal (D2) and diurnal (D1) species. This provides D2 tidal ranges (**Figure 3**) and also the D2 tidal current phase that is utilized below for tidal phase bin-averaged data presentations. The fundamental benefit of the CWT over traditional harmonic analysis is that it resolves the time-variation of frequency content, with no assumption of stationarity [Jay and Flinchem, 1999].

Bed stress (τ_b) was computed using linear regressions toward the bed of the bottom five stress measurements in the water column (**Chapter 2**), and the bottom shear velocity is $u_* = \sqrt{\tau_b / \rho}$ where ρ is water density. The water-side shear velocity (U_*) due to wind was computed using this equation with the bulk estimates of wind stress. For timeseries of u_* , this often led to undefined values on neaps or near slack tides because stress estimates were noisy and near zero. To produce a more continuous dataset for use in regressions or turbulent buoyancy flux computations, a drag coefficient of 0.0014 was used with the near

bed velocity (1.25 m height) and a quadratic drag law to compute u_* , giving good agreement with the regression estimates of u_* .

The gradient Richardson number (Ri) is a non-dimensional number useful for diagnosing the dynamic stability of the water column, with values below 0.25 typically indicating potential for instability [Geyer and Smith, 1987]. Ri was computed using the observed squared buoyancy frequency ($N^2 = g/\rho_0 \partial\rho/\partial x$) from 25 cm bins of CTD data, divided by 30-second averages of mean squared shear. We define the bottom boundary layer (δ_{bbf}) as the continuously turbulent range of heights above the bed, capped by either (a) a zero intercept (stress) in a regression of near-bed stress versus height, or (b) the first height where turbulent stress is not detected (**Chapter 2**).

4. Results

Neap-spring variability typically expected for a partially mixed estuary was observed at the 5 m deep shoal site in the time series and 12-hour anchor station data. The neap-spring cycle had a strong impact on near-bed salinity (**Figure 3**) and stratification, with peak stratification of 4 and 0.8 kg m^{-4} on weak neap and strong spring tides, respectively. Most tidal cycles exhibited periodic stratification (e.g. **Figure 4**), with the duration of well-mixed conditions (if any) typically depending on the strength of the tide.

Semi-diurnal phase relationships of stratification and velocity were typically similar to those expected for a lateral shoal [Scully *et al.*, 2009], with substantial differences relative to typical deep channel circulation patterns. One example of a 12-hour tidal cycle anchor station dataset that was collected four days past a strong spring tide is shown in **Figure 4**. The strongest pulse of saline water and stratification typically arrived late in

flood tide, likely due to bottom Ekman forcing causing cross-channel impingement of the salt wedge onto the shallow west side of the estuary [Scully *et al.*, 2009].

There were also signs of strong atmospheric effects on water column stratification during the CASsIE study at the shoal site. Temperature was frequently an important contributor to the full water column vertical density gradient, with temperature contributing 30% or more to the gradient in 25% of the timeseries profiles at the shoal site, predominantly in the warm-weather period early in the study. A 12-hour CTD timeseries on year-day 276 showed the effects of solar heating on a sunny afternoon with calm winds, with temperature enhancing upper water column stratification (from 0.5-1.5 m depth) by 50-100%, relative to salinity stratification alone (**Chapter 5**). Fall-season storms were also observed by SOCa, with mean along-estuary winds as high as 11.0 m s^{-1} (1.2 m height) gusting as high as 19 m s^{-1} (e.g. year-days 273.5-275.0 and 299.8-300.2), and were typically followed by periods of reduced stratification.

The deep channel site typically exhibits stronger stratification, with minima and maxima about three days past neap and spring tides, respectively. For along-channel water density transects typical of spring and neap conditions, as well as a complete climatology of stratification in the estuary, the reader is referred to **Chapter 2**. The two along-channel CTD transects are not presented here, but showed that the large-scale along-estuary density gradient ($\partial\rho/\partial x$) measured from stations to the north and south of the study site (**Figure 2**) were $-7.6 \times 10^{-5} \text{ kg m}^{-4}$ on 9/13//2007 and $-9.8 \times 10^{-5} \text{ kg m}^{-4}$ on 11/1/07.

Ebb tides during CASsIE had stronger near-surface currents and turbulence than floods, regardless of neap-spring phase (**Figure 5**). TKE shear production for the period shown in **Figure 4** was as high as $3 \times 10^{-5} \text{ W kg}^{-1}$, but the ADCP only detected shear

production in the upper half of the water column near peak flood and ebb. Surface-based SOCa estimates of TKE dissipation data at 50 cm depth during this period varied from $\sim 1 \times 10^{-7}$ to $7 \times 10^{-4} \text{ W kg}^{-1}$. Net turbulent transport is not shown because it requires additional averaging, but is presented below in **Section 4.2**, along with broader comparisons of P , $\partial \text{TKE} / \partial t$ and ϵ_{50} .

Levels of near-surface TKE dissipation (ϵ_{50}) are potentially related to several different variables, including winds, proximity or outcropping of the bottom boundary layer, near-surface TKE shear production, water speed or gradient Richardson number. The highest ϵ_{50} estimates of $2 \times 10^{-5} \text{ W kg}^{-1}$ in **Figure 4** were during ebb tide, at year-day 274.36. This period exhibited the tidal cycle's maximal near-surface water speed (50 cm s^{-1}) and shear production ($\sim 10^{-5} \text{ W kg}^{-1}$), as well as 3 m s^{-1} winds, and BBL turbulence extending from the bed to near the sea surface. Flood tide had relatively low ϵ_{50} values until yearday 274.62, when it rapidly increased, again coincident with increases in many of the same variables. Below, we attempt to determine relationships between these variables and ϵ_{50} by using regression analyses, quantifying the TKE budget, and examining possible dynamical explanations.

4.1 Near-surface dissipation observations and regressions

Wind speed clearly had a strong influence on ϵ_{50} during the study (**Figure 6**), but the wall layer model ($\epsilon = U_*^3 / 0.4z$) underestimated ϵ_{50} for most cases, suggesting additional processes beyond simple wind-generated shear instabilities were leading to higher turbulence levels. A log-log least-squares regression using U_*^3 shows significant correlation ($\alpha < 0.001$) and can account for 41% of the variance in ϵ_{50} (**Table 1**). Note that a

conservative approach is used to assess the significance of correlations using the effective degrees of freedom, the number of independent "events" that contribute to the correlation, defined as $edof = N/N_{ccv}$, where N_{ccv} is the number of lags over which the cross-covariance function rolls off by 50%.

Tidal currents and bottom boundary layer growth to the water surface appear to only have had a weak influence on ϵ_{50} . Evaluating the bottom wall layer dissipation scaling of $\epsilon_{50} \sim u_*^3$, the log of u_*^3 could explain only 10% of the variance in the log of ϵ_{50} . In cases where δ_{bb1} approached the sea surface, the median increase in dissipation over the 30 minutes before to after the time of reaching the surface was a factor of 2.00, though in a few cases it was an order of magnitude.

Variables related to turbulence generation by shear instability showed weak-to-moderate correlations with dissipation. A linear least-squares regression using surface water speed shows significant correlation with $\log_{10}\epsilon_{50}$ ($r^2=0.30$; $\alpha=0.02$) when using cases where wind speed was below 3 m s^{-1} (**Table 1**). A significant correlation is also present between surface water speed and $\log_{10}\epsilon_{50}$ when using all data ($r^2=0.14$; $\alpha=0.01$). While there was no correlation for surface water shear, the negative correlation for the log of near-surface gradient Richardson number (Ri_{surf}) was low-to-moderate ($r^2=0.18$). Ri_{surf} data was only available for the anchor station time series, so were fewer in number than any other variable used in the regression analysis ($N=78$), resulting in very low edof (8) and marginal significance ($\alpha=0.30$) in spite of the correlation (**Table 1**).

Variables related to air-sea heat fluxes had moderate correlations with dissipation, suggesting possible causative relationships (e.g. **Figure 7**). There was a significant positive correlation ($r^2=0.17$, $\alpha=0.06$) between the net air-sea heat flux (Q_{net}) and $\log_{10}\epsilon_{50}$. There is

a slightly stronger positive correlation ($r^2=0.22$) for periods of heat loss from water to atmosphere ($Q_{\text{net}}>0$), and no correlation during periods with heat gain into the water such as sunny and/or hot, windy afternoons ($Q_{\text{net}}<0$).

4.2 Near-surface TKE budgets

Near-surface TKE budgets are examined here, focusing on low-wind spring tide cases where lengthscales are relatively large and the signal-to-noise ratio is relatively good. Spring ebbs in the Hudson have been shown to have the strongest TKE dissipation [*Peters, 1999*], and account for a large percentage of the vertical salt flux over fortnightly spring-neap tidal periods [*Nepf and Geyer, 1996*]. Profiles of velocity, turbulence lengthscales, and TKE budget terms are shown in **Figures 8-10**, for the shoal and channel sites. The shoal site budgets utilize additional data from 2006 at the same site, using the same ADCP settings, to improve the signal to noise ratio. Consistent with predictions of *Stacey (2003)*, a large number of profiles must be averaged to reduce observational uncertainty for T_D . The average lengthscales and TKE parameters presented here are averages of 60-100 10-minute average profiles, so 3600-6000 ensemble averages of velocity (each an average of over 10 individual “sub-ping” measurements).

A theoretical vertical lengthscale for the turbulence expected to dominate energetically is the Ellison scale, which has been shown to be triple the Prandtl scale of $L_m = (\overline{u'w'})^{0.5} (\partial \bar{u} / \partial z)^{-1}$ [*Stacey et al., 1999*]. However, the open channel flow lengthscale imposed by the proximity of the seabed and surface, $L_{\text{OCF}} = 0.4z (1-z/h)^{0.5}$ [*Simpson et al., 1996*], would limit the scales as shown in **Figure 9**. Lengthscales during spring tides were

well above the vertical cell size of 25 cm, though only by a factor of 2-3 during shoal spring floods.

The shoal TKE budget for strong spring ebbs (**Figure 10**; top left) is closed to within their uncertainty levels, with a close similarity between ε_{50} ($5.2 \times 10^{-6} \text{ W kg}^{-1}$) and P at 60 cm depth (4.2×10^{-6}). Ebb near-surface P and ε_{50} were approximately equal to values predicted for that height by the bed wall layer model, $\varepsilon = u_*^3 / 0.4z$, while flood P and ε_{50} were much smaller ($10^{-6} \text{ W kg}^{-1}$ or lower). Signal-to-noise levels for shoal floods, however, were too low to quantify the budget.

The deep channel TKE budget terms (**Figure 10**) similarly show near-surface turbulence on ebbs is similar to the wall-layer model, and flood near-surface turbulence is weak. On floods, T_D approaches the magnitude of P in the upper water column, but both are substantially lower than the ebb P values.

The mean of absolute value of the TKE tendency term, $|\partial \text{TKE} / \partial t|$, is plotted in **Figure 10**, and was typically well below $10^{-6} \text{ W kg}^{-1}$. TKE measurements with Eq. 7 require subtraction of the noise floor (D) in Eq. 6, but $\partial \text{TKE} / \partial t$ should not be sensitive to this correction because time dependence of D is low – prior studies have found that D at a given height above the bed was relatively constant with time [Lu *et al.*, 2000; Stacey *et al.*, 1999].

5. Discussion

Here, we compare our results to a prior study of TKE dissipation in the Hudson, then assess the dominant drivers of near-surface dissipation in the Hudson, reflecting in general on characteristics of partially mixed or salt wedge estuaries. Wind stress generation of

turbulence clearly is dominant, but we also examine the relative importance of bed stress versus shear instability, the roles of ebb and flood tidal dynamics, and impacts on water column stratification of buoyancy fluxes due to tidal straining, turbulent mixing, and surface heat fluxes.

Several days of measurements of turbulence from near the bed to the upper water column along the deep channel of the lower Hudson (alongside Manhattan) showed the importance of stratification and local shear instability outside the bed log layer [*Peters, 1999; Peters and Bokhorst, 2000*]. They observed strong turbulence in the bottom boundary layer, weak turbulence in and above the pycnocline during neap tides, and low Ri and high ϵ through the water column during spring ebbs. Turbulence in the stratified water column well above the bottom appeared to be locally generated by shear instability, and was $10^{-5} \text{ W kg}^{-1}$ on spring ebbs, well above levels predicted by the wall layer dissipation model. That study did not include measurements above ~ 2.5 m depth, or address wind-generation, or include overnight observations, so our study provides a unique dataset for addressing some of the same but also some different processes.

5.1 Wind stress generation of turbulence

It is well-established that winds can influence upper ocean turbulence, though studies of direct wind generation of turbulence in estuaries are somewhat rare. Turbulence can be generated directly through shear (e.g. wall layer model), through wave breaking [*Gemmrich and Farmer, 2004*], and through interactions of shear and waves such as Langmuir cells [e.g., *Gargett and Wells, 2007*]. It has also been shown that along-channel

winds can modify stratification and indirectly strengthen or weaken turbulence through wind straining [*Chen and Sanford, 2009; Scully et al., 2005*].

The study was conducted at a broad, straight section of the Hudson and thus wind is expected to have a strong influence on near-surface turbulence, particularly for along-channel winds. The cross-channel fetch is ~ 1.8 km in each direction, and the along-channel fetch is over 14 kilometers to the north and much longer to the south. There is a significant correlation between the wind-driven shear velocity cubed (U_*^3) and ϵ_{50} in the CASsIE study (**Table 1**). This study does not examine details of the role of wave breaking, but rather focuses on periods with low-to-moderate winds where multiple processes may be important.

The fact that ϵ_{50} was above the wind-driven wall layer model can result from a number of processes superimposed on wind-driven shear, including those listed above. At wind speeds (U_{10N}) above ~ 5 m s⁻¹, wind wave breaking was typically observed, and likely explains ϵ_{50} above the wall layer model. At wind speeds below 5 m s⁻¹, dissipation above the wall layer prediction may result from superimposition of tide- and wind-driven currents; as described in **Section 3.3**, periods with weak currents were masked to avoid ϵ_{50} biases due to waves and Taylor's assumption. The good agreement between the spatial Aquadopp measurement and the temporal ADV estimates of ϵ_{50} for similarly low winds (**Section 3.3**) suggests that waves, vessel motion, and the use of Taylor's assumption were not causing biases for winds below 3.2 m s⁻¹.

5.2 Ebb dominance of near-surface dissipation

Near-surface turbulence was typically stronger on ebb tides than floods, at both the shoal and channel sites (**Figures 5, 10**). Spring flood tides had moderate currents but still had a low ϵ_{50} average, below $2 \times 10^{-6} \text{ W kg}^{-1}$ (**Figure 5**). Multiple processes exist that could cause differences in ϵ_{50} for flood versus ebb tides. One possible reason for stronger ebb turbulence is obvious from **Figure 4** – stronger tidal currents and shallower water depth lead to stronger shear. In shallow estuaries with a progressive tidal wave, the peak ebb velocity is near the time of minimum depth, and the peak flood near the time of maximum depth. For a given tidal volume transport, depth-averaged shear is weaker on flood tides.

The weaker ϵ_{50} and P on flood versus ebb tides can also be attributed to the dynamics of a partially stratified estuary. On ebbs, due to the opposition of barotropic (down-estuary and constant with depth) and baroclinic (up-estuary, maximal at the bed) pressure gradient forces, as well as due to differential advection of the along-channel salinity gradient (tidal straining), the entire water column has shear [*Stacey and Ralston, 2005*]. Shear instabilities and T_D during these periods can lead to relatively high ϵ_{50} (**Figure 10**). Alternatively, on flood tides, the alignment of these forces and the negative tidal straining buoyancy flux lead to a well-defined bottom boundary layer and pycnocline with maximum velocity (and zero shear) at the top [*Stacey and Ralston, 2005*]. In this case, since shear instability must be zero at this location, and shear is relatively weak above, near-surface ϵ_{50} is low. Also, T_D in the flood bottom boundary layer was typically observed to be toward the pycnocline from below, and weak above the pycnocline., similar to the initial observations using the ADCP third-moments method for observing T_D [*Stacey, 2003*]. During strong spring tides, the bottom boundary layer can reach the sea surface on flood tide, but at the sites observed

in this study, the resulting near-surface turbulence is much weaker than bottom wall layer predictions (**Figure 10**).

5.3 The role of bed stress versus local shear instability

A major goal of the research project was to study how strong tidal currents and a turbulent bottom boundary layer could cause strong near-surface turbulence. However, u_* (or bed stress) had only a weak correlation with ε_{50} , and there was only a median ε_{50} increase of 2.00 when the bottom boundary layer reached the sea surface (**Section 4.1**). Net turbulent transport of TKE (T_D) approached the same magnitude as P in the upper water column on flood tides at the channel station (**Figure 10**), but dropped toward the upper few meters. However, the magnitude was small relative to spring ebb P , and this likely points to the difference between rough bed, unstratified conditions where T_D is important [*Hurther et al.*, 2007] and relatively smooth-bed, frequently stratified estuaries such as the Hudson.

Due to the complex role of stratification, a simple parameterization for air-sea fluxes utilizing bed stress with a wall layer model [e.g., *Chu and Jirka*, 2003] or open channel flow model to represent tide-driven turbulence will generally not be accurate for a partially stratified (or salt wedge) estuary. Stratification can have complex effects due to its impact of damping turbulence but also accompanying and promoting enhanced shear on ebb tides, leading to local shear instability high in the water column (see prior section). Moreover, it is possible that increases in suspended mud during periods with high bed stress provide a negative feedback on turbulence, causing sediment-induced stratification and raising Ri , as can occur in the Hudson's turbidity maximum off Manhattan [*Orton and Kineke*, 2001].

Shear instability is typically the dominant turbulence generation mechanism in estuaries [*Geyer and Smith, 1987; Peters and Bokhorst, 2000*], whether near the bed or far from it. However, local shear instability in regions with strong shear high in the water column can produce strong turbulence near the surface. Surface water speed showed some correlation with ϵ_{50} , but mainly only at water speeds above 50 cm s^{-1} . For a given water speed on a neap tide, the dissipation is much lower than for the same water speed on a spring tide (**Figure 5**). This is likely because in partially stratified estuaries, outside of well-mixed flood tide bottom boundary layers, shear often accompanies stratification and the gradient Richardson number (Ri) is often near the critical value for shear instability, 0.25 [e.g., *Chant et al., 2007*]. The regression of Ri_{surf} and dissipation had moderate correlation ($r^2 = 0.18$) but too few independent events to be statistically significant (**Table 1**). While the variables should be related, a low Ri also doesn't necessarily require there to be substantial TKE and dissipation, so the lack of a stronger correlation is not surprising.

High values of ϵ_{50} from year-day 282.14-282.21 (**Figures 6-7**) appear to have been related to small-scale shear instability in the upper water column, as the ADCP shows strong shear and water speeds from $70\text{-}80 \text{ cm s}^{-1}$. However, ADCP estimates of P and the Ellison turbulent lengthscale were near zero during this period, likely due to turbulence lengthscales being smaller than the ADCP vertical averaging lengthscale of 25 cm. No CTD profile data were collected at this time, but observations during an ebb tide on the following day showed strong stratification (up to 2.5 kg m^{-4}). The Ozmidov scale is a theoretical lengthscale for the largest eddy that can occur in a stratified flow, $L_O = \epsilon^{0.5} N^{-3/2}$, and equals 0.14 m for this stratification and logarithmic mean ϵ_{50} of $7.8 \times 10^{-5} \text{ W kg}^{-1}$, so it is reasonable that the ADCP would not detect this episode.

5.4 Buoyancy flux impacts on upper water column stratification

Processes that govern water column stratification can indirectly impact turbulence generation, and are typically examined in terms of depth-integrated buoyancy fluxes in W kg^{-1} [Stacey *et al.*, 2001; Stacey and Ralston, 2005] or the temporal change of the vertical potential energy anomaly in W m^{-3} [Simpson *et al.*, 1990]. Here, we estimate and compare buoyancy fluxes due to wind- and tide-driven turbulent vertical mixing, spatial transport (tidal straining), and the surface heat flux, seeking dynamical clues to view alongside our observed correlations and budgeting results. Similar results are found when comparing contributions of each term to the vertical potential energy anomaly. Wind straining [e.g., Scully *et al.*, 2005] is not considered – the Wedderburn number had almost no correlation with ϵ_{50} , likely because wind-driven mixing increases in importance as you near the sea surface.

The estimated surface net heat flux (Q_{net}) provides a water column buoyancy flux in the upper layer, using the convention here of positive flux for a gain in water buoyancy [Imberger, 1985]:

$$B_{\text{surface}} = -Q_{\text{net}}\alpha g/c_p\rho \quad (12)$$

Here, we have incorporated the heat capacity (c_p) and thermal expansion coefficient (α) for water.

Turbulent buoyancy fluxes due to both tide-driven ($B_{\text{turb,tide}}$) and wind-driven ($B_{\text{turb,wind}}$) turbulent mixing were approximated using the negative of wall-layer scaling of P and the flux Richardson number (Eq. 5). The total turbulent buoyancy flux from wind and tides could alternately be estimated using observed shear production levels, but wavy periods have been omitted from the ADCP turbulence dataset, so this makes it impossible

to quantify mixing for all periods. A rough estimate of upper water column buoyancy destruction due to wind-driven turbulent mixing at 1 m depth was made using the wall-layer scaling. The along-channel buoyancy flux due to tidal straining on the shoal was approximated using the scaling of Stacey and Ralston [2005], $B_{\text{shear}} = g/\rho_0 (\partial\rho/\partial x) \Delta u \delta_{\text{bbl}}$, with a constant $\partial\rho/\partial x \approx 1 \times 10^{-4} \text{ kg m}^{-4}$ based on the observed values (**Section 4**). Here, the velocity difference scale used for shear is $\Delta u = 2u^*/0.4$, a scale for the difference between the mean bottom boundary layer speed and the water speed just above the top of the layer.

Resulting time series of each buoyancy flux are shown with upper water column stratification data in **Figure 11**. During sunny periods with weak winds (e.g. left panel), buoyancy fluxes due to tidal processes and surface fluxes are of similar order. During a stormy period (right panel), the wind mixing term was dominant through much of the period, but the study's strongest surface cooling and surface buoyancy flux were observed overnight as the storm ended. In spite of similar tidal straining and turbulent buoyancy fluxes, the ebb on the sunny day (276) restratified the upper water column, whereas the ebb on the cold morning (285) did not, suggesting the large difference in surface heat flux was an important factor. A cross-channel transect on year-day 285 showed that the stormy period did not cause total estuarine de-stratification, so this was only a local shoal de-stratification event. Strong stratification of 1 kg m^{-4} returned on the ebb tide during the sunny afternoon of year-day 285.

5.5 Indirect impacts of heat flux on near-surface turbulence generation

The buoyancy flux analysis above, as well as the significant correlations between Q_{net} and ϵ_{50} suggest a possible role for air-sea heat fluxes in turbulence generation. Our

turbulence dataset is unusual in that it includes full diurnal cycles and stormy periods that help evaluate this role – most prior estuary studies with dissipation measurements have only sampled during the daytime and relatively calm conditions [e.g., *Peters and Bokhorst, 2000; Zappa et al., 2003*], and this highlights the utility of an autonomous turbulence sampling platform.

The mechanism for decreased turbulence during periods with a downward net heat flux (e.g. a negative Q_{net} , on a sunny warm day) is most likely enhanced temperature stratification, damping turbulence (e.g. **Figure 11**). As mentioned in **Section 4**, temperature was frequently an important contributor to the full water column vertical density gradient, and at times had the same importance as salinity in near-surface stratification, doubling stratification and the gradient Richardson number on some sunny afternoons (e.g. year-day 276; **Chapter 5**).

Possible mechanisms for enhanced turbulence due to surface cooling include penetrative convection, and increased shear instability due to reductions in stratification (prior section). In lakes, surface heat loss is an important factor for turbulence, with seasonal or diurnal convective overturning [*Imberger, 1985*]. Also, in detailed studies of the sea surface, it has been shown that skin layer recovery after a disturbance occurs more rapidly when there is an upward surface heat flux [*Zappa et al., 1998*]. The observed overnight mean 510 W m^{-2} heat flux only directly provides a buoyancy flux out of the upper water column of $B_{surface} = 3 \times 10^{-7} \text{ W kg}^{-1}$ (Eq. 12; **Figure 7**). This is the maximum buoyancy production of TKE that could occur, and thus puts a ceiling on the TKE dissipation resulting from convection. Additionally, a surface flux doesn't have any direct impact on the TKE budget unless the water becomes negatively buoyant to the degree that

gravitational forces can overcome viscous ones and buoyancy production can occur.

Therefore, the correlation between ε_{50} and Q_{net} does not appear to be a direct result of cooling-induced convection.

The highest ε_{50} values of the study were observed during a moderate ebb tide from year-day 285.14-285.31, in spite of mean northwest winds below 5 m s^{-1} . CTD profiling was performed manually on site from year-day 285.25 onward, showing weak stratification (**Figure 11**), and the ADV was verified to be working without obstruction. It is likely that the low stratification resulting from the storm was an important factor, and that processes related to forced convection at a density front or due to wind straining of a cross-estuary density gradient are likely to have provided the energy for the strong ε_{50} . Closer examination of short timescale ε ($\sim 30 \text{ s}$ averages), 2 Hz wind and temperature data, and 1 Hz ADCP velocity and backscatter profiles have so far been inconclusive, but it involved less than $\sim 1\%$ of the ε_{50} data and further analyses are beyond the scope of this paper.

The Chesapeake also exhibits a "temperature inversion" in fall, where temperature opposes the salinity stratification, and was observed to be directly responsible for a 20-25% decrease in stratification early in the fall season, priming the system for increased mixing during fall storms [Blumberg and Goodrich, 1990]. A model experiment adding and removing the temperature inversion found that the inversion was important in the completeness of estuary deep water mixing, as well as its abruptness, but not in the timing of the event [Blumberg and Goodrich, 1990].

It is likely that the correlation between Q_{net} and ε_{50} would be reduced during periods with larger freshwater inputs to the estuary such as the spring freshet, when along-estuary salinity gradients and larger and tidal straining is stronger. However, the observed heat

fluxes were not unusual for sunny weather or fall-season cooling events, and the along-estuary density gradient observed during the study was not unusual compared with prior observations in the Chesapeake [e.g., *Blumberg and Goodrich*, 1990; *Scully et al.*, 2005], Delaware Bay [*Chen and Sanford*, 2009], or San Francisco Bay [*Stacey et al.*, 2001; *Stacey and Ralston*, 2005].

6. Summary and conclusions

An experiment was performed on the Hudson River Estuary to study the influence of water column and atmospheric processes on near-surface turbulence, and to demonstrate a framework for making autonomous measurements of these processes. Analyses of the forcing of near-surface TKE dissipation (ϵ_{50}) from the air- and water-side suggest that wind is the primary driver of the turbulence, but significant positive correlations also exist for ϵ_{50} and surface water speed (u_{50}), as well as net upward air-sea heat flux (Q_{net}).

A weaker correlation was found between ϵ_{50} and bed stress, suggesting that simple bed stress wall layer or open channel flow models are not likely to be useful for predicting near-surface turbulence or gas exchange. This is because stratification in a partially mixed or salt wedge estuary can have complex effects due to its impact of damping turbulence but also accompanying and promoting enhanced shear on ebb tides, leading to local shear instability high in the water column.

Seeking a dynamical explanation for the positive correlation between ϵ_{50} and Q_{net} , processes controlling water column stratification on sunny days and stormy days were contrasted. Solar heat input and straining caused similar buoyancy fluxes and promoted ebb tide restratification on a sunny day. Wind-driven mixing dominated during a fall-season

storm event, but strong overnight heat loss after the storm appeared to help prevent restratification during an ebb tide afterward.

The near-surface TKE budget at a shallow shoal study site was closed for a strong spring ebb tides, but turbulence was weak and estimated TKE terms noisy for spring floods. Looking to spring tide data from a deep channel site for a better signal-to-noise ratio, a local TKE budget between P and ε was not valid in the upper half of the water column, because the turbulent TKE transport term is of a similar magnitude to P . However, both terms are small relative to spring tide ebb shear production values. Near-surface turbulence was generally stronger on ebb tides than floods, and this is related to the dynamics of partially mixed and salt wedge estuaries that lead to shear throughout the water column on ebbs, but low shear in the upper water column on floods. Shear production and upward turbulent transport of TKE during spring ebbs add TKE to the upper water column, whereas spring floods exhibit a well-defined bottom boundary layer and low shear production in the upper water column.

In an era where the influence of air-sea interaction processes on estuarine and coastal flows are increasingly being appreciated, improved observational tools must be utilized to measure wind-driven momentum fluxes, air-sea heat exchanges, and wind-driven mixing. The dual observation approach demonstrated in this study, with bottom profiler and surface catamaran based turbulence and air-sea exchange observations, provides the opportunity to collect detailed autonomous measurements of these processes. Future studies should improve on our approach with either direct eddy covariance or atmospheric profile based flux estimates of heat and momentum exchanges [McGillis *et al.*, 2001], the latter method of which has been used on subsequent deployments of the catamaran. A fully integrated

atmosphere-ocean measurement approach holds great promise for improving our understanding of the effects of atmospheric processes on near-surface turbulence across the coastal zone.

References

Blumberg, A., and D. Goodrich (1990), Modeling of wind-induced destratification in Chesapeake Bay, *Estuaries and Coasts*, 13(3), 236-249.

Chant, R. J., W. R. Geyer, R. Houghton, E. Hunter, and J. Lerczak (2007), Estuarine Boundary Layer Mixing Processes: Insights from Dye Experiments, *J. Phys. Oceanogr.*, 37(7), 1859-1877.

Chen, S.-N., and L. P. Sanford (2009), Axial Wind Effects on Stratification and Longitudinal Salt Transport in an Idealized, Partially Mixed Estuary, *J. Phys. Oceanogr.*, 39(8), 1905-1920.

Chu, C. R., and G. H. Jirka (2003), Wind and Stream Flow Induced Reaeration, *Journal of Environmental Engineering*, 129(12), 1129-1136.

Clark, N., L. Eber, R. Laurs, J. Renner, and J. Saur (1974), Heat exchange between ocean and atmosphere in the eastern North Pacific for 1961–71, *NOAA Tech. Rep. NMFS SSRF*, 682, 108.

Cloern, J. (1987), Turbidity as a control on phytoplankton biomass and productivity in estuaries, *Cont. Shelf Res.*, 7(11-12), 1367-1381.

Fairall, C. W., E. F. Bradley, J. E. Hare, A. A. Grachev, and J. B. Edson (2003), Bulk Parameterization of Air-Sea Fluxes: Updates and Verification for the COARE Algorithm, *J. Clim.*, 16(4), 571-591.

Gargett, A. E., and J. R. Wells (2007), Langmuir turbulence in shallow water. Part 1. Observations, *J. Fluid Mech.*, 576(-1), 27-61.

Gemmrich, J. R., and D. M. Farmer (2004), Near-surface turbulence in the presence of breaking waves, *J. Phys. Oceanogr.*, 34, 1067-1086.

- Geyer, W. R., and J. D. Smith (1987), Shear Instability in a Highly Stratified Estuary, *J. Phys. Oceanogr.*, *17*(10), 1668-1679.
- Grant, H. L., R. W. Stewart, and A. Moilliet (1961), Turbulence Spectra From a Tidal Channel, *J. Fluid Mech.*, *12*, 241-268.
- Hurther, D., U. Lemmin, and E. Terray (2007), Turbulent transport in the outer region of rough-wall open-channel flows: the contribution of large coherent shear stress structures (LC3S), *J. Fluid Mech.*, *574*(-1), 465-493.
- Imberger, J. (1985), The diurnal mixed layer, *Limnol. Oceanogr.*, *30*, 737-770.
- Ivey, G., and J. Imberger (1991), On the nature of turbulence in a stratified fluid. I, The energetics of mixing, *J. Phys. Oceanogr.*, *21*(5), 650-658.
- Jay, D. A., and E. P. Flinchem (1999), A comparison of methods for analysis of tidal records containing multi-scale non-tidal background energy, *Cont. Shelf Res.*, *19*(13), 1695-1732.
- Josey, S., D. Oakley, and R. Pascal (1997), On estimating the atmospheric longwave flux at the ocean surface from ship meteorological reports, *J. Geophys. Res.*, *102*(27), 961-927.
- Li, M., L. Zhong, and W. C. Boicourt (2005), Simulations of Chesapeake Bay estuary: Sensitivity to turbulence mixing parameterizations and comparison with observations, *J. Geophys. Res.*, *110*.
- Lu, Y., and R. G. Lueck (1999), Using a Broadband ADCP in a Tidal Channel. Part II: Turbulence, *J. Atmos. Oceanic Technol.*, *16*(11), 1568-1579.
- Lu, Y., R. G. Lueck, and D. Huang (2000), Turbulence Characteristics in a Tidal Channel, *Journal of Physical Oceanography*, *30*(5), 855-867.
- Malone, T. C. (1977), Environmental regulation of phytoplankton productivity in the lower Hudson Estuary, *Estuarine and Coastal Marine Science*, *5*(2), 157-171.
- McGillis, W. R., J. B. Edson, J. D. Ware, J. W. H. Dacey, J. E. Hare, C. W. Fairall, and R. Wanninkhof (2001), Carbon dioxide flux techniques performed during GasEx-98, *Mar. Chem.*, *75*, 267-280.

- Nepf, H. M., and W. R. Geyer (1996), Intratidal variations in stratification and mixing in the Hudson estuary, *J. Geophys. Res.*, *101*, 12079-12086.
- Nimmo-Smith, W. A. M., S. A. Thorpe, and A. Graham (1999), Surface effects of bottom-generated turbulence in a shallow tidal sea, *Nature*, *400*, 251-254.
- NOAA-NOS (2006), National Oceanographic and Atmospheric Administration, National Ocean Service data available at <http://spo.nos.noaa.gov/bathy/>.
- Orton, P., and G. Kineke (2001), Comparing calculated and observed vertical suspended-sediment distributions from a Hudson River Estuary turbidity maximum, *Estuarine, Coastal and Shelf Science*, *52*(3), 401-410.
- Peters, H. (1999), Spatial and temporal variability of turbulent mixing in an estuary, *J. Mar. Res.*, *57*, 805-845.
- Peters, H., and R. Bokhorst (2000), Microstructure observations of turbulent mixing in a partially mixed estuary. Part I: Dissipation rate, *J. Phys. Oceanogr.*, *30*, 1232-1244.
- Pulkkinen, K. (1993), Comparison of Different Bin-mapping Methods for a Bottom-mounted Acoustic Profiler, *J. Atmos. Oceanic Technol.*, *10*(3), 404-409.
- Reed, R. (1977), On estimating insolation over the ocean, *J. Phys. Oceanogr.*, *7*(3), 482-485.
- Rippeth, T. P., M. R. Palmer, J. H. Simpson, N. R. Fisher, and J. Sharples (2005), Thermocline mixing in summer stratified continental shelf seas, *Geophys. Res. Lett.*, *32*.
- Scully, M., C. Friedrichs, and J. Brubaker (2005), Control of estuarine stratification and mixing by wind-induced straining of the estuarine density field, *Estuaries and Coasts*, *28*(3), 321-326.
- Scully, M. E., W. R. Geyer, and J. A. Lerczak (2009), The Influence of Lateral Advection on the Residual Estuarine Circulation: A Numerical Modeling Study of the Hudson River Estuary, *Journal of Physical Oceanography*, *39*(1), 107-124.
- Simpson, J., J. Brown, J. Mathews, and G. Allen (1990), Tidal straining, density currents, and stirring in the control of estuarine stratification, *Estuaries*, *12*, 125-132.

Simpson, J., W. Crawford, T. Rippeth, A. Campbell, and J. Cheok (1996), The vertical structure of turbulent dissipation in shelf seas, *J. Phys. Oceanogr.*, 26(8), 1579-1590.

Souza, A. J., N. R. Fisher, J. H. Simpson, and M. J. Howarth (2008), Effects of tidal straining on the semidiurnal cycle of dissipation in the Rhine region of freshwater influence: Comparison of model and measurements, *J. Geophys. Res.*, 113.

Stacey, M. T., S. G. Monismith, and J. R. Burau (1999), Measurements of Reynolds stress profiles in unstratified tidal flow, *J. Geophys. Res.*, 104.

Stacey, M. T., J. R. Burau, and S. G. Monismith (2001), Creation of residual flows in a partially stratified estuary, *J. Geophys. Res.*, 106.

Stacey, M. T. (2003), Estimation of Diffusive Transport of Turbulent Kinetic Energy from Acoustic Doppler Current Profiler Data, *Journal of Atmospheric and Oceanic Technology*, 20(6), 927-935.

Stacey, M. T., and D. K. Ralston (2005), The Scaling and Structure of the Estuarine Bottom Boundary Layer, *J. Phys. Oceanogr.*, 35(1), 55-71.

Tennekes, H., and J. L. Lumley (1972), *A first course in turbulence*, MIT Press, Cambridge, MA.

Veron, F., and W. K. Melville (1999), Pulse-to-pulse coherent Doppler measurements of waves and turbulence, *J. Atmos. Ocean. Technol.*, 16, 1580-1597.

Voulgaris, G., and J. H. Trowbridge (1998), Evaluation of the acoustic- Doppler velocimeter (ADV) for turbulence measurements, *J. Atmos. Oceanic Technol.*, 15, 272-289.

Warner, J. C., W. R. Geyer, and J. A. Lerczak (2005), Numerical modeling of an estuary: A comprehensive skill assessment, *J. Geophys. Res.*, 110.

Zappa, C., W. McGillis, P. Raymond, J. Edson, E. Hints, H. Zemmeling, J. Dacey, and D. Ho (2007), Environmental turbulent mixing controls on air-water gas exchange in marine and aquatic systems, *Geophys. Res. Lett.*, 34(10), 10601.

Zappa, C. J., A. T. Jessup, and H. H. Yeh (1998), Skin-layer recovery of free-surface wakes: Relationship to surface renewal and dependence on heat flux and background turbulence, *J. Geophys. Res.*, *103*(C10), 21711–21722.

Zappa, C. J., P. A. Raymond, E. Terray, and W. R. McGillis (2003), Variation in surface turbulence and the gas transfer velocity over a tidal cycle in a macro-tidal estuary, *Estuaries*, *26*(6), 1401-1415.

Figure Captions

Figure 1: Conceptual diagram showing some of the processes that may influence upper water column turbulence in a partially mixed or salt wedge estuary. Vectors at the center show characteristic ebb tide (toward the left) and flood tide (toward the right) velocity profiles.

Figure 2: The Hudson River estuary (left) with a zoom-in to the 2007 CASsIE study site (right panel) with shaded NOAA-NOS [2006] bathymetry data. The Self-Orienting Catamaran (SOCa) was deployed at a mean depth of 5.1 m, 100 m south of the ADCP for the CASsIE study, and the meteorological (met) station was on Piermont Pier. Data from a 2004 ADCP deployment in 15 m depth water across from Piermont Pier is also used in this paper for comparison to the observed conditions during CASsIE.

Figure 3: Time series of ambient conditions during the 2007 CASsIE study. The periods where various systems were deployed are indicated as: (shaded) ADCP deployment, and (dashed vertical lines) SOCa catamaran deployment. Variables include (a) wind velocity vectors for Piermont (pointing in direction wind is coming from), (b) river flow past Green Island Dam near Troy, NY, (c) observed water level (η), with the envelope of observed semi-diurnal tidal range (from wavelet analysis) superimposed, (d) air (T_{air}) and water (T_{water}) temperatures, (e) estimated net upward surface heat flux, and (f) salinity measured on the ADCP tripod, at 30 cm above the bed.

Figure 4: Water and wind conditions during one 12-hour timeseries, four days after a strong spring tide. Shown are along-stream velocity (u), contours of water density anomaly (σ_t), TKE shear production, bottom boundary layer height (δ_{bb}), near-surface Richardson number (Ri_{surf}), TKE dissipation (ϵ) at 50 cm depth, wind speed, and wind speed in the direction of the water current. Times of CTD profiles are shown with external x-axis ticks in the upper panels.

Figure 5: Tidal phase bin-averaged (top) water velocity and (bottom) dissipation, for periods with low winds ($U_{1,2}$ below 3 m s^{-1}). The legend designates neaps (year-days 275-280 and 304-306) and strong spring tides (year-days 298-300). Errorbars show the 95% confidence intervals on the mean, assuming a log-normal distribution.

Figure 6: The relationship between wind speed and dissipation (50 cm depth), measured on SOCa. Dashed lines show the uncertainty range for the wall layer model for wind-generated turbulence within a factor of $\pm 33\%$ of an estimated quadratic drag coefficient of 0.0015. The squares and pluses are from two weak spring ebb tides that exhibited anomalously high dissipation, the squares with strong shear and currents (**Section 5.3**) and the pluses with strong heat fluxes and no stratification (**Section 5.5**).

Figure 7: The net air-sea heat flux (Q_{net}) and dissipation have a strong relationship, for low winds or all data. Points in black have wind speeds ($U_{1,2}$) below 3 m s^{-1} , while grey points have stronger winds. The dashed line shows the maximum ϵ that could result from free convection caused by surface cooling (i.e., 100% of the buoyancy loss is converted to TKE

buoyancy production). However, Q_{net} could also influence turbulence by promoting or destroying stratification, impacting the potential for shear instability. Squares and pluses are as in the prior figure.

Figure 8: Velocity profiles for periods used in the strong spring tide TKE budgets (**Figure 10**). The 60-100 10-minute average profiles are all superimposed, to show the typical velocity structure. Mean water column depths are (shoal) 5.1 m and (channel) 15 m.

Figure 9: Vertical turbulence lengthscales for the periods used in the strong spring tide TKE budgets (**Figure 10**). Shown are: Mean profiles of the estimated Ellison turbulence lengthscale (L_E) and the theoretical open-channel flow limit due to the bed and sea surface boundaries (L_{OCF}).

Figure 10: Mean TKE budget terms for strong spring tides with low winds – TKE shear production (P), net turbulent TKE flux (T_D), mean absolute value of TKE tendency ($\partial\text{TKE}/\partial t$), and dissipation at 50 cm depth (ϵ_{50}) from SOCa (shoal budget only). Observed standard error is shown as shading around T_D and P , and as a horizontal line for ϵ_{50} . For the shoal site, the near-surface TKE budget is quantified at ~ 50 cm depth as $\partial\text{TKE}/\partial t = P - 0.2P - \epsilon + T_D$ (**Section 4.2**). The bed wall layer model of P_{wall} is also shown for comparison.

Figure 11: Two timeseries of estimated upper water column buoyancy fluxes and stratification at the shoal site, showing processes that can indirectly impact turbulence by modifying stratification. Shown are the stratification over the upper two meters ($-\partial\rho/\partial z$)

measured with CTD profiles, and buoyancy fluxes due to: surface heat flux (B_{surface}), tidal straining (B_{shear}), tide-driven mixing ($B_{\text{turb,tide}}$), and wind-driven mixing ($B_{\text{turb,wind}}$). The period to the left was a sunny day with strong positive buoyancy fluxes and restratification during ebb (year-day 276.4), and the period to the right had a fall-season storm with wind-driven de-stratification, followed by strong overnight heat loss and no restratification on the morning ebb (year-day 285.2).

Table 1: Results of the correlation analysis for $\log_{10}\epsilon_{50}$, with significant results shaded ($\alpha \leq 0.10$)

Independent variable	variable name	r^2	N	edof^a	α^b	Details
$\log_{10}U_*^3$	surface turb. scale	0.41	538	54	<0.001	for all data
Q_{net}	sea-to-air heat flux	0.17	432	22	0.06	for all data
$\log_{10}u_*^3$	bed turb. scale	0.10	247	24	0.14	for all data
u_{surf}	water speed	0.14	506	50	0.01	for all data
u_{surf}	water speed	0.30	180	18	0.02	$U_{1,2} \leq 3 \text{ m s}^{-1}$
u_{surf}	water speed	0.02	342	34	>0.33	$2 < U_{1,2} \leq 5$
u_{surf}	water speed	0.03	50	5	>0.33	$5 < U_{1,2}$
$\log_{10}Ri_{\text{surf}}$	Richardson #	0.18	78	8	0.30	for all data
du_{surf}/dz	surface shear	0.00	380	38	--	for all data

a Effective degrees of freedom, $\text{edof} = N/N_{\text{ccv}}$, where N_{ccv} is the cross-covariance roll-off scale

b Significance test – α is the probability of a Type I error, false correlation by random chance

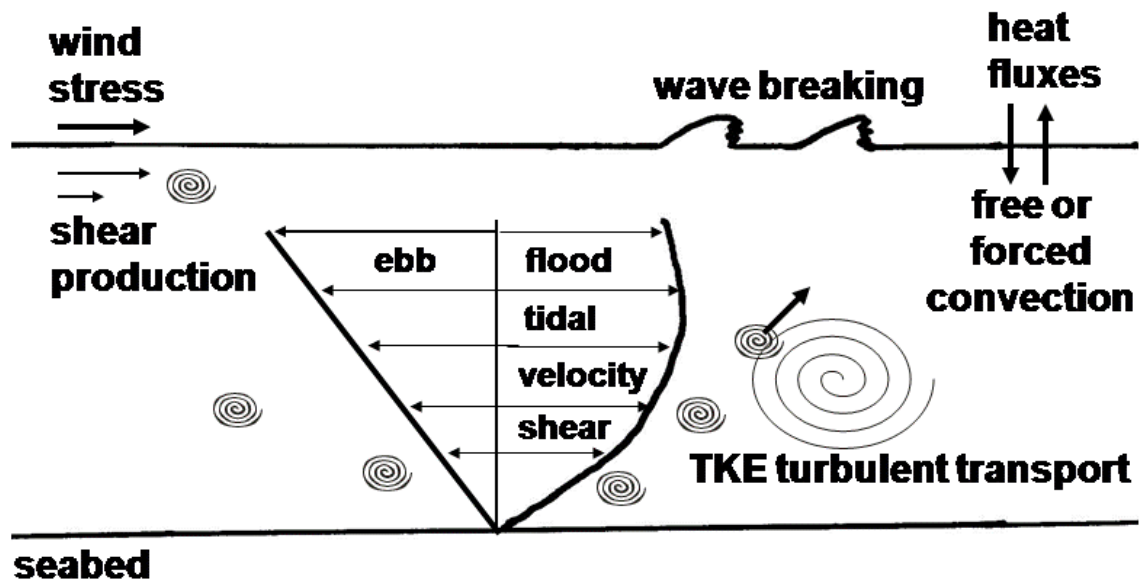


Figure 1: Conceptual diagram showing some of the processes that may influence upper water column turbulence in a partially mixed or salt wedge estuary. Vectors at the center show characteristic ebb tide (toward the left) and flood tide (toward the right) velocity profiles.

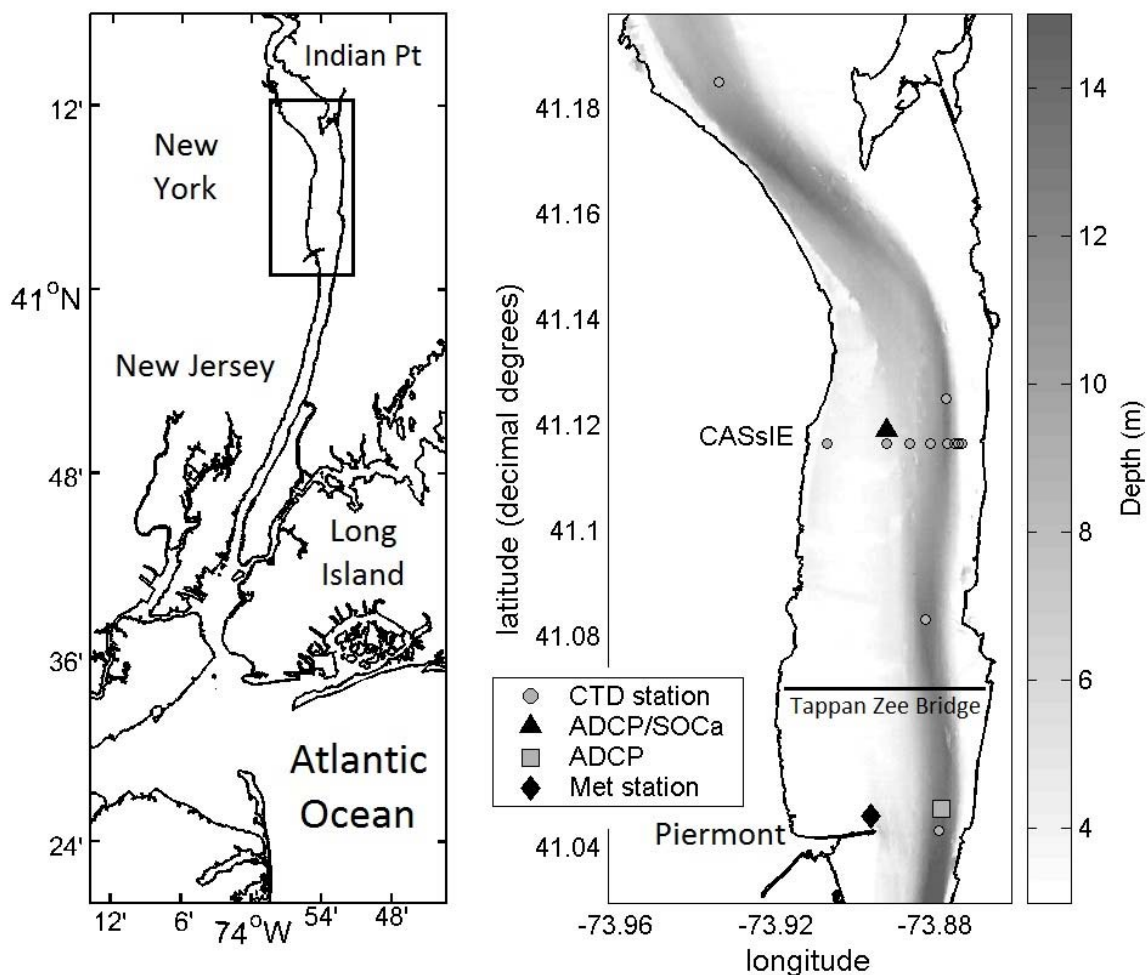


Figure 2: The Hudson River estuary (left) with a zoom-in to the 2007 CASsIE study site (right panel) with shaded NOAA-NOS [2006] bathymetry data. The Self-Orienting Catamaran (SOCa) was deployed at a mean depth of 5.1 m, 100 m south of the ADCP for the CASsIE study, and the meteorological (met) station was on Piermont Pier. Data from a 2004 ADCP deployment in 15 m depth water across from Piermont Pier is also used in this paper for comparison to the observed conditions during CASsIE.

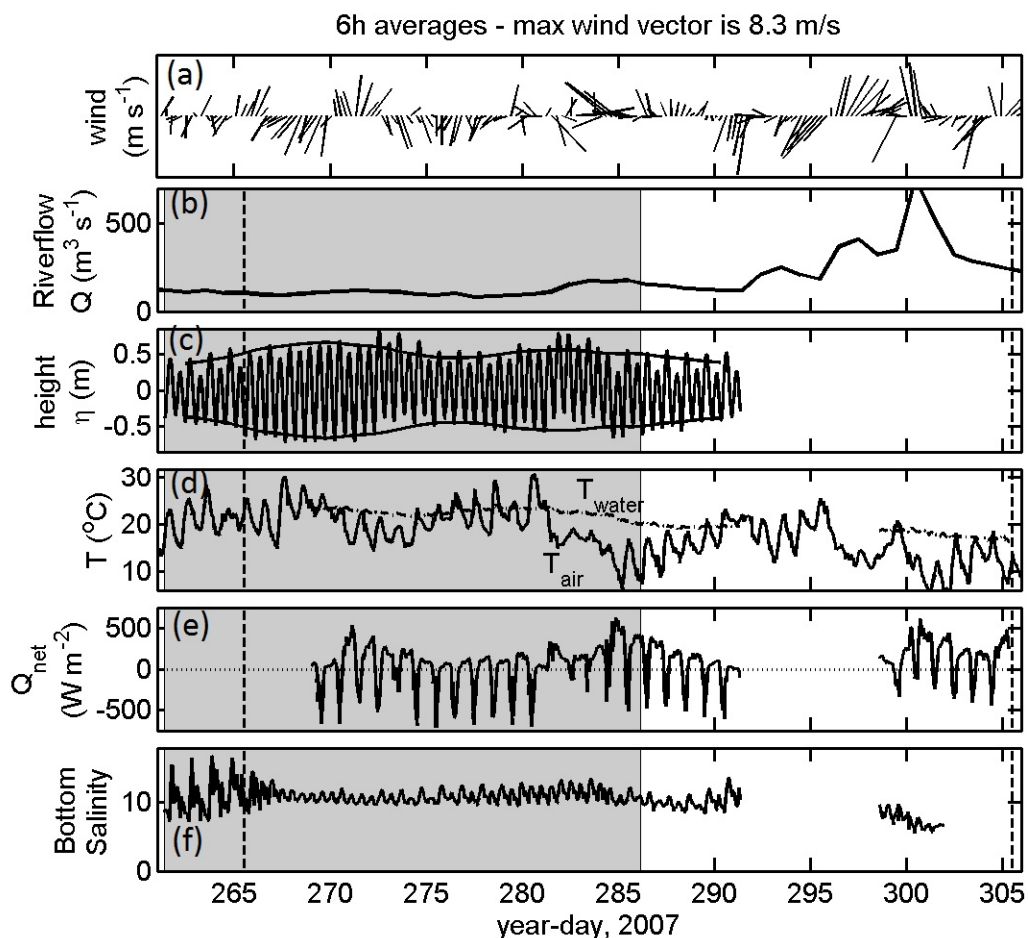


Figure 3: Time series of ambient conditions during the 2007 CASsIE study. The periods where various systems were deployed are indicated as: (shaded) ADCP deployment, and (dashed vertical lines) SOCa catamaran deployment. Variables include (a) wind velocity vectors for Piermont (pointing in direction wind is coming from), (b) river flow past Green Island Dam near Troy, NY, (c) observed water level (η), with the envelope of observed semi-diurnal tidal range (from wavelet analysis) superimposed, (d) air (T_{air}) and water (T_{water}) temperatures, (e) estimated net upward surface heat flux, and (f) salinity measured on the ADCP tripod, at 30 cm above the bed.

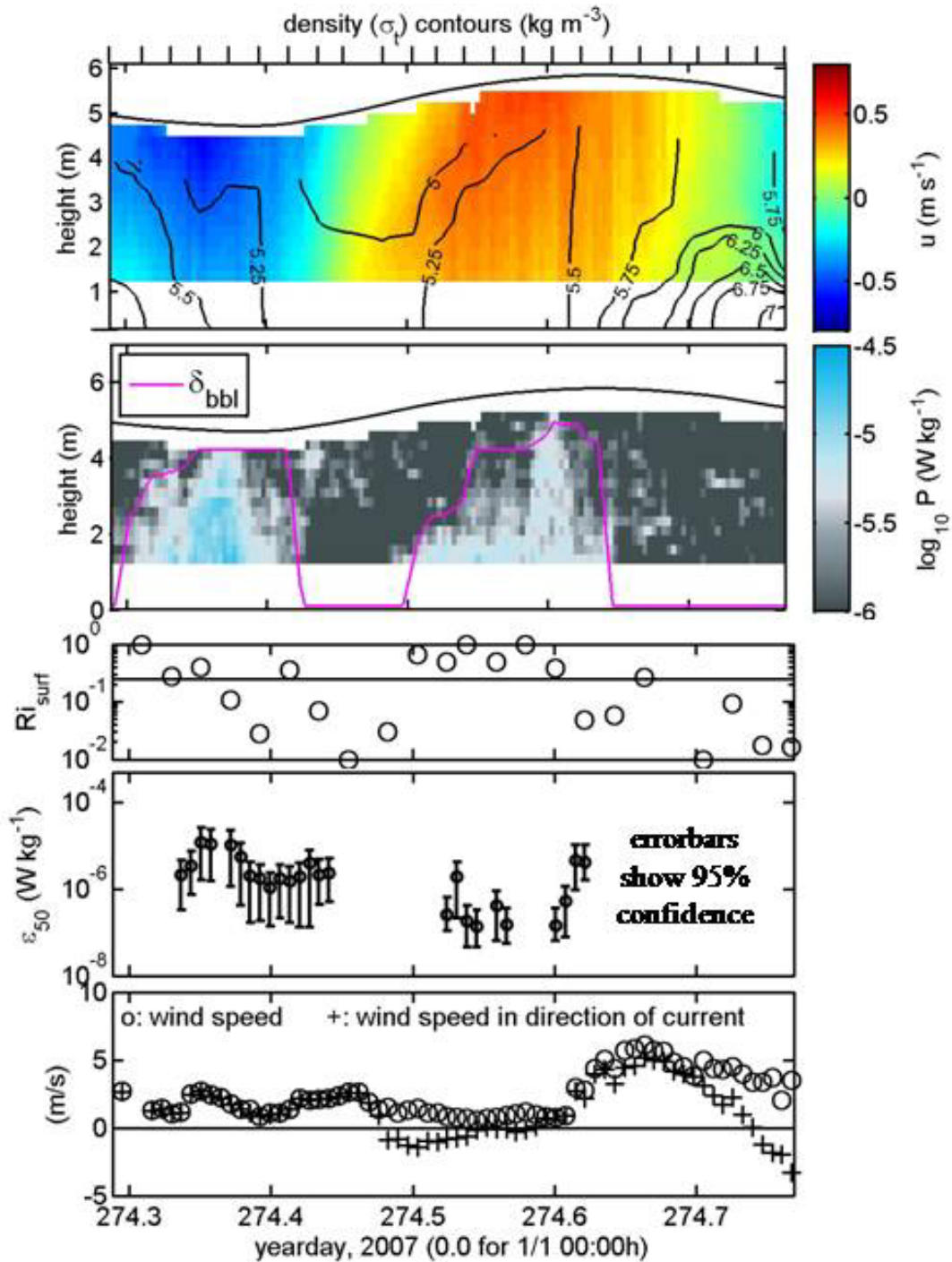


Figure 4: Water and wind conditions during one 12-hour timeseries, four days after a strong spring tide. Shown are along-stream velocity (u), contours of water density anomaly (σ_t), TKE shear production, bottom boundary layer height (δ_{bbl}), near-surface Richardson number (Ri_{surf}), TKE dissipation (ϵ) at 50 cm depth, wind speed, and wind speed in the direction of the water current. Times of CTD profiles are shown with external x-axis ticks in the upper panels.

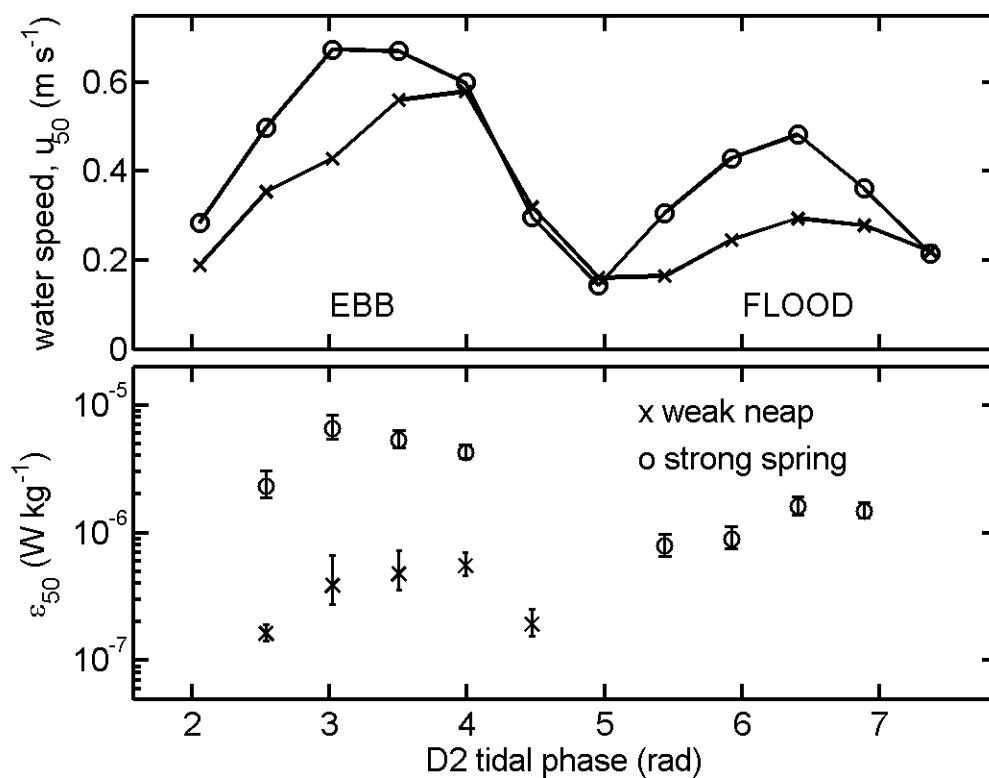


Figure 5: Tidal phase bin-averaged (top) water velocity and (bottom) dissipation, for periods with low winds ($U_{1.2}$ below 3 m s^{-1}). The legend designates neaps (yeardays 275-280 and 304-306) and strong spring tides (yeardays 298-300). Errorbars show the 95% confidence intervals on the mean, assuming a log-normal distribution. Only averages from periods with mean water speed above 0.3 m s^{-1} and more than five 10-minute averages are shown.

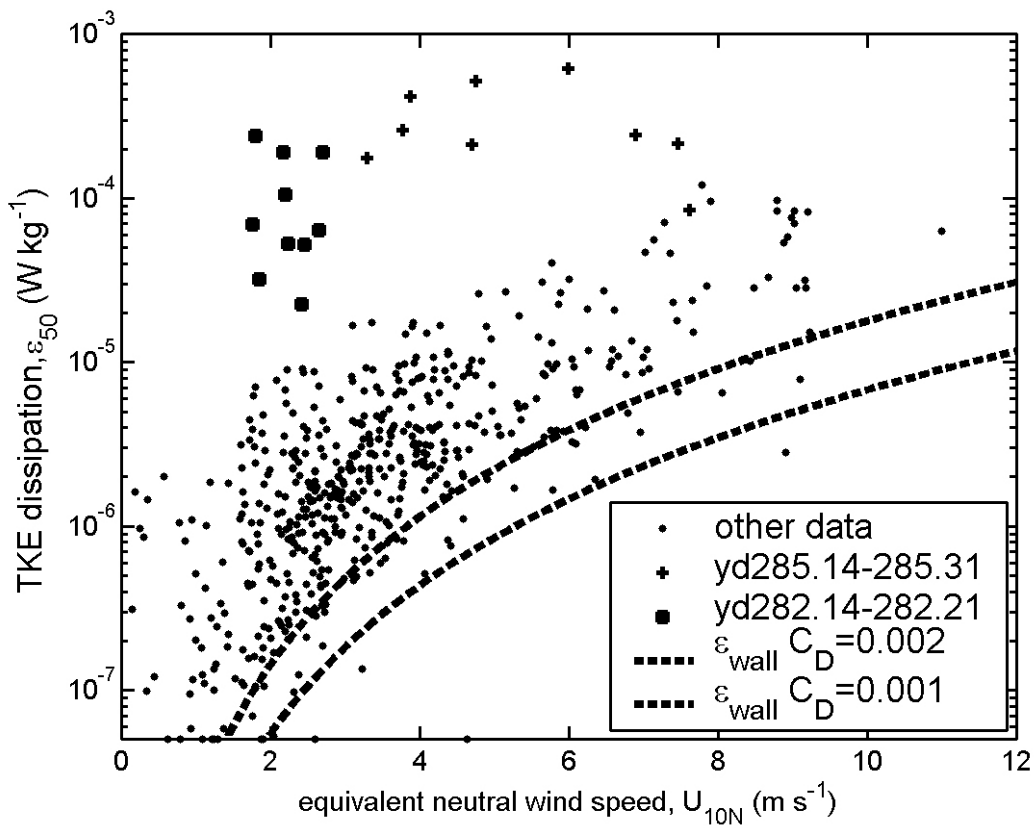


Figure 6: The relationship between wind speed and dissipation (50 cm depth), measured on SOCa. Dashed lines show the uncertainty range for the wall layer model for wind-generated turbulence within a factor of $\pm 33\%$ of an estimated quadratic drag coefficient of 0.0015. The squares and pluses are from two weak spring ebb tides that exhibited anomalously high dissipation, the squares with strong shear and currents (**Section 5.3**) and the pluses with strong heat fluxes and no stratification (**Section 5.5**).

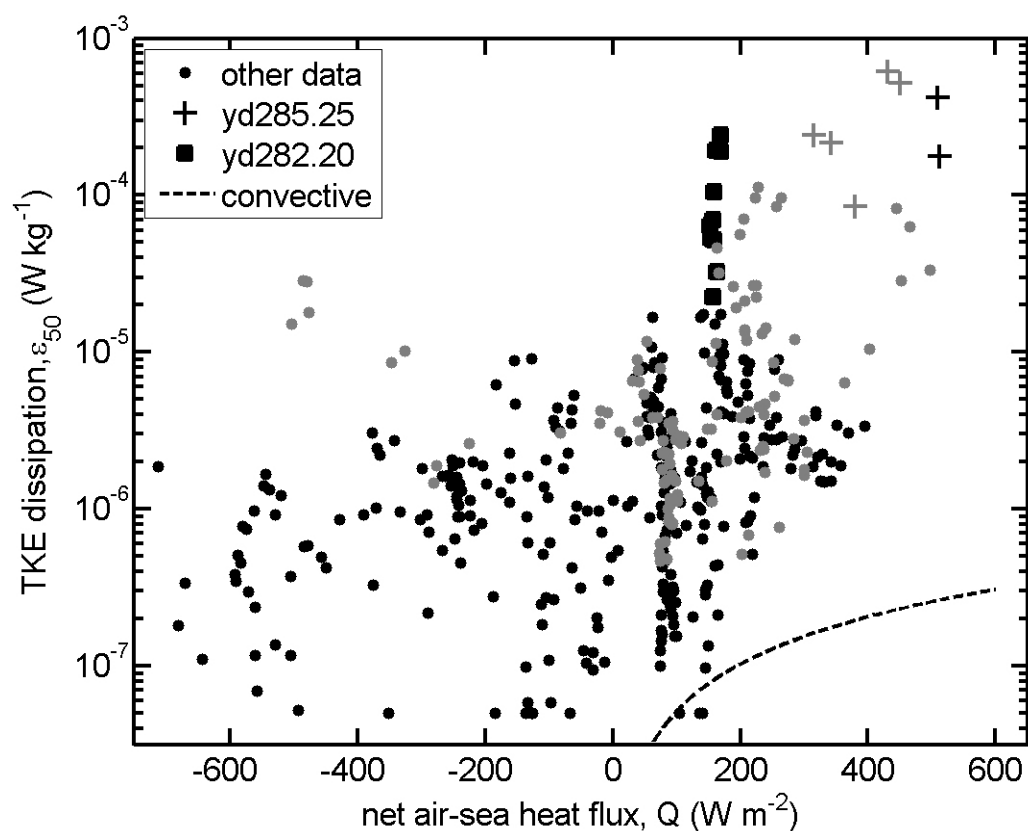


Figure 7: The net air-sea heat flux (Q_{net}) and dissipation have a strong relationship, for low winds or all data. Points in black have wind speeds ($U_{1,2}$) below 3 m s^{-1} , while grey points have stronger winds. The dashed line shows the maximum ε that could result from free convection caused by surface cooling (i.e., 100% of the buoyancy loss is converted to TKE buoyancy production). However, Q_{net} could also influence turbulence by promoting or destroying stratification, impacting the potential for shear instability. Squares and pluses are as in the prior figure.

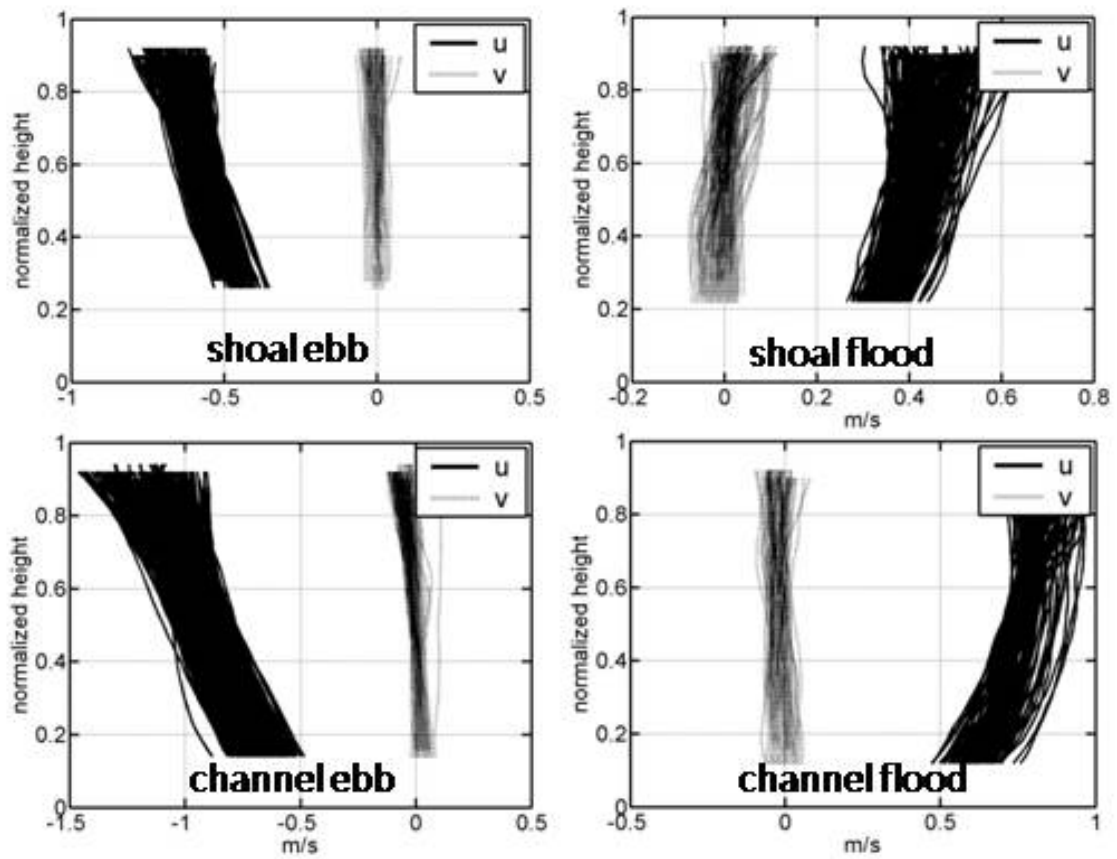


Figure 8: Velocity profiles for periods used in the strong spring tide TKE budgets (**Figure 10**). The 60-100 10-minute average profiles are all superimposed, to show the typical velocity structure. Mean water column depths are (shoal) 5.1 m and (channel) 15 m.

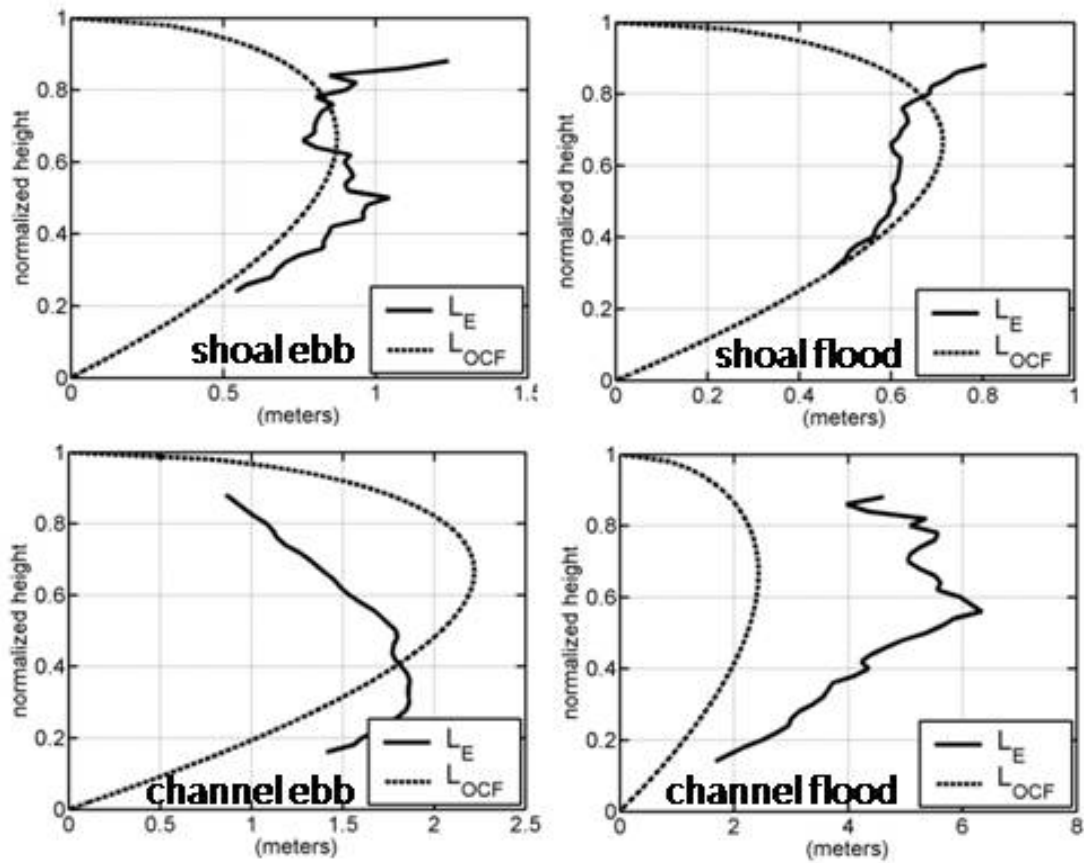


Figure 9: Vertical turbulence lengthscales for the periods used in the strong spring tide TKE budgets (**Figure 10**). Shown are: Mean profiles of the estimated Ellison turbulence lengthscale (L_E) and the theoretical open-channel flow limit due to the bed and sea surface boundaries (L_{OCF}).

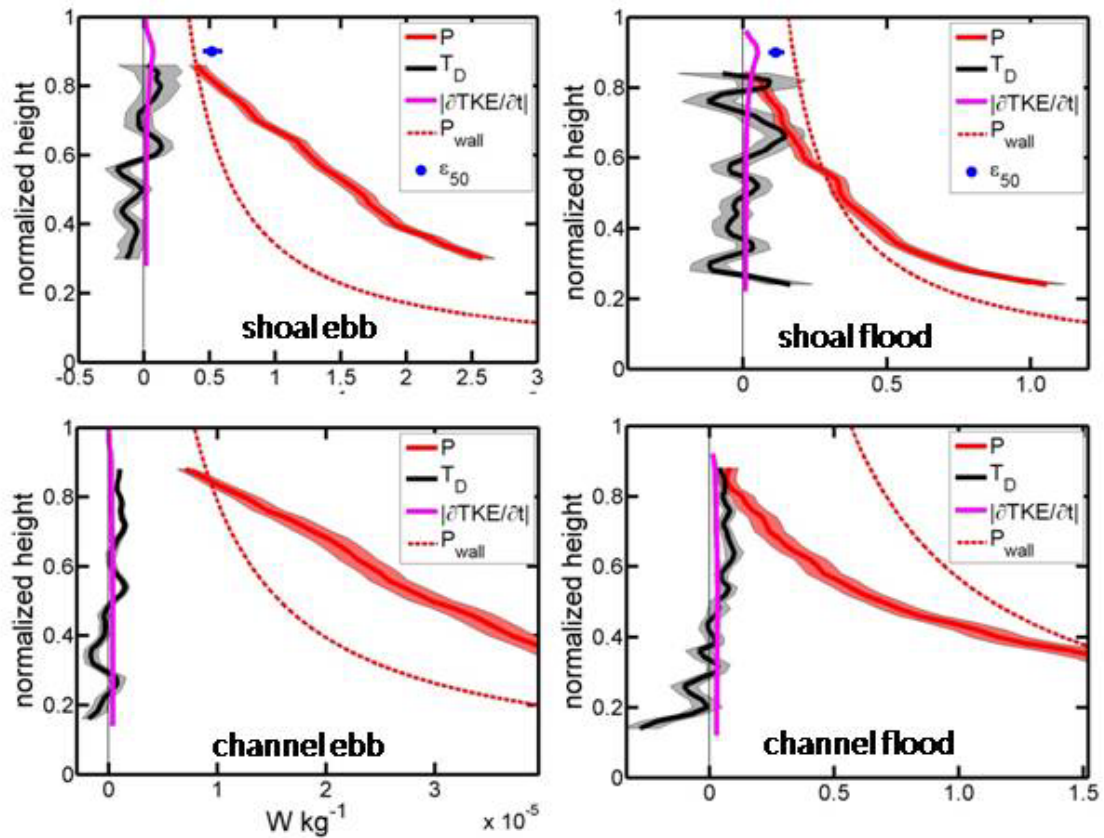


Figure 10: Mean TKE budget terms for strong spring tides with low winds – TKE shear production (P), net turbulent TKE flux (T_D), mean absolute value of TKE tendency ($|\partial TKE/\partial t|$), and dissipation at 50 cm depth (ε_{50}) from SOCa (shoal budget only). Observed standard error is shown as shading around T_D and P , and as a horizontal line for ε_{50} . For the shoal site, the near-surface TKE budget is quantified at ~ 50 cm depth as $\partial TKE/\partial t = P - 0.2P - \varepsilon + T_D$ (**Section 4.2**). The bed wall layer model of P_{wall} is also shown for comparison.

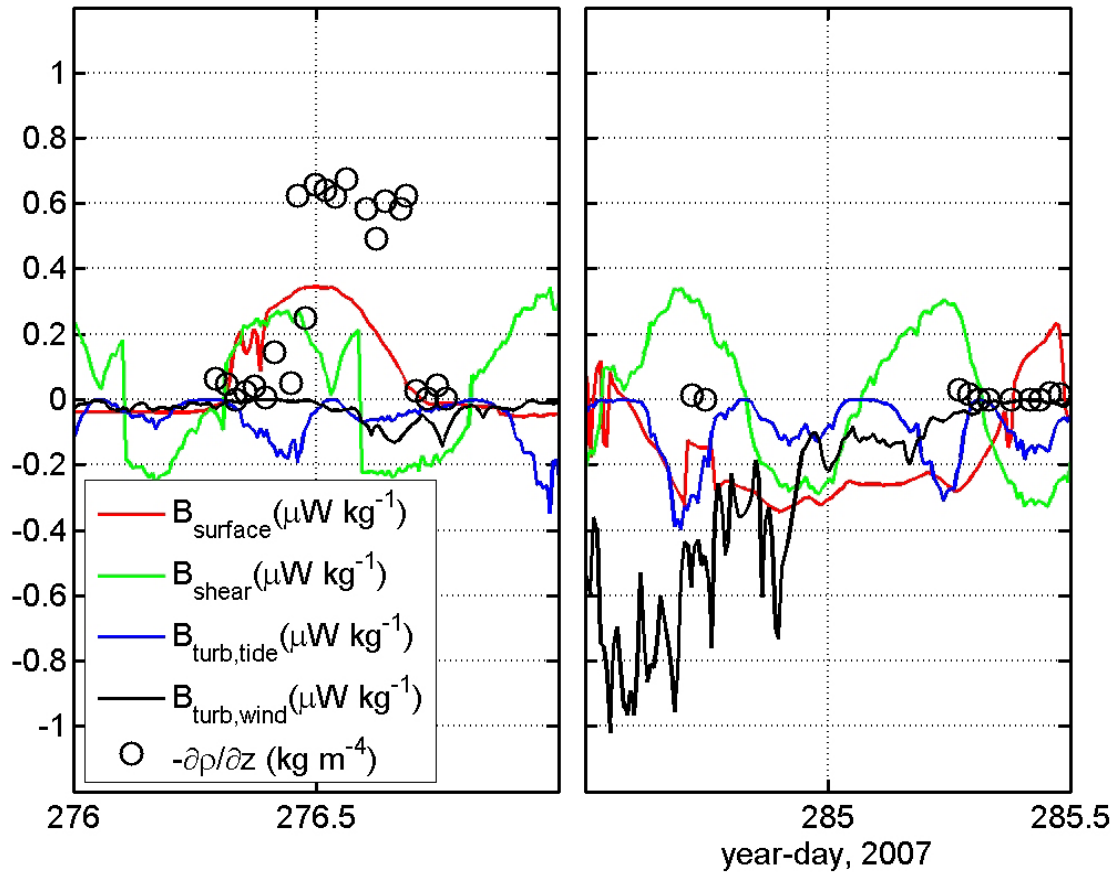


Figure 11: Two timeseries of estimated upper water column buoyancy fluxes and stratification at the shoal site, showing processes that can indirectly impact turbulence by modifying stratification. Shown are the stratification over the upper two meters ($-\partial\rho/\partial z$) measured with CTD profiles, and buoyancy fluxes due to: surface heat flux (B_{surface}), tidal straining (B_{shear}), tide-driven mixing ($B_{\text{turb,tide}}$), and wind-driven mixing ($B_{\text{turb,wind}}$). The period to the left was a sunny day with strong positive buoyancy fluxes and restratification during ebb (year-day 276.4), and the period to the right had a fall-season storm with wind-driven de-stratification, followed by strong overnight heat loss and no restratification on the morning ebb (year-day 285.2).

Chapter 5

SEA BREEZE FORCING OF ESTUARY TURBULENCE AND AIR-WATER CO₂ EXCHANGE¹

¹ to be published as: Orton, P.M., McGillis, W.R. and Zappa, C.J. Sea breeze forcing of estuary turbulence and air-water CO₂ exchange. In press, *Geophysical Research Letters*.

Abstract

The sea breeze is often a dominant meteorological feature at the coastline, but little is known about its estuarine impacts. Measurements at an anchored catamaran and meteorological stations along the Hudson River and New York Bay estuarine system are used to illustrate some basic characteristics and impacts of the feature. The sea breeze propagates inland, arriving in phase with peak solar forcing at seaward stations, but several hours later at up-estuary stations. Passage of the sea breeze front raises the water-to-air CO₂ flux by 1-2 orders of magnitude, and drives turbulence comparable to spring tide levels in the upper meter of the water column, where most primary productivity occurs in this highly turbid system. Modeling and observational studies often use remotely-measured winds to compute air-water fluxes (e.g. momentum, CO₂), and this leads to a factor of two flux error on sea breeze days during the study.

1. Introduction

The sea breeze is a ubiquitous fair-weather feature along most of the world's coastlines, present in warmer months at mid-latitudes, and year-round in tropical and subtropical regions [Gille *et al.*, 2003]. It arises on sunny days due to atmospheric pressure differences that develop as a result of the different solar absorption properties of sea and land. If no topographic boundaries exist, the sea breeze often penetrates tens of kilometers inland, and at some locations, hundreds of kilometers [Miller *et al.*, 2003].

Estuarine air-water gas exchange and biogeochemistry are gaining increased attention due to their potential role in the global carbon cycle [e.g., Dai *et al.*, 2009], as well as concerns over poorly-ventilated, low-oxygen bottom water. Air-water exchanges are often

primarily controlled by winds [Wanninkhof, 1992], so the sea breeze likely plays an important role with these processes. Moreover, recent studies have begun to demonstrate powerful influences of the sea breeze on circulation, freshwater residence time, and in some cases mixed layer depth in estuaries [Geyer, 1997; Simionato *et al.*, 2005], coastal embayments [Valle-Levinson *et al.*, 2003], and river plumes [Hunter *et al.*, 2007].

Here, we present first-of-their-kind observations of the inland propagation of the sea breeze past four sites along an estuary, and detailed measurements of associated air-water CO₂ exchange and water turbulence. We demonstrate the air-water flux errors that can arise from using remote wind data or daily averages in modeling or observational studies of systems with sea breezes. We conclude by using spectral analysis to look at seasonality and quantify the proportion of wind variance in the diurnal band, and briefly discuss systems likely to have similar sea breeze impacts.

2. Field Observations

A 1.85 m long Self-Orienting Catamaran (SOCa) with air-water exchange and turbulence measurements was anchored frequently at a 5.1 m deep site on the Hudson River estuary from 23 September through 2 November, 2007 (year-day 265.0-306.0; **Figure 1**). An acoustic Doppler velocimeter mounted on a forward boom sampled water velocity at 50 cm depth at 25 Hz, and the Inertial Dissipation Method (IDM) was used with the frozen field assumption to estimate 10 minute averages of the rate of dissipation (ϵ) of turbulent energy [Chapter 3; Zappa *et al.*, 2003]. A keel rotated SOCa so that the boom was oriented into the current to avoid wake biases. Periods with a wave orbital speed greater than 40% of mean flow speed were omitted to avoid biases from aliasing of wave energy

into the inertial subrange [Lumley and Terray, 1983]. Nearby, a bottom-mounted acoustic Doppler current profiler (ADCP) measured vertical profiles of velocity at 1 Hz and 25 cm vertical resolution, permitting computation of shear production (P) of turbulent energy [e.g., Orton and Visbeck, 2009]. Five 12-hour time series with vertical CTD profiling (salinity, temperature) were also performed from a small anchored boat.

SOCa also provided automated CO₂ profiling using a gas valve switching system, and water-to-air CO₂ flux (F_{CO_2}) estimates using the Gradient Flux Technique [GFT, Chapter 3; Zappa *et al.*, 2003]. The profiling system measured CO₂ partial pressure (pCO_2) using a non-dispersive infrared sensor (NDIR), sampling air from atmospheric heights of 0.4 and 2.25 m and from the headspace of an equilibrator receiving pumped surface water (0.2 m depth). Timeseries measurements were made of wind and air temperature with a sonic anemometer (height 1.2 m), humidity and pCO_2 with an NDIR (height 2.25 m), and water temperature (depth 0.2 m). GFT utilizes the fact that a constituent's air-water exchange is proportional to its vertical gradient in the atmospheric surface layer, and corrects for the smearing of the gradient by turbulent mixing. The required air-water heat and momentum fluxes and Monin-Obukhov Similarity Theory parameterizations of turbulent diffusivity were all computed using the Matlab COARE 3.0 bulk flux toolbox [Fairall *et al.*, 2003]

Additional measurements utilized in this paper include our own meteorological station at Piermont Pier (anemometer at 8 m height), and National Data Buoy Center (NDBC) stations at Robbins Reef lighthouse in Upper New York Bay (code ROBN, anemometer at 22 m height) and Sandy Hook (code SDHN, at 9 m height), all mapped in **Figure 1**. Our Piermont Pier station is a tripod on top of a one-story flat-top building, with measurements that include a cup/vane anemometer at 8 m height above mean water level,

solar radiation and air temperature. When inter-compared in this paper, wind data are transformed to 10 m height wind (U_{10}) by assuming neutral atmospheric conditions and a sea surface aerodynamic roughness length of 3×10^{-4} m, an approximation for $\sim 6 \text{ m s}^{-1}$ along-channel winds and ~ 30 cm wind seas [Drennan *et al.*, 2005], typical of the Hudson's sea breeze. Uncertainty of a factor of 10 in roughness leads to uncertainty in the U_{10} estimates of only $\pm 10\%$ or less, and almost no error for the sites near 10 m height.

Sea breeze days are defined using a three-stage conditional filter similar to that of Furberg *et al.* [2002], designed to identify days with a daytime onset of a surface onshore wind that is related to the cross-shore air temperature gradient. The stages require that (1) the sunrise-to-sunset mean air temperature over land must be greater than the temperature over the sea, (2) the wind must blow onshore for at least two hours between [sunrise +2h] to [sunset +2h], and (3) a majority of winds from [sunrise -8h] to [sunrise +2h] must be calm (below 2 m s^{-1}) or offshore.

3. Results and Discussion

On sunny, warm days during the field study, a land-sea temperature gradient built up by mid-morning and wind observations showed characteristics of a sea breeze, with south winds arriving at the measurement sites by mid-afternoon (**Figure 1**). Cooling or moderating temperatures often followed the arrival of the south winds. There were a total of seven sea breeze days, year-days 269, 272, 274, 275, 276, 277 and 279, for which the general pattern and estuarine impacts of winds are described below.

There was often a well-defined up-estuary delay in arrival of the south wind, to at least the furthest station northward, 71 km up-estuary (**Figures 1-2**). This suggests the

marine layer was propagating as a gravity current, as sea breezes typically do over land [Miller *et al.*, 2003] and land breezes over the ocean [Gille *et al.*, 2005]. Moreover, wind and temperature changes were often abrupt, suggesting a front formed at the leading edge, an additional feature of sea breezes and gravity currents [Miller *et al.*, 2003]. The sea breeze wind pattern was typically also present at LaGuardia Airport (LGA; **Figure 1**), so the marine layer may have traveled the over-land route northward past LaGuardia to get to Piermont, or up the steep-walled Hudson which is bordered by 100 m or greater topography and infrastructure in most places.

The observed lag of the sea breeze with distance up the Hudson is useful for estimating marine layer height by inverting the gravity wave propagation speed equation, $U_{sb} = \gamma(g'h)^{0.5}$, where h is a scale height, $g' = g(\Delta\theta/\theta)$ is the reduced gravity, $\Delta\theta$ is the inversion strength, θ is atmospheric potential temperature in Kelvin, and γ is ~ 0.62 [Gille *et al.*, 2005]. The lags in arrival of the wind front over the 55 km distance from ROBN to SOCa, were 3.34 and 3.64 h on year-days 274 and 277, suggesting propagation speeds of 4.6 and 4.2 m s⁻¹, respectively. Using these speeds with the observed afternoon mean land-sea temperature difference of 3°C (**Figure 1**, bottom panel) and 6°C gives scale heights (h) of 470 and 280 m. Prior observations of New York area sea breeze inversion heights have been from 100-300 m [Childs and Raman, 2005; Novak and Colle, 2006; Thompson *et al.*, 2007]. The higher h on year-day 274 may explain the relatively robust inland propagation on that day, making the feature less sensitive to urban roughness elements that have been shown to slow propagation [Childs and Raman, 2005].

3.1 Sea breeze driven turbulence and air-water CO₂ exchange

The diurnal wind cycle had a dominant effect on the water-to-air CO₂ flux (F_{CO_2}) on sea breeze days during the study (**Figure 2**). From Piermont northward, sea breeze days typically had light winds in the middle of the day, with glassy or light chop sea surface conditions and SOCa F_{CO_2} values below 5 mmol m⁻² d⁻¹. When the sea breeze arrived at SOCa ($U_{10} = 5.0-7.7$ m s⁻¹), wind wave breaking was often observed, and F_{CO_2} rose by a factor of 10-100 to as much as 73 mmol m⁻² d⁻¹.

The sea breeze can drive near-surface turbulence comparable to spring tide levels, but with daily recurrence (**Figure 3**). Mean dissipation rates (ϵ) at 50 cm depth associated with 5.0-7.7 m s⁻¹ winds (U_{10}) and weak currents (below 0.4 m s⁻¹) during the entire study were 8.0×10^{-6} W kg⁻¹. These are comparable to ϵ at the same depth during peak spring tides with weak winds (U_{10} below 4 m s⁻¹), which averaged 5.2×10^{-6} W kg⁻¹. Peak spring tide is defined as periods within two days of the month's strongest spring tide, with depth-average ebb tide currents from 80-100% of tidal maxima (spring ebbs had stronger near-surface turbulence than floods). The turbulent shear production rate (P) is closely related to and typically scales with ϵ [e.g., *Gross and Nowell, 1985*], and the average spring tide upper water column P is also similar to the sea breeze driven ϵ . The shoal site where SOCa was deployed is 5.1 m deep, but a 100-day current profiler deployment east of Piermont Pier in the Hudson's deep channel (14 m) where currents are stronger [*Orton and Visbeck, 2009*] exhibits similar upper water column P levels (**Figure 3**). For comparison, wall-layer modeled dissipation levels at 50 cm depth for a quadratic drag coefficient of 0.0012 and winds from 5.0-7.7 m s⁻¹ are $1.1-4.1 \times 10^{-6}$ W kg⁻¹, but additional superimposed processes (e.g. wind wave breaking) likely explain the higher observed sea breeze driven ϵ .

The diurnal phasing of the sea breeze is particularly interesting in light of diurnal cycles of solar heating, solar heating enhanced stratification, and primary production. The Hudson is turbid, 90% of light is often attenuated in the upper meter, and light limitation has been shown to be a very important control on photosynthesis [Malone, 1977]. Calm waters at mid-day enabled solar heating to warm surface waters by up to 2.2°C (Figure 2), and the vertical temperature gradient typically enhanced density stratification by 50-100%, relative to salinity stratification alone. Water pCO_2 at 20 cm depth decreased during these periods by as much as 42% (year-day 276.5-276.7; Figure 2). This was likely due to primary production, as a 2°C change in temperature would only result in a 5% change in CO_2 solubility [Wanninkhof, 1992].

3.2 Errors from under-sampling or using remote winds

Modeling and observational studies often use remote [e.g., Hellweger *et al.*, 2004; Yan *et al.*, 2008] or daily-average [e.g., Yan *et al.*, 2008] wind forcing to parameterize air-water exchanges, or measure gas exchange on daily or often longer timescales with deliberate chemical tracer injection. Using remote wind data with a quadratic parameterization can lead to large errors in estimated air-water exchanges (e.g. CO_2 , momentum). The top panel of **Figure 2** shows four days of measured F_{CO_2} at the SOCa site, compared with estimates from a quadratic wind-based parameterization using local winds [Wanninkhof, 1992], and from the parameterization using remote wind data measured at the ROBN station. Using the parameterization with local winds for all the sea breeze days gives a net F_{CO_2} estimate 5% above the *in situ* measurements, whereas using the parameterization with remote winds gives a net F_{CO_2} estimate 92% above the *in situ*

measurements and marked differences in diurnal phasing of the flux. Until 2006, there were no operational wind data measurements on the Hudson or New York Bay, and this is still common for many estuaries.

Using daily averages will obscure diurnal phasing effects important to biogeochemical processes, and can lead to overestimation of the net flux. The timing of the sea breeze can reduce the net F_{CO_2} , relative to steady winds, if it arrives at the time of day that photosynthesis has minimized the surface water pCO_2 (e.g., year-day 276.7). Moreover, new measurements from August 2009 at Piermont Pier show that pCO_2 there can vary from highly supersaturated (2000 μatm) to highly undersaturated (200 μatm) from early morning to late afternoon, along with supersaturation of oxygen. Strong diurnal cycles in pCO_2 have also been observed in other estuaries [e.g., *Dai et al.*, 2009].

3.3 Broader context

The seasonality and along-estuary variation of diurnal band winds are illustrated with wind velocity spectra in **Figure 4**. Diurnal band winds can dominate the wind variability on the Hudson for as much as a week at a time in spring, summer or early fall. Integrating the spectra, the diurnal band ($0.75 < f < 1.3 \text{ cyc d}^{-1}$) provides 20% of total wind variance at both ROBN and Piermont during sea breeze season. Viewing all the available data from these sites, the sea breeze is a more reliable mid-day and afternoon feature at Robbins Reef and Sandy Hook. At Piermont, the phase lag and duration of the sea breeze are highly erratic, and the reverse process, the land breeze, provides some of the diurnal wind energy. The erratic phase lag is likely due to the long propagation distance to that site, as many prior

studies have shown a high level of sensitivity of deep inland propagation to ambient synoptic winds [Miller *et al.*, 2003].

Sea breezes are a common and in some cases powerful forcing agent in many estuaries and coastal regions [e.g., Geyer, 1997; Hunter *et al.*, 2007; Simionato *et al.*, 2005; Valle-Levinson *et al.*, 2003], many of which likely exhibit similar impacts on air-water exchanges and turbulence to those reported here. A quick survey of a few other estuaries with good NOAA-NDBC buoy coverage shows that the Strait of Juan de Fuca is a system with stronger sea breezes (often 10 m s^{-1}) and more robust and predictable inland propagation, likely due to strong topographic trapping of the marine layer by mountains to the north and south. A common summertime wind pattern is that west winds are maximal at $\sim 1700 \text{ h}$ local time near the ocean and maximal at $\sim 2200 \text{ h}$ at the eastern end of the Strait, consistent with propagation at 8.0 m s^{-1} .

In conclusion, we have demonstrated that the sea breeze propagates inland and can reach at least 71 km up the Hudson/NY Bay estuarine system. Sea breeze winds can raise F_{CO_2} by 1-2 orders of magnitude, and raise turbulence levels in the upper meter of the water column to spring tide levels on a daily recurring basis. Using remote wind data from the nearest NDBC site in a quadratic wind-based parameterization led to overestimation of F_{CO_2} by 92% for sea breeze days during the study, due to strong spatial wind variability. These results demonstrate that physical and biogeochemical studies for certain estuaries should measure or model atmospheric forcing on spatial and temporal scales necessary to resolve propagating sea breezes.

References

- Childs, P. P., and S. Raman (2005), Observations and Numerical Simulations of Urban Heat Island and Sea Breeze Circulations over New York City, *Pure Appl. Geophys.*, *162*(10), 1955-1980.
- Dai, M., Z. Lu, W. Zhai, B. Chen, Z. Cao, K. Zhou, W.-J. Cai, and C.-T. A. Chen (2009), Diurnal variations of surface seawater pCO₂ in contrasting coastal environments, *Limnol. Oceanogr.*, *54*(3), 735-745.
- Drennan, W. M., P. K. Taylor, and M. J. Yelland (2005), Parameterizing the Sea Surface Roughness, *J. Phys. Oceanogr.*, *35*(5), 835-848.
- Fairall, C. W., E. F. Bradley, J. E. Hare, A. A. Grachev, and J. B. Edson (2003), Bulk Parameterization of Air-Sea Fluxes: Updates and Verification for the COARE Algorithm, *J. Clim.*, *16*(4), 571-591.
- Furberg, M., D. G. Steyn, and M. Baldi (2002), The climatology of sea breezes on Sardinia, *Int. J. Climatol.*, *22*(8), 917-932.
- Geyer, W. R. (1997), Influence of Wind on Dynamics and Flushing of Shallow Estuaries, *Estuar. Coast. Shelf Sci.*, *44*(6), 713-722.
- Gille, S. T., S. G. Llewellyn Smith, and S. M. Lee (2003), Measuring the sea breeze from QuikSCAT Scatterometry, *Geophys. Res. Lett.*, *30*.
- Gille, S. T., S. G. Llewellyn Smith, and N. M. Statom (2005), Global observations of the land breeze, *Geophys. Res. Lett.*, *32*.
- Gross, T., and A. Nowell (1985), Spectral scaling in a tidal boundary layer, *J. Phys. Oceanogr.*, *15*(5), 496-508.
- Hellweger, F., A. Blumberg, P. Schlosser, D. Ho, T. Caplow, U. Lall, and H. Li (2004), Transport in the Hudson estuary: A modeling study of estuarine circulation and tidal trapping, *Estuaries Coasts*, *27*(3), 527-538.
- Hunter, E., R. Chant, L. Bowers, S. Glenn, and J. Kohut (2007), Spatial and temporal variability of diurnal wind forcing in the coastal ocean, *Geophys. Res. Lett.*, *34*.

Lumley, J. L., and E. A. Terray (1983), Kinematics of turbulence converted by a random wave field, *J. Phys. Oceanogr.*, 13, 2000-2007.

Malone, T. C. (1977), Environmental regulation of phytoplankton productivity in the lower Hudson Estuary, *Estuar. Coast. Mar. Sci.*, 5(2), 157-171.

Miller, S. T. K., B. D. Keim, R. W. Talbot, and H. Mao (2003), Sea breeze: Structure, forecasting, and impacts, *Rev. Geophys.*, 41.

Novak, D. R., and B. A. Colle (2006), Observations of Multiple Sea Breeze Boundaries during an Unseasonably Warm Day in Metropolitan New York City, *Bull. Amer. Meteorol. Soc.*, 87(2), 169-174.

Orton, P. M., and M. Visbeck (2009), Variability of internally generated turbulence in an estuary, from 100 days of continuous observations, *Cont. Shelf Res.*, 29(1), 61-77.

Simionato, C. G., V. Meccia, W. Dragani, and M. Nunez (2005), Barotropic tide and baroclinic waves observations in the Rio de la Plata Estuary, *J. Geophys. Res.*, 110.

Thompson, W. T., T. Holt, and J. Pullen (2007), Investigation of a sea breeze front in an urban environment, *Q. J. Roy. Meteor. Soc.*, 133(624), 579-594.

Valle-Levinson, A., L. P. Atkinson, D. Figueroa, and L. Castro (2003), Flow induced by upwelling winds in an equatorward facing bay: Gulf of Arauco, Chile, *J. Geophys. Res.*, 108.

Wanninkhof, R. (1992), Relationship Between Wind Speed and Gas Exchange Over the Ocean, *J. Geophys. Res.*, 97.

Yan, S., L. A. Rodenburg, J. Dachs, and S. J. Eisenreich (2008), Seasonal air-water exchange fluxes of polychlorinated biphenyls in the Hudson River Estuary, *Environ. Pollut.*, 152(2), 443-451.

Zappa, C. J., P. A. Raymond, E. Terray, and W. R. McGillis (2003), Variation in surface turbulence and the gas transfer velocity over a tidal cycle in a macro-tidal estuary, *Estuaries*, 26(6), 1401-1415.

Figure Captions

Figure 1: Study area map, with wind and air temperature data for a strong sea breeze day.

(a) the Hudson River and New York Bay estuarine system, showing the Sandy Hook, Robbins' Reef (ROBN), and Piermont Pier meteorological stations, and the SOCa catamaran location. Wind velocity vectors and local air temperature data are shown on the right: (b) At SOCa, (c) Piermont, (d) ROBN, and (e) Sandy Hook, rotated by 30° clockwise to account for the different principal axis of the diurnal winds at that site. The last panel (f) shows air temperatures over the coastal Atlantic Ocean in New York Bight (NOAA buoy 44025, 40°15' N, 73°10' W) and inland at Newark (EWR). Similar wind patterns were typically also observed at LaGuardia Airport (LGA).

Figure 2: Observations during the same period shown in **Figure 1** and the subsequent three days: (a) **water-to-air** CO₂ flux estimates (F_{CO_2}) including SOCa observations, as well as those computed from a quadratic wind-based parameterization [Wanninkhof, 1992] with local winds (W92soca) or remote winds (W92robn), (b) SOCa water-side CO₂ partial pressure (pCO_2) and solar radiation, (c) water temperature (shading) and depth (black line), and (d,e) wind velocity vectors and air temperatures at SOCa and ROBN.

Figure 3: Comparison of turbulence levels resulting from sea breezes and spring tides. Average near-surface dissipation (ϵ) and shear production (P) are shown for peak spring tide currents over the shoal at SOCa ("shoal tide") and peak spring tide currents over the deep channel ("channel tide"), and compared with periods with typical peak sea breeze

wind speeds of 5.0-7.7 m s⁻¹. Sea breeze P is not shown because waves bias the P measurement, and channel tide ε was not measured.

Figure 4: Variance-preserving wind velocity spectra for two sites along the Hudson/NY Bay estuarine system. Analysis periods include sea breeze “season” from April-August, 2009; “offseason” from January-February, 2009; and “peak 2007” from year-day 272.0-279.0 during the field study.

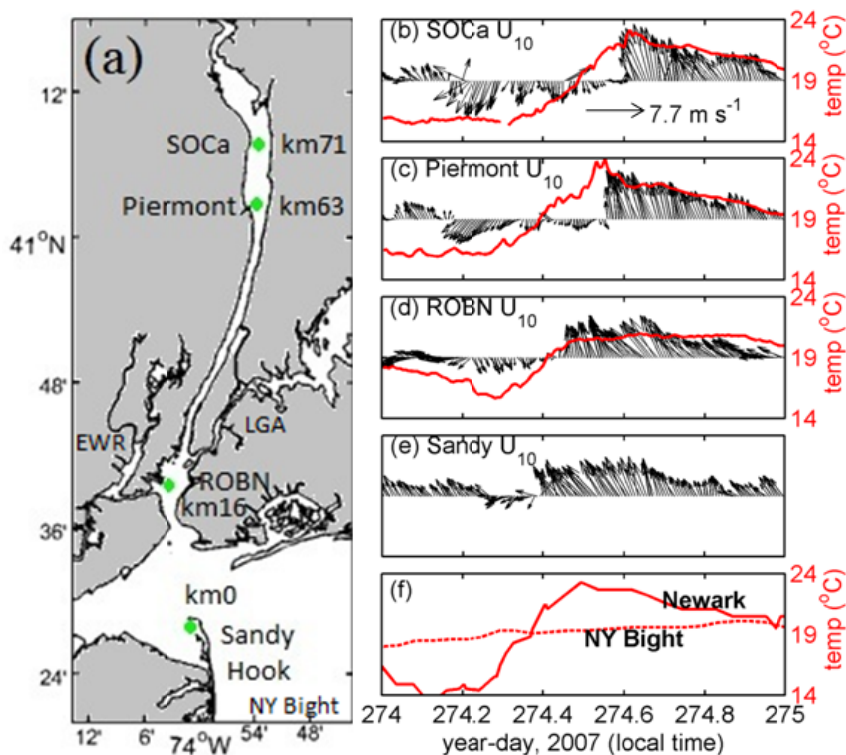


Figure 1: Study area map, with wind and air temperature data for a strong sea breeze day. (a) the Hudson River and New York Bay estuarine system, showing the Sandy Hook, Robbins' Reef (ROBN), and Piermont Pier meteorological stations, and the SOCa catamaran location. Wind velocity vectors and local air temperature data are shown on the right: (b) At SOCa, (c) Piermont, (d) ROBN, and (e) Sandy Hook, rotated by 30° clockwise to account for the different principal axis of the diurnal winds at that site. The last panel (f) shows air temperatures over the coastal Atlantic Ocean in New York Bight (NOAA buoy 44025, 40°15' N, 73°10' W) and inland at Newark (EWR). Similar wind patterns were typically also observed at LaGuardia Airport (LGA).

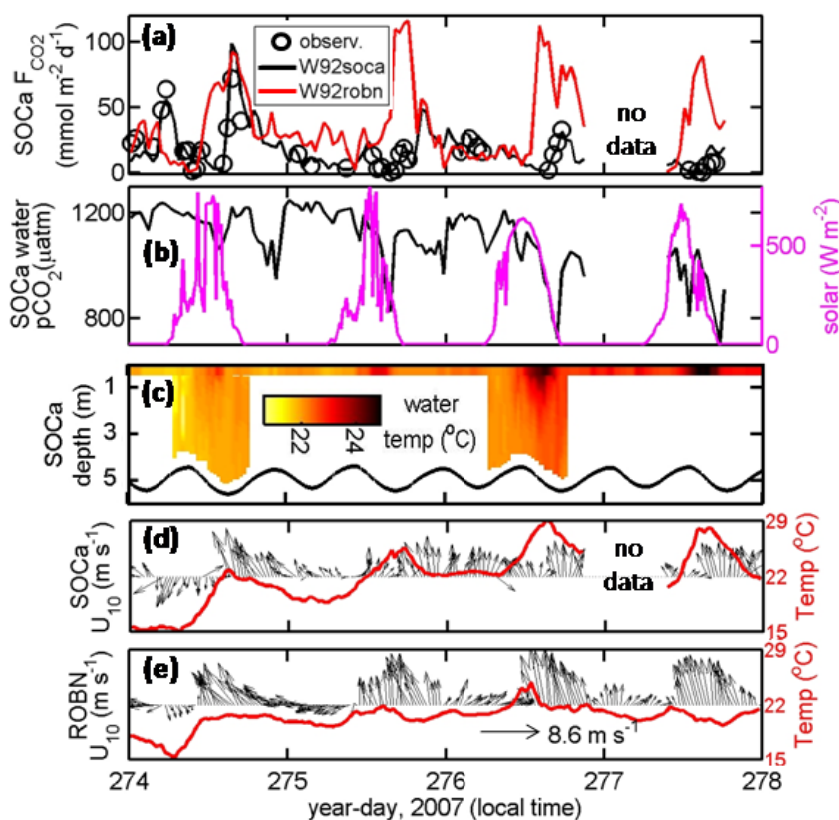


Figure 2: Observations during the same period shown in **Figure 1** and the subsequent three days: (a) water-to-air CO_2 flux estimates (F_{CO_2}) including SOCa observations, as well as those computed from a quadratic wind-based parameterization [Wanninkhof, 1992] with local winds (W92soca) or remote winds (W92robn), (b) SOCa water-side CO_2 partial pressure ($p\text{CO}_2$) and solar radiation, (c) water temperature (shading) and depth (black line), and (d,e) wind velocity vectors and air temperatures at SOCa and ROBN.

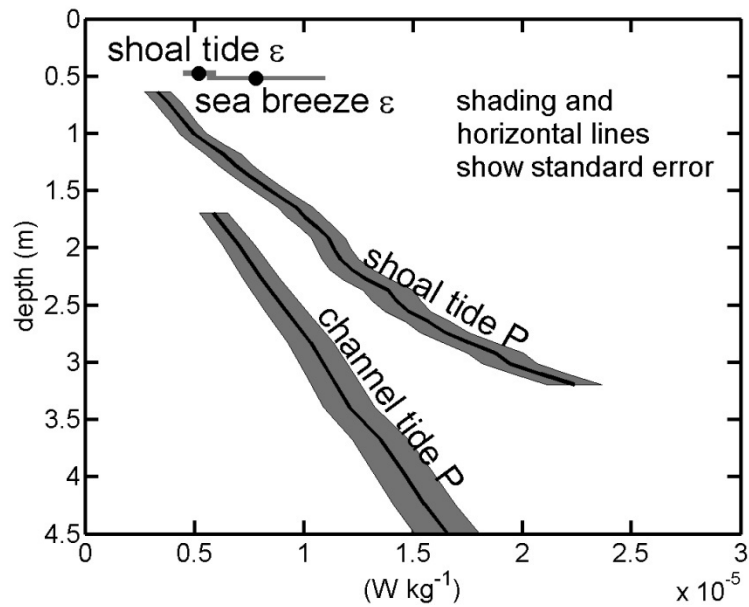


Figure 3: Comparison of turbulence levels resulting from sea breezes and spring tides. Average near-surface dissipation (ϵ) and shear production (P) are shown for peak spring tide currents over the shoal at SOCa (“shoal tide”) and peak spring tide currents over the deep channel (“channel tide”), and compared with periods with typical peak sea breeze wind speeds of $5.0\text{--}7.7\text{ m s}^{-1}$. Sea breeze P is not shown because waves bias the P measurement, and channel tide ϵ was not measured.

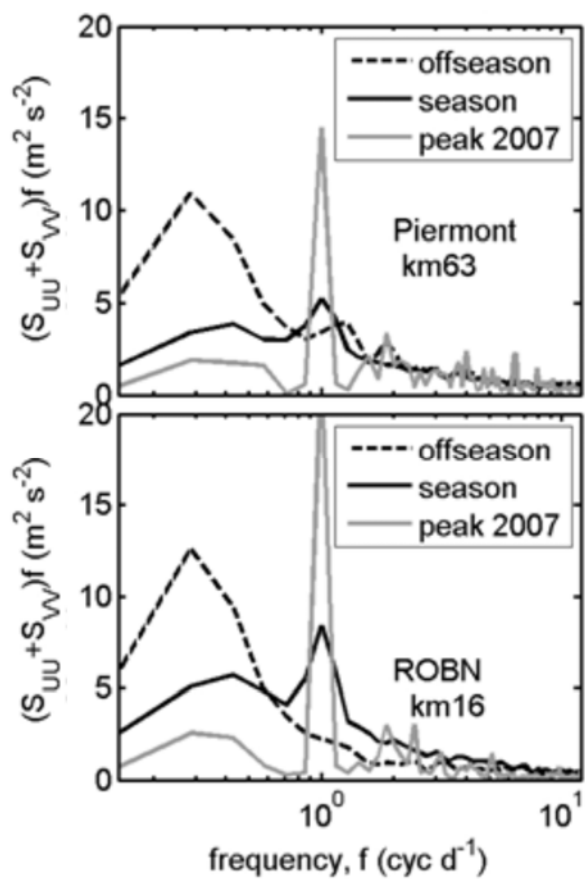


Figure 4: Variance-preserving wind velocity spectra for two sites along the Hudson/NY Bay estuarine system. Analysis periods include sea breeze “season” from April-August, 2009; “offseason” from January-February, 2009; and “peak 2007” from year-day 272.0-279.0 during the field study.

Chapter 6

CONCLUSIONS AND FUTURE RESEARCH

1. Summary

A study was undertaken to examine the tidal and atmospheric controls on near-surface turbulence and air-sea exchange of CO₂ in an estuary. Autonomous methods and platforms were developed to measure near-surface turbulence and air-water exchanges, and an estuary sampling program was executed in the Hudson River estuary with deployments over a wide range of tidal and atmospheric forcing. These observations have been interpreted in light of the general circulation and dynamics of estuaries, as well as atmospheric processes, and the utility of simple dynamical and regression models has been evaluated for simulating near-surface turbulence and air-water CO₂ exchange.

2. Primary Conclusions

The primary conclusions of this research program are as follows:

1. An instrumented, Self-Orienting Catamaran (SOCa) was successfully developed to measure air-water mass, heat and momentum exchange, as well as physical properties just above and below the air-water interface. The field-tested autonomous capabilities of SOCa include an atmospheric CO₂ profiling and air-water flux measurement system, surface-following measurements of water velocity and turbulent energy dissipation, and rotational orientation of water sensors into a variable surface current to avoid flow distortion.

2. Methods were developed for multi-month deployments and data processing for acoustic Doppler current profilers, permitting collection of billions of 0.5 or 1 Hz velocity averages and making millions of estimates of several turbulence parameters in the budget of turbulent kinetic energy. Benefits of the continuous long-term turbulence record include our capturing: (1) the seasonality of turbulence due to changing riverflow, (2) hysteresis in

stratification and turbulence over the fortnightly cycle of tidal range, and (3) intermittent events such as breaking internal waves.

3. A location with convergent, sloped channel morphology has strong turbulence generated at mid-water column by internal wave breaking and shear instability, and is maximal during stratified periods when bottom boundary layer turbulence is minimal at other sites.

4. Wind speed has the strongest correlations with turbulent energy dissipation at 50 cm depth (ϵ_{50}), yet dissipation was often an order of magnitude or more above that predicted from a wind wall layer law, even when whitecapping was not observed.

5. The net upward air-sea heat flux correlates moderately with ϵ_{50} , but it is demonstrated that this cannot energetically be caused by free convection. Examining buoyancy fluxes that impact stratification and can indirectly control turbulence, wind-driven mixing dominated during a fall-season storm event, but strong heat loss after the storm may have been related to the study's strongest turbulence the morning after. Solar heat input and tidal mixing and tidal straining (horizontal buoyancy transport) were all important on sunny, calm weather days.

6. Near-surface low-wind (below 3 m s^{-1}) TKE budgets are closed within uncertainty levels. Observed mean ebb tide ϵ_{50} and P are well above the bed-driven wall layer model, likely due to local shear instability, and flood tide ϵ_{50} and P fit closer to an open channel flow model that has low turbulence near the sea surface.

7. The sea breeze often travels inland as a gravity current, arriving in phase with solar forcing and biological p_{CO_2} drawdown near the ocean, but increasingly out of phase with propagation up-estuary. At a site 71 km up-estuary, it raises both the air-sea CO_2 exchange

and turbulent energy dissipation at 50 cm depth by 1-2 orders of magnitude. Many other estuaries likely exhibit similar sea breeze characteristics and impacts, and the Strait of Juan de Fuca is illustrated as a specific example.

3. Implications for Modeling Estuarine Gas Transfer for any Estuary

1. Ideally, we need to look at multiple sites, not one – A more complete understanding of estuarine gas transfer will require measurements at multiple sites, enabling us to examine the effects of varying wind fetch, stratification and depth.

2. Simplest models – A wind-forced model [e.g., *Wanninkhof*, 1992] is useful for first-order air-water gas flux estimates in the Hudson or similar systems. The use of wall layer turbulence models for estimating wind- and tide-driven gas transfer [e.g., *Chu and Jirka*, 2003], however, will often be inaccurate for estuaries because of the complicating effects of stratification. Also, whitecapping can be important in estuaries with a large wind fetch, such as the Hudson.

3. Ocean turbulence parameterizations [e.g., *k-omega*; *Umlauf et al.*, 2003] may be used with the *Zappa et al.* [2007] relationship between dissipation and gas transfer velocity to estimate k_{660} . This approach should be more useful than wall-layer or open channel flow turbulence models, when there is *a priori* information on waves and stratification.

4. Coastal winds are often non-synoptic – Modeling and observational studies often use remotely-measured winds to compute air-water fluxes (e.g. momentum, CO₂), and this is shown to cause large flux errors during these periods, in terms of magnitude and diurnal phase. For certain estuaries, studies will need wind estimates on space and time scales sufficient to resolve propagating sea breezes.

References

Chu, C. R., and G. H. Jirka (2003), Wind and Stream Flow Induced Reaeration, *Journal of Environmental Engineering*, 129(12), 1129-1136.

Umlauf, L., H. Burchard, and K. Hutter (2003), Extending the k-[omega] turbulence model towards oceanic applications, *Ocean modelling*, 5(3), 195-218.

Wanninkhof, R. (1992), Relationship between wind speed and gas exchange over the ocean, *J. Geophys. Res.*, 97(C5), 7373-7382.

Zappa, C., W. McGillis, P. Raymond, J. Edson, E. Hintsa, H. Zemmeling, J. Dacey, and D. Ho (2007), Environmental turbulent mixing controls on air-water gas exchange in marine and aquatic systems, *Geophys. Res. Lett.*, 34(10), 10601.

Appendix A

INTEGRATED OCEAN-ATMOSPHERE SAMPLING

ABOARD A ROBOTIC BOAT

Abstract

A battery- and solar-powered 5.5 m long robotic boat has been developed for integrated atmosphere-ocean sampling – measurements spanning the oceanic mixed layer and lower atmospheric surface layer, as well as exchanges between these layers. It has been remotely commanded to perform ocean transects as long as 63 km, to act as un-tethered buoy and hold station for a 24-hour time series, and to follow a grid to map simulated harmful algal blooms. Measurements from Massachusetts Bay are presented that include atmospheric profiles of wind velocity and temperature, atmospheric and surface ocean CO₂ partial pressures, sea-to-air CO₂ fluxes, upper ocean currents (2-49 m depth), and surface ocean fluorescence, temperature and salinity. Measurement of atmosphere and ocean properties and exchanges onboard an autonomous vehicle is a key advance for ocean observing systems and observational science programs, improving the ability of scientists to study a wide range of high-priority research topics.

1. Introduction

Several important research areas in oceanography, meteorology and climate science require integrated ocean-atmosphere measurements – sampling through the ocean mixed layer, the lower atmospheric surface layer, and exchanges between these layers. For example, predicting future climate change requires understanding what controls exchanges of carbon dioxide, heat, and momentum between the atmosphere and ocean interior, as well as the biogeochemical response. A higher resolution of air-sea exchange measurements [Bender *et al.*, 2002] and detailed studies of upper ocean biogeochemistry [Johnson *et al.*,

2009] are needed to more fully understand the Earth's carbon cycle and improve our climate prediction capabilities.

Capabilities for integrated ocean-atmosphere sampling are limited with remote sensing, autonomous underwater vehicles (AUVs) or floating platforms. Remote sensing only provides information directly on the sea surface, and AUVs have limited capabilities for air-sea interaction measurements, with almost no atmospheric capabilities and typically no interfacial measurements. In addition, AUVs are limited in their payload capacity and endurance. There has been some success in adapting buoys [e.g., air-sea interaction spar-buoy; *Graber et al.*, 2000] and shallow-water fixed platforms [e.g., Martha's Vineyard Coastal Observatory; *Edson et al.*, 2004] for air-sea interaction measurements, but researchers cannot direct these resources in mobile sampling.

Robotic boats have unique potential for integrated ocean-atmosphere sampling at high spatial and temporal resolution. They are increasingly being utilized for ocean-focused sampling [e.g., *Curcio et al.*, 2005; *Li and Weeks*, 2009; *Manley et al.*, 2000]. The Ocean-Atmosphere Sensor Integration System (OASIS; **Figure 1**) is a robotic boat that has been developed and demonstrated in several recent field deployments. Capabilities include (a) solar powered transit and sampling at sea for multi-day deployments, with remote satellite uploads for cruise plans; (b) a capability of carrying a relatively large instrumentation payload [~250 kg, versus 5 kg for a SLOCUM glider; *Webb et al.*, 2001]; (c) a water-tight, stable design for survival in storm conditions; (d) the ability to autonomously switch between acting as a boat, drifter, or untethered buoy [e.g., *Curcio et al.*, 2006]; and (e) real-time satellite and radio communications. A proposed second generation vessel, the Remote

Ocean-Atmosphere Measurement System (ROAMS; **Figure 1, inset**), would have extended autonomous sampling durations and autonomous mooring capability at sea.

Here, we describe OASIS and demonstrate the unique capabilities of robotic boats for integrated ocean-atmosphere studies. Below are summaries of platform characteristics and measurements, field studies, and performance. We highlight two coastal ocean deployments that demonstrate the vessel capabilities – (1) a cross-shelf transect off northern Virginia, and (2) a study of Massachusetts Bay, with measurements of ocean and atmosphere properties and sea-to-air CO₂ fluxes, and we conclude by discussing the future potential for robotic boats in ocean and climate observing systems.

2. Measurements

2.1 *The Ocean-Atmosphere Sensor Integration System (OASIS)*

OASIS has a weighted keel, 5.5-m length, 1.5-m width, 1400-kg weight, 0.70-m draft, 5-m mast height, and 6-m³ internal payload volume (**Figure 1**). OASIS travels at a maximum speed of 4 km h⁻¹ over water and has a water-tight design, is self-righting, and is designed to survive in storm conditions. The onboard system is capable of performing precision navigation and has been developed to support uploaded cruise tracks and station keeping as an untethered buoy. To date, three R&D prototypes have been utilized for a variety of experiments in estuaries and lakes such as mapping simulated harmful algal blooms in moving tidal currents [*Higinbotham et al.*, 2008], and have covered over 1000 km on the water.

The core onboard control system comprises seven major subsystems – propulsion, communications, command and data handling (C&DH), guidance navigation and control

(GN&C), attitude determination, power, and core meteorological sensors [Higinbotham *et al.*, 2008]. Onboard wireless communication hardware includes Freewave radios and Iridium satellite modems. The GN&C subsystem interfaces with navigation sensors including a GPS receiver and digital compass to obtain time, position, velocity, and heading measurements. The subsystem enables direct manual control or autonomous control through the use of a custom autopilot implementation. Graphical user interface software and remote communications enable the user to remotely upload transect missions, survey the camera view from the front of the vessel, and monitor data [Higinbotham *et al.*, 2008].

2.2 Instrumentation and methods

All OASIS vessels are outfitted with a basic set of mast-mounted meteorological sensors at 5 m height (e.g. pressure, temperature, humidity and wind velocity), and surface ocean salinity, temperature and fluorescence measurements using water pumped from 0.7-m depth, all of which collect data at 1 Hz and transmit it to a remote operations center [Higinbotham *et al.*, 2008]. One vessel (OASIS2) is also outfitted with a CO₂ system that samples the surface ocean and atmosphere pCO₂ at 1 Hz (described below), and a 600 kHz acoustic Doppler current profiler that records 5-s averages of water velocity measured at 50 cm intervals from 2 to 49 m depth. It also has a Campbell CSAT-3 sonic anemometer on a short mast at the front of the vessel, measuring wind velocity and temperature at 2.4 m height.

Surface ocean and atmosphere pCO₂ measurements are collected using instrumentation and an equilibrator housed inside OASIS2. A Li-Cor 840 closed-path non-

dispersive infrared (NDIR) CO₂/H₂O analyzer is used for measuring atmospheric and surface ocean pCO₂ with air samples routed through a gas valve switchbox with zero dead space. The switchbox is used so that atmospheric and air-water gradients are measured using the same NDIR analyzer, avoiding problems with instrument inter-calibration. Air for the NDIR is pumped through the switchbox in 10-minute increments from a lower atmospheric air intake at the front of the vessel, and from the headspace of an equilibrator that processes surface water pumped from 0.7-m depth below the vessel. Further details on these methods, and an evaluation of the water-side pCO₂ measurement system on a different platform are described in **Chapter 3**.

Sea-to-air CO₂ fluxes (F_{CO_2}) were estimated using observations and the standard model [e.g., *Takahashi et al.*, 2009]:

$$F_{\text{CO}_2} = -k_{660} K_0 \Delta p\text{CO}_2 (\text{Sc}_{\text{CO}_2}/660)^{-1/2} \quad (1)$$

Here, k_{660} is the gas transfer velocity at a Schmidt number (Sc) of 660 (for CO₂ in seawater at 20 °C), K_0 is the solubility, $\Delta p\text{CO}_2$ is the sea-to-air difference in pCO₂, and Sc_{CO_2} is the Schmidt number of the sample water. This uses the ideal gas approximation and assumes solubility is constant from the water intake depth upward to the sea surface [*McGillis and Wanninkhof*, 2006]. Partial pressures of CO₂ were computed from observed molar ratio concentrations and the CO₂ solubility K_0 was computed as a function of *in situ* water temperature and salinity [e.g., *McGillis and Wanninkhof*, 2006]. The transfer velocity was estimated using a parameterization that has the benefit of a realistic non-zero velocity at low wind speeds, the parameterization of McGillis et al. [2001a]:

$$k_{\text{Sc}} = (3.3 + 0.026 U_{10\text{N}}^3)(660/\text{Sc})^{1/2} \quad (2)$$

Sc was estimated using observed salinity and temperature time series [Wanninkhof, 1992]. The neutral equivalent 10-m wind speed (U_{10N}) is approximated from the measured wind at 5-m height and the observed sea-to-air differences in temperature and moisture, using the COARE 3.0 bulk algorithm [Fairall *et al.*, 2003]. Instrumentation for more “direct” air-sea heat, moisture, momentum and CO₂ flux measurements using eddy covariance [McGillis *et al.*, 2001a] or indirect profile-based methods such as the gradient flux technique [McGillis *et al.*, 2001b] have all recently been installed on OASIS and will be useful for extending and diversifying the vessel’s air-sea exchange measurement capabilities.

2.3 Coastal ocean deployments

In April 2008, while sampling without the CO₂ air-sea flux system, OASIS2 conducted an autonomous 24-hour round-trip cross-shelf transect of 63 km from Chincoteague Island, northern Virginia, and then held station in an un-tethered buoy mode for 8 hours (**Figure 2**). In June 2008, OASIS2 was deployed in Boston Harbor, MA to demonstrate the CO₂ system with measurements in Massachusetts Bay (**Figure 3**). During a 36-hour deployment from June 25-26, the vessel completed a 15-km autonomous transect (Transect T2), and conducted buoy-mode operations for 24 hours. It was towed out from a dock at the University of Massachusetts Boston (T1), through a high-traffic region out into Massachusetts Bay. A transect mission, comprising a series of waypoint latitude/longitude pairs, was remotely uploaded and it returned autonomously to the outer harbor (T2), where it began the 24 hour time series in buoy mode. The following afternoon, it was towed back into the marina (T3). Data collected during the towed periods were generally acceptable,

though atmospheric $p\text{CO}_2$ data were omitted in rare cases when winds blew vessel exhaust toward the platform.

3. Results and discussion

The field experiments demonstrate the capabilities of OASIS vessels to: (a) follow uploaded path plans utilizing radio and satellite communications, (b) perform coastal ocean transects, with the 63-km survey off northern Virginia, and (c) perform un-tethered buoy mode sampling. Weather was relatively calm with wind speeds (U_{10N}) below 6 m s^{-1} , and the average boat speed during the autonomous transects was 2.6 km h^{-1} . The boat was always able to keep within 15 m of the uploaded transect paths, and was a very stable platform for making water or wind velocity measurements; motoring during periods with 5- 6 m s^{-1} winds, the standard deviation in pitch was 0.5° and in roll was 3.6° . Vessel motoring on coastal ocean transects was limited to 1-2 days because observed solar power generation (max 600 W) did not keep up with power utilization (typically 670 W), in part due to solar panel shading (seen in **Figure 1**). Plans have been drafted to build a second-generation vessel and develop autonomous mooring capability that will address this issue (see **Section b** below).

3.1 Autonomous, integrated atmosphere-ocean sampling in Massachusetts Bay

The transect and buoy-mode observations from Massachusetts Bay are summarized with time series in **Figure 4**. The range in oceanic $p\text{CO}_2$ was 334 to 619 μatm , atmospheric $p\text{CO}_2$ varied from 365 to 405 μatm , $\Delta p\text{CO}_2$ varied from -51 to +244 μatm , and estimated CO_2 sea-to-air flux was from -3.1 to +13 $\text{mmol m}^{-2} \text{ day}^{-1}$. Ocean velocity profile data show

a $\sim 30 \text{ cm s}^{-1}$, 5-10 m deep northward current offshore of the density front, and 30 to 40 cm s^{-1} tidal currents at the entrance to Boston Harbor, alternating between flood (year-day 176.3) and ebb (177.6) tides. Atmospheric profile data show a strong temperature gradient due to a large (up to $+8 \text{ }^\circ\text{C}$) sea-to-air temperature difference and weak atmospheric mixing.

The observations are consistent with the prior observation that coastal ocean hydrographic properties, atmosphere and ocean pCO_2 , and F_{CO_2} have strong temporal and across-shelf variability [e.g., *Boehme et al.*, 1998]. Cross-shelf gradients were large, and the dominant spatial oceanic feature was a strong water density front just offshore from Boston Harbor, at the 30-m isobath and $70.83 \text{ }^\circ\text{W}$ longitude (**Figures 3-4**). The cross-front change in water pCO_2 during Transect T1 was $-310 \text{ } \mu\text{atm}$, ΔSST was $-2.1 \text{ }^\circ\text{C}$, ΔS was $+1.5$. Strong temporal variability is exemplified by the front's disappearance or advection inshore within four hours – it was not observed on the return transect T2 which extended from the offshore end of T1 to the location of the 24-hour buoy-mode station. Large temporal changes were also observed in atmospheric pCO_2 ($\sim 40 \text{ } \mu\text{atm}$), consistent with observed south winds blowing along the coastline and forcing by the diurnal solar-driven terrestrial cycle of photosynthesis.

3.2 Future possibilities with robotic boats

Approaches for extending the time that an electric robotic boat can spend at sea are autonomous docking at a buoy [e.g., *Moline and Schofield*, 2009] and autonomous anchoring [*Wood*, 2009], both of which would enable a vessel to stay on the water while re-charging with cabled electrical power or solar power. Design is underway for the ROAMS

robotic boat, with autonomous docking, and enhanced sampling capabilities and improved efficiency (**Figure 1, inset**). The 25' long ROAMS would have an improved hull and deck that accommodates more solar panels, have a more hydrodynamically efficient below-water design, and have low, uniform deck to minimize wind drag and nearly eliminate solar panel shading. ROAMS could also include a winched profiler, providing *in situ* physical and biogeochemical measurements through the ocean mixed layer.

The transect and buoy-mode capabilities utilized in both studies (**Figures 2-3**) illustrate how a “mobile buoy” coastal ocean observing system could capitalize on the flexibility of robotic boats. Two or more robotic boats can exchange roles between holding station in buoy mode, running transects, adaptive sampling of regions with maximal benefit for data assimilation, or returning to port for service. Such a system could be designed to optimally sample the observed high variability in coastal ocean hydrographic properties, atmosphere and ocean pCO₂, and F_{CO2} (e.g., **Figure 4**). Moreover, when deployed by remote control (from low ship-traffic inlets), robotic boats can save on the substantial costs of ship time for deploying regular ocean buoys [*Curcio et al.*, 2006].

Robotic boats are unique ocean sampling platforms because of their potential for integrated ocean-atmosphere sampling, continuous communications capabilities at sea, sampling versatility, and large payload capacity. They can be used for a wide range of important topics beyond air-sea CO₂ transfer, such as marine aerosols, dust or reactive nitrogen deposition, or remote-sensing ground-truth (e.g., for salinity, **Figure 2**). A technological progression is underway that will promote large-scale utilization of robotic boats, with ongoing advances in machine intelligence, solar panel technology, long-life rechargeable batteries, and satellite communications. Robotic boats have great potential for

ocean and climate studies, and can become a major component of Earth observing systems in the coming decades.

References

Bender, M., et al. (2002), A large-scale CO₂ observing plan: In situ oceans and atmosphere (LSCOP), NOAA-OAR special report, 201 pp, National Oceanographic and Atmospheric Administration, Office of Global Projects, Washington, D.C.

Boehme, S. E., C. L. Sabine, and C. E. Reimers (1998), CO₂ fluxes from a coastal transect: a time-series approach, *Mar. Chem.*, 63(1-2), 49-67.

Curcio, J., J. Leonard, and A. Patrikalakis (2005), SCOUT - a low cost autonomous surface platform for research in cooperative autonomy, paper presented at Oceans-IEEE.

Curcio, J. A., P. A. McGillivray, K. Fall, A. Maffei, K. Schwehr, B. Twiggs, C. Kitts, and P. Ballou (2006), Self-Positioning Smart Buoys, The "Un-Buoy" Solution: Logistic Considerations using Autonomous Surface Craft Technology and Improved Communications Infrastructure, paper presented at Oceans-IEEE.

Edson, J. B., C. J. Zappa, J. A. Ware, W. R. McGillis, and J. E. Hare (2004), Scalar flux profile relationships over the open ocean, *J. Geophys. Res.*, 109.

Fairall, C. W., E. F. Bradley, J. E. Hare, A. A. Grachev, and J. B. Edson (2003), Bulk Parameterization of Air-Sea Fluxes: Updates and Verification for the COARE Algorithm, *J. Clim.*, 16(4), 571-591.

Graber, H. C., E. A. Terray, M. A. Donelan, W. M. Drennan, J. C. Van Leer, and D. B. Peters (2000), ASIS: A New Air-Sea Interaction Spar Buoy: Design and Performance at Sea, *J. Atmos. Oceanic Technol.*, 17(5), 708-720.

Higinbotham, J., J. Moisan, C. Schirtzinger, M. Linkswiler, J. Yungel, and P. Orton (2008), Update on the Development and Testing of a New Long Duration Solar Powered Autonomous Surface Vehicle, paper presented at Proceedings of the IEEE/MTS OCEANS 2008 Conference.

Johnson, K., et al. (2009), Observing biogeochemical cycles at global scales with profiling floats and gliders: Prospects for a global array, *Oceanography*, 22(3), 216-225.

Li, C., and E. Weeks (2009), Measurements of a small scale eddy at a tidal inlet using an unmanned automated boat, *J. Mar. Syst.*, 75(1-2), 150-162.

Manley, J. E., A. Marsh, W. Cornforth, and C. Wiseman (2000), Evolution of the autonomous surface craft AutoCat, paper presented at Oceans-IEEE.

McGillis, W. R., J. B. Edson, J. E. Hare, and C. W. Fairall (2001a), Direct covariance air-sea CO₂ fluxes, *J. Geophys. Res.*, 106.

McGillis, W. R., J. B. Edson, J. D. Ware, J. W. H. Dacey, J. E. Hare, C. W. Fairall, and R. Wanninkhof (2001b), Carbon dioxide flux techniques performed during GasEx-98, *Mar. Chem.*, 75, 267-280.

McGillis, W. R., and R. Wanninkhof (2006), Aqueous CO₂ gradients for air-sea flux estimates, *Mar. Chem.*, 98(1), 100-108.

Moline, M. A., and O. Schofield (2009), Remote Real-Time Video-Enabled Docking for Underwater Autonomous Platforms, *J. Atmos. Oceanic Technol.*, 26(12), 2665-2672.

Takahashi, T., et al. (2009), Climatological mean and decadal change in surface ocean pCO₂, and net sea-air CO₂ flux over the global oceans, *Deep-Sea Research Part II*, 56(8-10), 554-577.

Wanninkhof, R. (1992), Relationship Between Wind Speed and Gas Exchange Over the Ocean, *J. Geophys. Res.*, 97.

Webb, D. C., P. J. Simonetti, and C. P. Jones (2001), SLOCUM: an underwater glider propelled by environmental energy, *Oceanic Engineering, IEEE Journal of*, 26(4), 447-452.

Wood, S. (2009), Application of an Autonomous Self-Mooring Vehicle: Characterization of a Lagoon Environment Using a Portable Autonomous Self-Mooring Vehicle, *Sea Technol.*, 50(1), 38-40.

Figure Captions

Figure 1: The Ocean-Atmosphere Sensor Integration System, vessel 2 (OASIS2) – a solar- and battery-powered robotic boat that is remotely monitored and controlled. (Inset) scale model (1:10) of the planned Remote Ocean-Atmosphere Measurement System (ROAMS).

Figure 2: The shoreward cross-shelf transect off northern Virginia, with salinity shaded on the OASIS2 ship track. An 8-hour time series was collected in un-tethered buoy mode at the location marked by the black circle. The total autonomous round trip was 63 km, beginning and ending at the circle.

Figure 3: Transects T1 from the Massachusetts Bay study, with the estimated sea-to-air flux of CO₂ on the OASIS2 ship track. Later, a 24-hour time series was collected in buoy mode at the location marked by the black circle.

Figure 4: Atmosphere and ocean vertical profile time series data (local time) from the entire Massachusetts Bay study, including the outgoing transect (T1), partial incoming transect (T2), 24-hour buoy mode time series, and return transect (T3). Grey or black lines are for water-side measurements (0.7 m depth), pink lines are for 2.4 m high atmospheric measurements, and red lines are for 5.0 m high atmospheric measurements. Data include water density anomaly (σ_t), temperature (T), salinity, ocean (water) and atmospheric (atmo) pCO₂, chlorophyll-a (CHL), wind speed (U_{wind}), CO₂ sea-to-air flux (F_{CO_2}), depth (z), and water velocity profiles (black areas show depths below seabed).

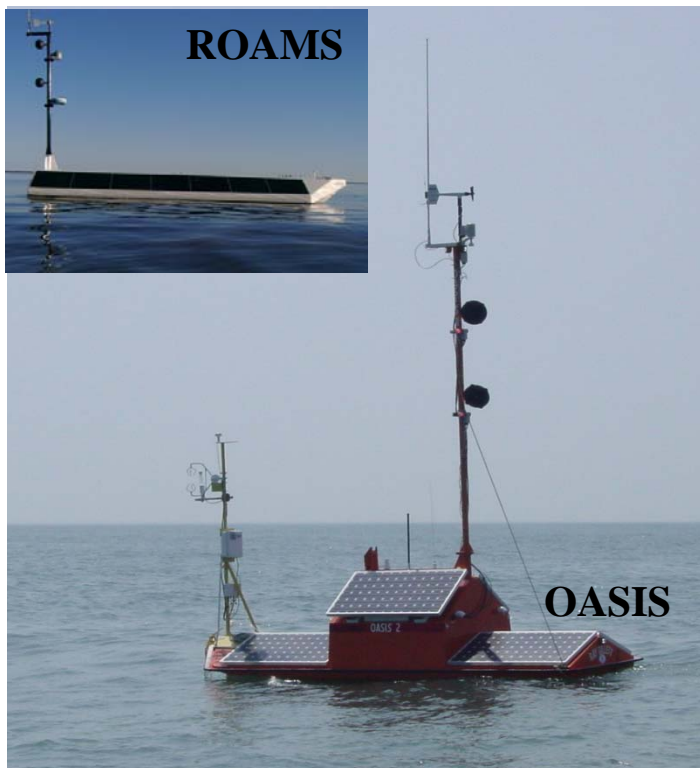


Figure 1: The Ocean-Atmosphere Sensor Integration System, vessel 2 (OASIS2) – a solar- and battery-powered robotic boat that is remotely monitored and controlled. (Inset) scale model (1:10) of the planned Remote Ocean-Atmosphere Measurement System (ROAMS).

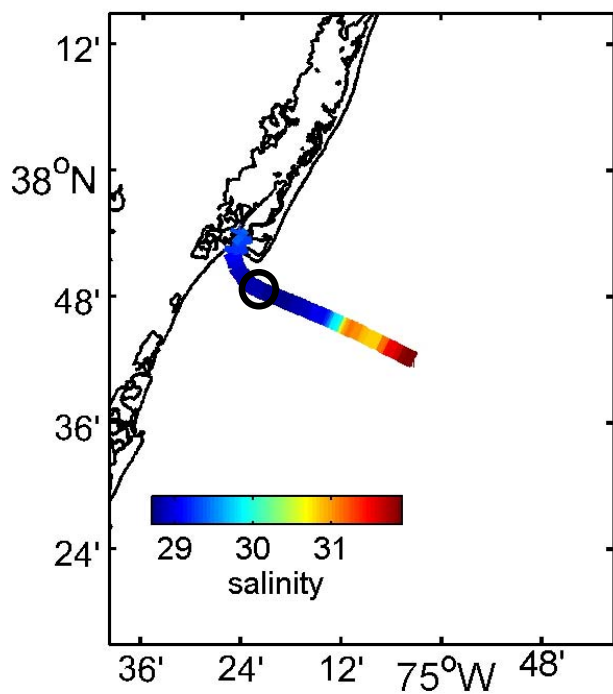


Figure 2: The shoreward cross-shelf transect off northern Virginia, with salinity shaded on the OASIS2 ship track. An 8-hour time series was collected in un-tethered buoy mode at the location marked by the black circle. The total autonomous round trip was 63 km, beginning and ending at the circle.

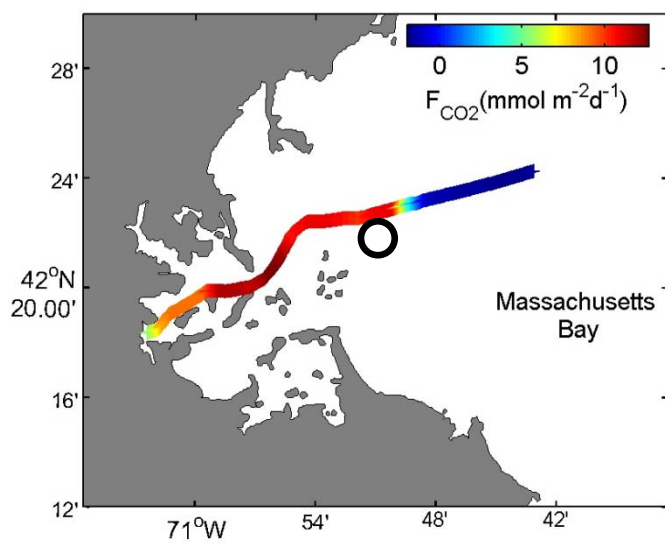


Figure 3: Transects T1 from the Massachusetts Bay study, with the estimated sea-to-air flux of CO₂ on the OASIS2 ship track. Later, a 24-hour time series was collected in buoy mode at the location marked by the black circle.

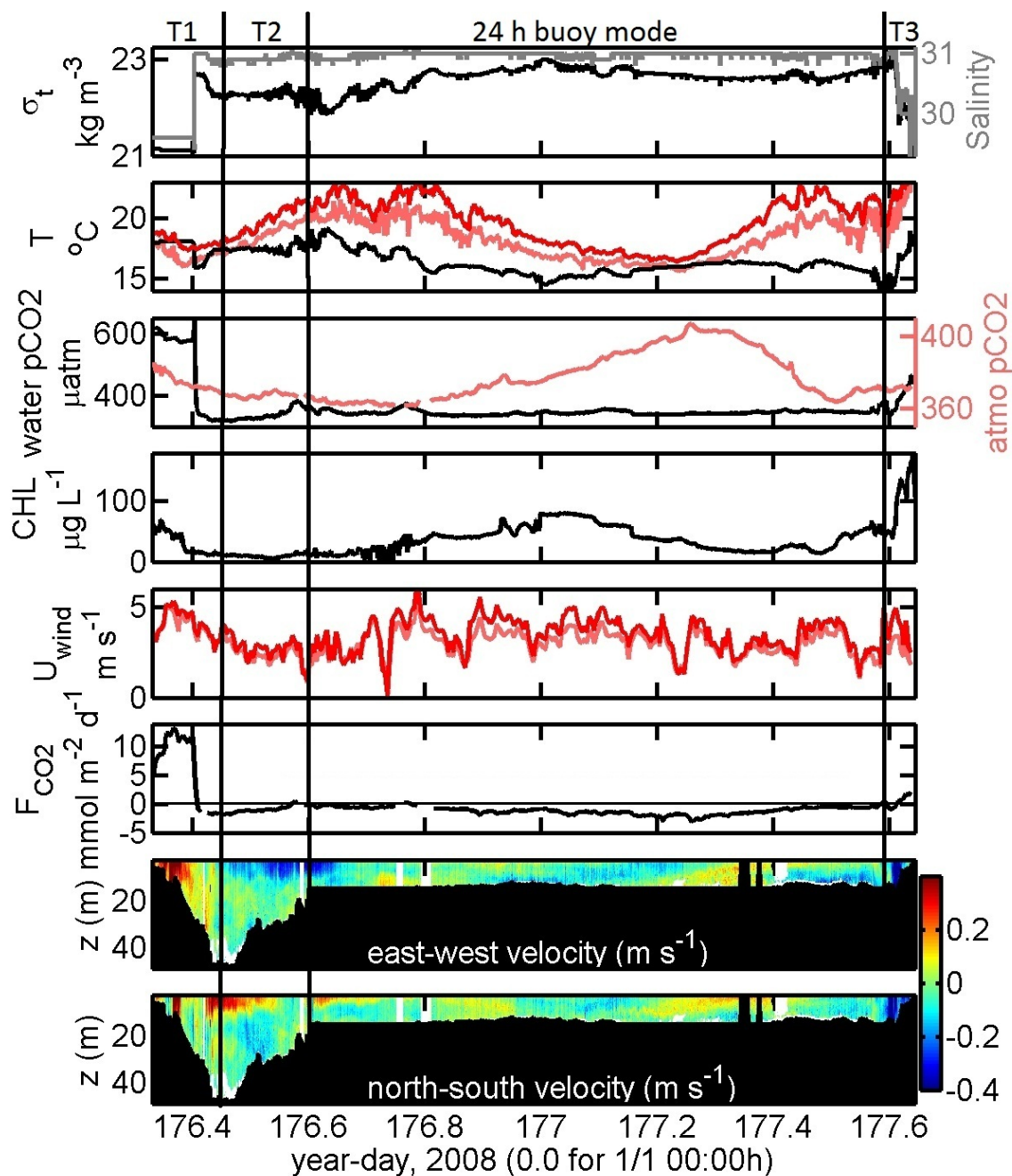


Figure 4: Atmosphere and ocean vertical profile time series data (local time) from the entire Massachusetts Bay study, including the outgoing transect (T1), partial incoming transect (T2), 24-hour buoy mode time series, and return transect (T3). Grey or black lines are for water-side measurements (0.7 m depth), pink lines are for 2.4 m high atmospheric measurements, and red lines are for 5.0 m high atmospheric measurements. Data include water density anomaly (σ_t), temperature (T), salinity, ocean (water) and atmospheric (atmo) pCO₂, chlorophyll-a (CHL), wind speed (U_{wind}), CO₂ sea-to-air flux (F_{CO_2}), depth (z), and water velocity profiles (black areas show depths below seabed).